

An Experimental Study of Surface-Mounted Bluff Bodies Immersed in  
Thick Turbulent Boundary Layers

By

Helen Afi Amorin

A Thesis Submitted to the Faculty of Graduate Studies of  
The University of Manitoba

In Partial Fulfilment of the Requirements of the Degree of

MASTER OF SCIENCE

Department of Mechanical Engineering

University of Manitoba

Winnipeg, Manitoba

Canada

## Abstract

This is a study of an experimental investigation of the effects of spanwise aspect ratio on the turbulent properties of separation bubbles over a surface-mounted bluff body. In this study, the streamwise aspect ratio was kept constant at  $l/h = 2.36$  and the spanwise aspect ratio was varied from 1 to 20. The body was immersed in a turbulent boundary layer whose thickness is equivalent to 4.8 times the body height. The Reynolds number, based on the body height and freestream velocity, was 12500. A time-resolved particle image velocimetry (TR-PIV) method was used to measure the velocity field within the separation bubble to quantify the influence of varying spanwise aspect ratio on the mean flow and turbulent characteristics. Two distinct separation bubbles developed on top and downstream of the bluff bodies. The results showed that the reattachment lengths of both separation bubbles are influenced by the aspect ratio; they increased monotonically as aspect ratio increased from  $w/h = 1$  to 8, and reach asymptotic values and do not vary significantly with aspect ratio larger than 8. The effects of aspect ratios on the mean velocities, Reynolds stresses, triple velocity correlations and turbulence production are also examined over the bluff body. Galilean decomposition, quadrant decomposition, joint probability density function (JPDF), two-point auto-correlation function and proper orthogonal decomposition (POD) are also used to investigate the impact of spanwise aspect ratio on the structures present in the flow field.

## **Acknowledgements**

I would like to express my sincere gratitude to my academic advisor Dr. Mark F. Tachie for his support, guidance and encouragement during this research. I would like to thank Dr. Xingjun Fang for his great assistance in this research.

I am very grateful for the financial support provided by the University of Manitoba.

The patience, love and encouragement of my husband, Nana Kwabena Osei, has been my pillar through this research.

Finally, I would like to thank my family and friends for their continuous love and support.

## Table of Contents

Abstract .....	ii
Acknowledgements .....	iii
Chapter 1 Introduction.....	1
1.1 Motivation for Research .....	1
1.2 Objective and Scope of Research .....	5
1.3 Thesis Structure .....	6
Chapter 2 Literature Review.....	7
2.1 Overview of Geometry-Induced Flow Separation.....	7
2.2 Coherent Structures and Eduction Techniques.....	9
2.2.1 Galilean Decomposition.....	10
2.2.2 Swirling Strength .....	11
2.2.3 Correlation Functions.....	12
2.2.4 Quadrant Analysis.....	12
2.2.5 Joint Probability Density Function .....	14
2.2.6 Proper Orthogonal Decomposition (POD).....	14

2.3 Review of Literature on Geometry-Induced Separated and Reattached Flow .....	16
2.3.1 Two-Dimensional Bluff Bodies .....	18
2.3.2 Three-Dimensional Bluff Bodies .....	26
2.4 Summary of Previous Studies on Geometry-Induced Separated and Reattached Flow .....	30
Chapter 3    Experimental Setup .....	31
3.1 Test Section and Rough Wall .....	31
3.2 Test Conditions .....	34
3.3 Time-Resolved Particle Image Velocimetry .....	34
3.3.1 Particle Illumination and Recording .....	36
3.4 Measurement Procedure .....	37
Chapter 4    Results and Discussion .....	41
4.1 Instantaneous Flow Visualization .....	41
4.2 Distributions of Mean Velocities and Reynolds Stresses .....	43
4.3 Quadrant Analysis .....	60
4.5 Turbulent Transport and Production of Kinetic Energy .....	63
4.6 Two-Point Correlation .....	68

4.7 Joint Probability Density Function (JPDF).....	73
4.8 Proper Orthogonal Decomposition (POD).....	76
Chapter 5 Conclusions and Recommendation for Future Work.....	83
5.1 Summary and Conclusion.....	83
5.2 Recommendation for Future Work.....	85
References.....	86
Appendix.....	94
A.1 Measurement Uncertainty.....	94
A.2 Error Estimation.....	94
A.2.1 The Estimation of Bias Errors.....	95
A.2.2 The Estimation of Precision Errors.....	97
A.2.3 The Estimation of Total Errors.....	98
A.3 Copyright Permission.....	99

## Table of Tables

Table 2-1 Overview of previous studies on FFS, BFS, FBFS. ....	18
Table 2-2 Overview of previous studies on cubes and other 3D bluff bodies. ....	27
Table 3-1 Upstream boundary layer. ....	40
Table 4-1 Summary of the contribution of first four modes to the total TKE. ....	78
Table A-1 Bias error of the local streamwise mean velocity ( $U$ ) at $(x, y, z) = (0.2, 1.1, 0.0)$ in the AR 1 case .....	96
Table A-2 Bias error of the local wall-normal mean velocity ( $V$ ) at $(x, y, z) = (0.2, 1.1, 0.0)$ in the AR 1 case .....	96
Table A-3 Bias error of the local streamwise mean velocity ( $U$ ) at $(x, y, z) = (3.1, 0.93, 0.0)$ in the AR 1 case .....	96
Table A-4 Bias error of the local wall-normal mean velocity ( $V$ ) at $(x, y, z) = (3.1, 0.93, 0.0)$ in the AR 1 case .....	97

## Table of figures

Figure 1-1 Geometries of a a) forward-facing step, b) backward-facing step, c) square cylinder and d) forward-backward-facing-step.....	2
Figure 1-2 Three-dimensional surface-mounted bluff body (Hussein & Martinuzzi, 1996).....	3
Figure 2-1 Schematic of separation and reattachment over a bluff body. ....	9
Figure 2-2 A sketch of the four quadrants of the $u' - v'$ plane. ....	13
Figure 3-1 Test facility.....	32
Figure 3-2 Schematic of experimental setup showing upstream roughness and block at aspect ratio 20: a) three-dimensional view, b) sectional view. ....	33
Figure 3-3 Typical setup of a time-resolved particle image velocimetry (TR-PIV) (Nematollahi, 2019). ....	35
Figure 4-1 Contour plots of the Galilean decomposition of the instantaneous flow fields for aspect ratio (a) 1, (b) 4, (c) 8 and (d) 20. ....	41
Figure 4-2 Contours of streamwise mean velocity for AR (a) 1 and (b) 20, and wall-normal mean velocity for AR (c) 1 and (d) 20.....	44
Figure 4-3 Reattachment length of separation bubble at the leading and trailing edges as function of the aspect ratio: a) separation at leading edge; b) separation at trailing edge. ....	47

Figure 4-4 Mean flow in the $x - z$ plane at half body height ( $y/h = 0.5$ ) of AR a) 1 b) 3.5 and c) 8.....	49
Figure 4-5 Growth of shear layer.....	51
Figure 4-6 Contour plots of Reynolds stresses of AR (a) 1 (left column) and (b) 20 (right column). .....	53
Figure 4-7 Contour plots of eddy kinematic viscosity of AR (a) 1 and (b) 20.....	55
Figure 4-8 One-dimensional profiles of (a) streamwise and (b) wall-normal mean velocities. ....	57
Figure 4-9 One-dimensional profile of Reynolds stresses for aspect ratio 1, 4, 8 and 20. ....	59
Figure 4-10 Quadrant analysis of AR 1 and 20. ....	62
Figure 4-11 One-dimensional profiles of triple correlations. ....	65
Figure 4-12 One dimensional profile of (a) total production in the AR 1, 4, 8 and 20 cases. (b) contribution of normal and shear stress production to the total production at AR 20 in the recirculation bubble. ....	67
Figure 4-13 Iso-contours of the two-point spatial auto-correlation function of streamwise velocity ( $R_{uu}$ ) in the (a) AR 1, (b) AR 4,(c) AR 8 and (d) AR 20 cases, with the reference point at $(x/h, y/h) = (0.04, 1), (0.3-0.6, 1)$ and $(0.8, 1.2)$ (from left to right of each row). Contour levels are from 0.3 to 0.9 in 0.1 intervals.....	69
Figure 4-14 Iso-contours of the two-point spatial auto-correlation function of wall-normal velocity ( $R_{vv}$ ) for (a) AR 1, (b) AR 4, (c) AR 8 and (d) AR 20 cases, with the reference point at $(x/h, y/h)$	

= (0.04, 1), (0.3-0.6, 1) and (0.8, 1.2) (from left to right of each row). Contour levels are from 0.3 to 0.9 with 0.1 intervals..... 71

Figure 4-15 Iso-contours of the two-point spatial cross-correlation function ( $R_{uv}$ ) for (a) AR 1, (b) AR 4, (c) AR 8 and (d) AR 20 cases, with the reference point at  $(x/h, y/h) = (0.04, 1)$ ,  $(0.3-0.6, 1)$  and  $(0.8, 1.2)$  (from left to right of each row). Contour levels are from -0.4 to -0.1 and 0.1 to 0.5 with 0.1 intervals..... 72

Figure 4-16 Contours of the joint PDF of the velocity fluctuations along the mean dividing streamline: (a)-(d) represents aspect ratios 1, 4, 8 and 20 respectively at  $x/h = 0.04, y/h = 1.04$ ; (e)-(f) represents aspect ratios 1, 4, 8 and 20 respectively at  $x/h = 0.8, y/h = 1.2$ ..... 75

Figure 4-17 Distribution of modal and cumulative energy fractions for the first 40 modes. .... 77

Figure 4-18 Iso-contours of the spatial Eigen modes in the recirculation region for the first four modes in AR 1, 4, 8 and 20..... 81

## Nomenclature

$a$	proper orthogonal decomposition temporal coefficient
$C_f$	skin friction coefficient
$C_p$	wall pressure coefficient
$d_l$	light sheet thickness
$d_s$	width of the Airy function
$d_t$	particle image diameter
$D_a$	aperture diameter
$d_p$	diameter of tracer particles
$f$	frequency
$f'$	focal length
$f^\#$	f-number of camera lens
$Fr_H$	Froude number ( $U_e/\sqrt{gH_u}$ )
$g$	acceleration due to gravity
$h$	body height
$H$	shape factor

$H_q$	hyperbolic hole size
$H_u$	upstream water depth
$I$	particle image intensity
$k_s$	equivalent sand grain roughness height
$k_s^+$	roughness Reynolds number ( $k_s U_\tau / \nu$ )
$l_r$	upstream reattachment length
$l$	body length
$L_r$	downstream reattachment length
$M$	magnification factor
$N$	number of samples
$P$	mean pressure
$P_T$	total mean pressure
$Q$	contribution to the Reynolds shear stress from a given quadrant
$R_{uu}$	temporal auto-correlations of the streamwise velocity fluctuations
$R_{vv}$	temporal auto-correlations of the wall-normal velocity fluctuations
$Re_h$	Reynolds number based on the body height ( $U_e h / \nu$ )

$Re_\theta$	Reynolds number based on momentum thickness ( $U_e\theta/\nu$ )
$S_k$	Stokes number ( $\tau_p/\tau_f$ )
$t$	time
$T$	total sampling time
$T_u$	integral time scale of the streamwise velocity fluctuations
$T_v$	integral time scale of the wall-normal velocity fluctuations
$u$	instantaneous streamwise velocity
$u'$	streamwise fluctuating velocity
$u_{rms}$	streamwise turbulent intensity
$\overline{u'u'}$	streamwise Reynolds normal stress
$\overline{u'^2v'}$	wall-normal transport of $\overline{u'u'}$
$\overline{u'v'}$	Reynolds shear stress
$\overline{u'v'^2}$	wall-normal transport of $\overline{u'v'}$
$U$	streamwise mean velocity
$U_c$	convection velocity
$U_e$	freestream velocity at the upstream location

$U_s$	slip velocity
$U_\tau$	friction velocity
$v$	instantaneous wall-normal velocity
$v'$	wall-normal fluctuating velocity
$v_{rms}$	wall-normal turbulent intensity
$\overline{v'v'}$	wall-normal Reynolds normal stress
$\overline{v'^3}$	wall-normal transport of $\overline{v'v'}$
$V$	wall-normal mean velocity
$w$	body width
$x$	streamwise coordinate
$y$	wall-normal coordinate
$z$	spanwise coordinate

### **Greek**

$\delta$	turbulent boundary layer thickness
$\delta^*$	displacement thickness

$\delta_w$	vorticity thickness
$\kappa$	von Kármán constant
$\nu$	kinematic viscosity
$\nu_t$	eddy kinematic viscosity
$\theta$	momentum thickness
$\rho$	density
$\rho_p$	density of seeding particles
$\rho_f$	density of working fluid
$\Delta U_{max}$	velocity defect
$\lambda$	wavelength of laser light source
$\lambda_z$	streak spacing
$\Pi$	Coles wake parameter
$\tau_f$	fluid characteristic time scale
$\tau_p$	particle response time

## Superscript

$()^+$  normalization by inner variables

## Acronyms

APG adverse pressure gradient

AR aspect ratio ( $w/h$ )

BFS backward-facing step

BR blockage ratio ( $h/H_u$ )

CB cube

CCD charge-coupled device

CFD computational fluid dynamics

CMOS complementary metal-oxide semiconductor

DNS direct numerical simulation

FFS forward-facing step

HWA hotwire anemometry

IA interrogation area

LDV	laser Doppler velocimetry
Nd:YAG	Neodymium: Yttrium Aluminum Garnet
Nd:YLF	Neodymium: Yttrium Lithium Fluoride
PIV	particle image velocimetry
POD	proper orthogonal decomposition
TKE	turbulent kinetic energy
TR	time-resolved
ZPG	zero pressure gradient

# Chapter 1 Introduction

## 1.1 Motivation for Research

Flow separation is a common phenomenon in diverse engineering, industrial and environmental applications. It can be caused by severe adverse pressure gradient, shockwaves and sudden changes in body geometry. Flow separation greatly affects the structural performance and integrity of these bodies: it leads to increased drag, aerodynamic loads as well as flow-induced vibration and noise. Flow separation also gives rise to high turbulence levels which leads to improved mixing and enhanced heat transfer both of which are beneficial to applications such as heat exchangers. Extensive research has thus been performed to better understand separation and reattachment mechanism to facilitate the design of engineering systems and structures.

Geometry-induced flow separation, which is the subject of this study, with focus on two-dimensional (2D) and three-dimensional (3D) surface-mounted bluff bodies, is experienced by bodies such as buildings, bridges and vehicles. A two-dimensional bluff body is one where the mean flow at the midspan of the bluff body is two-dimensional and free of side wall or end effects. Two-dimensional surface-mounted bluff bodies have been extensively studied and include a forward-facing step, backward-facing step, forward-backward-facing (intermediate streamwise aspect ratio) step and square cylinders are schematically shown in Fig. 1-1. Figure 1-1(a) shows a forward-facing step (FFS), and for this geometry, separation occurs upstream of the bluff body due to the adverse pressure gradient and reattaches to the front face of the bluff body. The separation bubble present at the front face of the bluff body is a universal feature common to separated and reattached flows. Due to the presence of the bluff body, another separation occurs

at the leading edge of the bluff body and reattaches to the top face of the step. Figure 1-1(b) shows a backward-facing step (BFS) which is characterised by a separation bubble at the trailing edge of the step. In both the forward-facing and backward-facing steps, the streamwise aspect ratio,  $l/h$  where  $l$  is streamwise length and  $h$  is body height, is sufficiently long such that there is no interaction between the recirculation bubbles developed on and downstream of the step.

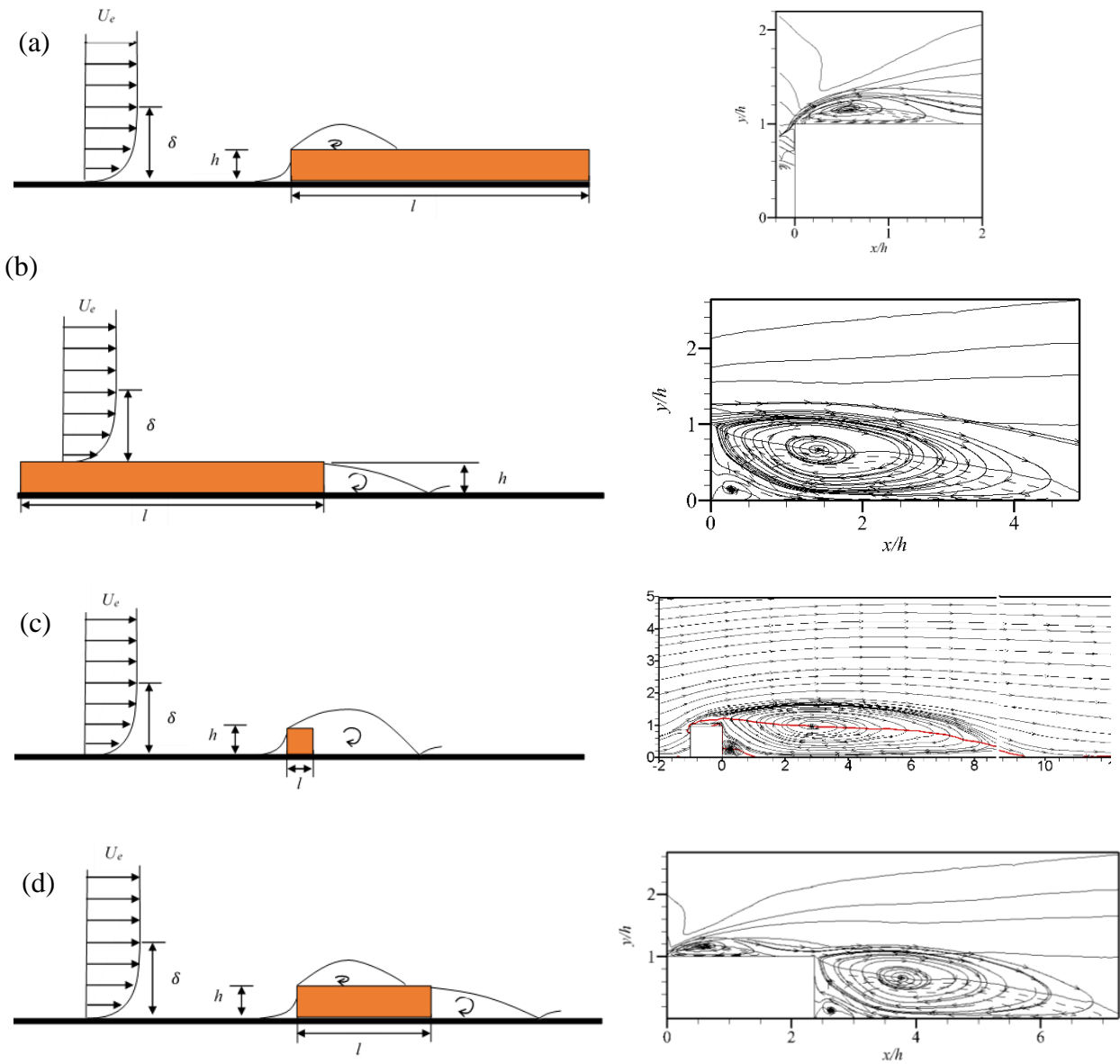


Figure 1-1 Geometries of a) forward-facing step, b) backward-facing step, c) square cylinder and d) forward-backward-facing-step.

Square prisms are characterised by one large separation bubble that extends from the leading edge of the bluff body and reattaches downstream as seen in Fig. 1-1(c). In this case,  $l/h$  is not sufficiently long to allow reattachment on top of the bluff body. When the streamwise aspect ratio ( $l/h$ ) is sufficiently long so that reattachment occurs on the bluff body but is much shorter than that of the FFS and BFS, this geometry is referred to as the forward-backward-facing step (FBFS), which is shown in Fig. 1-1(d). It is called the forward-backward-facing step because it physically resembles a combination of the FFS and BFS, where a separation bubble is formed in front, on top and downstream of the bluff body. The flow field is however much more complex than that of the FFS and BFS since there exists a strong interaction between the separation bubbles on top and downstream of the bluff body.

The surface-mounted cube and rectangular prisms are typical examples of 3D surface-mounted bluff bodies.

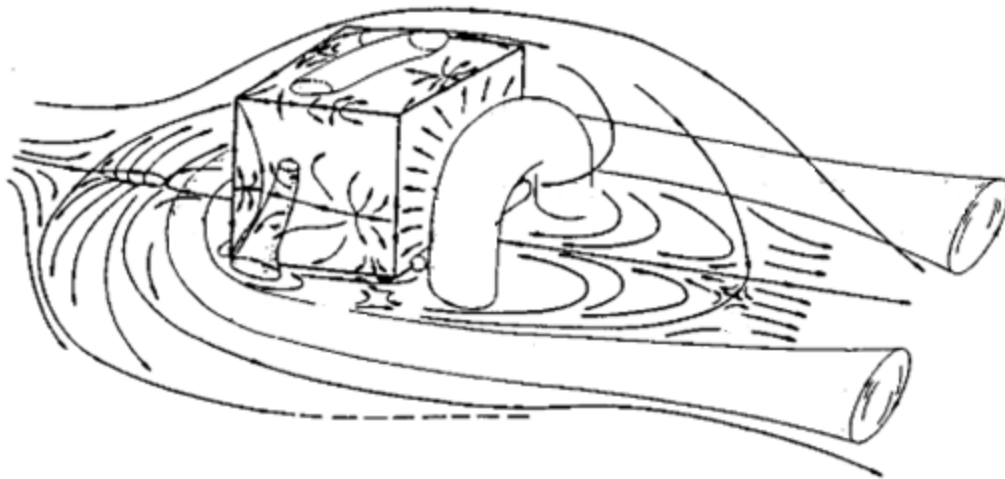


Figure 1-2 Three-dimensional surface-mounted bluff body (Hussein & Martinuzzi, 1996).

Unlike two-dimensional bluff bodies, flow separation occurs on the sides of a three-dimensional body so that end effects are not negligible, and the flow characteristics are spatially inhomogeneous in the spanwise direction, as shown in Fig. 1-2. The flow around a surface-mounted cube is characterised by a horseshoe vortex which wraps itself around the body (Castro & Robins, 1977a; Martinuzzi & Tropea, 1993). There exists a vortex core between the downstream face of the cube and the horseshoe vortex; in this region the fluid is deflected away from the centre and into the horseshoe vortex producing a region of strong mixing and turbulence production (Hussein & Martinuzzi, 1996).

While the prototypical 2D and 3D surface-mounted bluff bodies shown in Fig. 1-1 and 1-2 have been studied extensively, bluff bodies with intermediate spanwise aspect ratio have not been examined in considerable detail. Consequently, the characteristics of the separated shear layer and flow structure in the case of the intermediate aspect ratio are not well understood.

Flow characteristics are also significantly influenced by initial and boundary conditions such as relative boundary thickness,  $\delta/h$ , turbulence intensity, Reynolds number,  $Re_h$ , and wall roughness which is often characterized by the roughness Reynolds number,  $k_s^+$ . Previous research on cubes and FFS have clearly shown that these bluff bodies, when subjected to a thick oncoming turbulent boundary layer ( $\delta/h \gg 1$ ), are exposed to high turbulence intensity, high mean shear and structures, which renders the flow more complex (Castro & Robins, 1977; Castro & Dianat, 1983; Kim et al., 2003)

It is important to note that in many environmental applications such as flow past low-rise buildings, the structures are exposed to turbulent boundary layers with thickness much higher than their

heights. Nonetheless, there has been no detailed investigation of the effects of spanwise aspect ratio on surface-mounted bluff bodies subjected to a thick oncoming turbulent boundary layer.

One of the salient features of turbulence is the existence of coherent structures. Coherent structures come in many forms, and are believed to be dynamically important to turbulent production and transport (Adrian, 2007; Volino et al., 2007). Coherent structures are defined as three-dimensional regions of the flow over which at least one fundamental flow variable (velocity component, density, temperature, etc.) exhibits significant correlation with itself or with another variable over a range of space and/or time that is significantly larger than the smallest local scales of the flow (Robinson, 1991).

## **1.2 Objective and Scope of Research**

The objective of this study is to investigate the effects of spanwise aspect ratio on the mean flow, turbulent statistics and coherent structures in surface-mounted bluff bodies subjected to a thick turbulent boundary layer.

Surface-mounted bluff bodies of a fixed height ( $h = 30$  mm) and length ( $l = 70.8$  mm) but a spanwise width,  $w$ , which varied from 30 mm to 600 mm were tested in this study. This was to achieve 3D, transitional and 2D regimes. Detailed velocity measurements were performed upstream to characterise the upstream boundary layer using a time-resolved particle image velocimetry (TR-PIV). Measurements were also obtained over and downstream of the bluff body, simultaneously, using two side-by-side high speed cameras. From the TR-PIV data, the reattachment length of the separation bubbles over and downstream of the bluff body were

obtained to investigate the effects of varying aspect ratio on the mean properties of the separated shear layer. The mean velocities, Reynolds stresses, quadrant analysis, Galilean decomposition, two-point correlation, joint probability density function (JPDF) and proper orthogonal decomposition (POD) were also obtained to determine the effects of spanwise aspect ratio on turbulent properties and structures.

### **1.3 Thesis Structure**

This thesis is divided into five chapters. Review of literature on previous investigations of separated and reattached turbulent flows over both two and three-dimensional bluff bodies is presented in Chapter 2. Coherent structures and some of the methods of eduction are also discussed in Chapter 2. Chapter 3 provides a detailed description of the experimental procedure including the test facility, details of the bluff body, test conditions and the PIV system. The results are presented and discussed in Chapter 4. Finally, in Chapter 5, the results are summarized, and the major conclusions are highlighted.

## **Chapter 2 Literature Review**

A review of the pertinent literature on separated and reattached turbulent flows generated by sharp-edged surface-mounted bluff bodies is presented in this chapter. The review encompasses previous studies on flow separation induced by geometries including forward-facing step (FFS), backward-facing step (BFS), forward-backward-facing step (FBFS) and cubes. Of particular interest in this review is the dependence of the mean flow and turbulence characteristics of the separated shear layers on initial or upstream conditions such as Reynolds number, relative boundary layer thickness and wall roughness. Prior to presentation of the literature review, an overview of a generic separated and reattached flow over a surface-mounted bluff body is presented and used to introduce the flow nomenclature. An overview of coherent structures and some of the techniques used to extract such structures from the velocity field are also presented.

### **2.1 Overview of Geometry-Induced Flow Separation**

Geometry-induced flow separation, which is the subject of this study, is a common phenomenon observed in many engineering, environmental and industrial applications including low-rise buildings, bridges and vehicles. Surface-mounted bluff bodies can be classified as two-dimensional or three-dimensional bluff bodies. The dimensionality of the bluff body and mean flow induced by such a bluff body is dependent on the spanwise aspect ratio of the body. For a two-dimensional bluff body, the mean flow at the midspan of the bluff body is two-dimensional and free of side wall or end effects. Unlike two-dimensional bluff bodies, flow separation occurs

on the sides of a three-dimensional bluff body so that end effects are not negligible, and the flow characteristics are spatially inhomogeneous in the spanwise direction.

A schematic of separated and reattached turbulent flow over a generic sharp-edged surface-mounted bluff body is shown in Fig. 2-1. Also shown is the Cartesian coordinate system adopted in the present study: the  $x$ ,  $y$  and  $z$  (not shown) coordinates represent the streamwise, wall-normal and spanwise directions, respectively. The origin of the  $x$  and  $y$  coordinates is located at the base of the bluff body and the  $z$  coordinate from the centre of the span of the channel. Hereafter, the mean velocities in the streamwise, wall-normal and spanwise directions will be denoted by  $U$ ,  $V$  and  $W$ , respectively, while the corresponding fluctuating velocities will be represented by  $u'$ ,  $v'$  and  $w'$ , respectively. The geometry of the bluff body or step is characterised by its streamwise length ( $l$ ), spanwise width ( $w$ ) and height ( $h$ ). Also shown is a boundary layer upstream of the bluff body with a freestream velocity,  $U_e$ , and boundary layer thickness,  $\delta$ , which is defined as the wall-normal location at which local streamwise mean velocity is 99% of the free stream velocity. The relative boundary layer thickness is defined as  $\delta/h$ .

For the generic flow topology shown in Fig. 2-1, flow separation first occurs upstream of the bluff body, due to the presence of the adverse pressure gradient induced by bluff body and reattaches on the forward face of the bluff body. This is a common feature of both two-dimensional and three-dimensional separated and reattached turbulent flows generated by sharp-edged surface-mounted bluff bodies. At the leading edge of the bluff body, a second separation is observed and may either reattach on top of the bluff body (as shown in the Fig. 2-1) or downstream of the bluff body when the relative streamwise length of the body ( $l/h$ ) is not sufficiently long. As will be discussed in section 2.4, the relative streamwise length ( $l/h$ ) required for the flow to reattach on top of the bluff

body is strongly dependent on the spanwise aspect ratio of the bluff body ( $w/h$ ) as well as the characteristics of the upstream boundary layer including the relative boundary layer thickness ( $\delta/h$ ). At the trailing edge of the bluff body, there is another separation and a subsequent reattachment downstream of the bluff body. The reattachment length of the separation bubble on

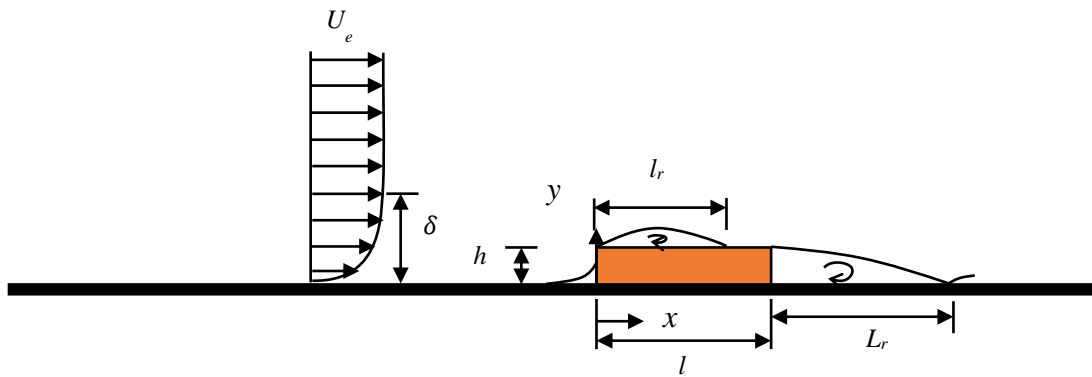


Figure 2-1 Schematic of separation and reattachment over a bluff body.

top of the bluff body is defined as the distance from the leading edge to the reattachment point and is denoted by  $l_r$ . Similarly, the reattachment length behind the bluff body, which is defined as the streamwise distance from the trailing edge to the reattachment point, is represented by  $L_r$ .

## 2.2 Coherent Structures and Eduction Techniques

Coherent structures are omnipresent in turbulent shear flows. Following Robinson (1991), coherent structures can be defined as three-dimensional regions of the flow over which at least one fundamental flow variable, such as velocity component and temperature, exhibits significant correlation with itself or with another variable over a range of space and/or time that is significantly

larger than the smallest local scales of the flow. Coherent structures are the main mechanism for turbulence production and play a dynamically important role in turbulent transport of mass, heat and momentum.

Eduction of coherent structure is defined in this study as the process of measuring the properties of a structure over its spatial extent (Hussain, 1986). A comprehensive review of coherent structures and the different techniques developed over the years for their eduction are available in Robinson (1991), Adrian et al. (2000), Alfonsi (2008), among others. In this section, those techniques applied to analyse coherent structures in this study are discussed.

### **2.2.1 Galilean Decomposition**

The Galilean decomposition is a structure detection method that is based on the principle of Galilean (Lagrangian) invariance. To detect vortices in unsteady or time dependent flows, it is necessary for the method to satisfy Galilean invariance. Kline & Robinson (1988) define a vortex as existing when the instantaneous streamlines mapped onto a plane normal to the core exhibit a roughly circular or spiral pattern, when viewed in a reference frame moving with the centre of the core vortex. To satisfy the conditions of this definition, a vortex can be identified if the velocity at the centre of each small vortex, in a turbulent field of large-scale motion consisting of small vortices within it, is removed (Adrian et al., 2000).

In Galilean decomposition, a constant advection velocity,  $U_c$ , is subtracted from the whole velocity field, revealing in this way the vortex cores traveling at this particular convective velocity.

$$u_{vc} = U - U_c \quad (2-1)$$

### 2.2.2 Swirling Strength

Swirling strength of a vortex is a measure or quantification of the strength of the swirling motion and is used to locate the vortices present in the flow. To visualize vortices, the imaginary part of the complex eigenvalue of the velocity gradient tensor is used.

The velocity gradient tensor  $D$  in Cartesian coordinates is decomposed as follows:

$$D \equiv [d_{ij}] = [v_r \ v_{cr} \ v_{ci}] \begin{bmatrix} \lambda_r & & \\ & \lambda_{cr} & \lambda_{ci} \\ & -\lambda_{ci} & \lambda_{cr} \end{bmatrix} [v_r \ v_{cr} \ v_{ci}]^{-1} \quad (2-2)$$

where  $\lambda_r$  is the real eigenvalue with a corresponding eigenvector  $v_r$ , and  $\lambda_{cr} + \lambda_{ci}i$  are the conjugate pair of the complex eigenvalues with complex eigenvectors  $v_{cr} \pm v_{ci}i$ . With the coordinate  $(x, y, z)$  system defined by the three vectors  $\{v_{ci} \ v_{cr} \ v_r\}$ , the local streamlines can then be expressed as

$$x(t) = C_r \exp \lambda_r t \quad (2-3)$$

$$y(t) = \exp \lambda_{cr} t [C_1 \cos(\lambda_{ci} t) + C_2 \sin(\lambda_{ci} t)] \quad (2-4)$$

$$z(t) = \exp \lambda_{cr} t [C_2 \cos(\lambda_{ci} t) + C_1 \sin(\lambda_{ci} t)] \quad (2-5)$$

The vortex is either stretched or compressed along the axis  $v_r$ , and swirling on the plane spanned by the vectors  $v_{cr}$  and  $v_{ci}$ .

The strength of the swirling motion is represented by  $\lambda_{ci}$ .

### 2.2.3 Correlation Functions

The temporal correlation function is the correlation between fluctuating velocity components at two different times or two points. The autocorrelation function is the correlation between velocity components at two different times and is defined as:

$$R_{ii}(\tau) = \frac{\overline{u_i(t) u_i(t+\tau)}}{u_i^2(t)} \quad (2-6)$$

Two-point correlation determines the interrelations among different fluctuating velocity components at two points. The two-point correlation is the simplest statistic containing some information on the spatial structure of a random field. For a stationary turbulence,

$$R_{ij}(x_{ref} + \Delta x, y_{ref} + \Delta y) = \frac{\overline{u_i(x_{ref}, y_{ref}) u_j(x_{ref} + \Delta x, y_{ref} + \Delta y)}}{\sigma_i(x_{ref}, y_{ref}) \sigma_j(x_{ref} + \Delta x, y_{ref} + \Delta y)} \quad (2-7)$$

where the point  $(x_{ref}, y_{ref})$  represents the reference location,  $\Delta x$  and  $\Delta y$  are the spatial separations between  $u_i$  and  $u_j$  in the streamwise and wall-normal directions, respectively, and  $\sigma_i$  and  $\sigma_j$  are the root-mean-square values of  $u_i$  and  $u_j$  at  $(x_{ref}, y_{ref})$  and  $(x_{ref} + \Delta x, y_{ref} + \Delta y)$ , respectively.

### 2.2.4 Quadrant Analysis

Quadrant analysis of the Reynolds shear stress provides detailed information on the contribution to the total turbulence production from various events occurring in the flow (Willmarth & Lu, 1972; Wallace et al., 1972). The Reynolds shear stress at each grid point is decomposed into contributions from the four quadrants excluding a hyperbolic hole of size  $H$  as follows:

$$\langle u'v' \rangle_Q(x, y, H) = \frac{1}{N} \sum_{i=1}^N u'_i(x, y) v'_i(x, y) I_Q(x, y, H) \quad (2-8)$$

where  $N$  is the total number of instantaneous velocity vectors and  $I_Q$  is an indicator function given by:

$$I_Q(x, y, H) = \begin{cases} 1, & \text{when } |u'_i(x, y)v'_i(x, y)|_Q \geq Hu_{rms}(x, y) v_{rms}(x, y) \\ 0, & \text{otherwise} \end{cases} \quad (2-9)$$

In quadrant analysis, the Reynolds shear stress is divided into four quadrants according to the signs of  $u'$  and  $v'$  as shown below:

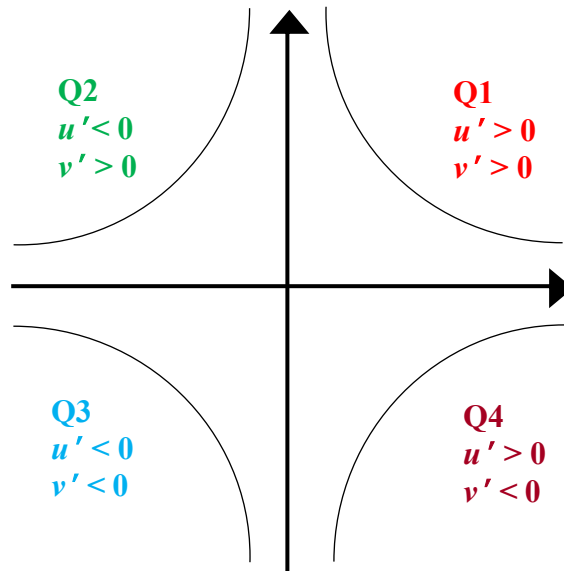


Figure 2-2 A sketch of the four quadrants of the  $u' - v'$  plane.

The four quadrant events are Q1 (outward motion of high speed fluid), Q2 (ejection of low speed fluid), Q3 (inward motion of low speed fluid) and Q4 (sweep of high speed fluids). For turbulent shear flows with positive mean shear ( $\partial U / \partial y > 0$ ), the ejection and sweep events are the dominant contributors to the Reynolds shear stress and turbulence production.

### 2.2.5 Joint Probability Density Function

The probability density function (PDF),  $P(u')$  gives a complete description of a turbulent variable,  $u'$ , at a given location and instant in time.  $P(u') du'$  represents the probability of the variable  $u'$  taking a value between  $u'$  and  $u' + du'$ , and it is defined follows

$$\int_{-\infty}^{\infty} P(u') du' = 1 \quad (2-10)$$

However, turbulence involves the dependence of several variables on one another. In this case, a joint probability density function (JPDF) between two variables JPDF,  $u'$  and  $v'$ , for instance can be defined. Here,  $P(u', v')$  is the probability of finding the first random variable between  $u'$  and  $u' + du'$ , and the second variable between  $v'$  and  $v' + dv'$ . The integral of  $P(u', v')$  over the  $u' - v'$  space is unity, i.e.

$$\int_{-\infty}^{\infty} \int_{-\infty}^{\infty} P(u', v') du' dv' = 1 \quad (2-11)$$

### 2.2.6 Proper Orthogonal Decomposition (POD)

The Proper Orthogonal Decomposition (POD) was first introduced in fluid dynamics by Lumley (1967). In POD, a series of measurements is decomposed into a number of modes which make up an orthonormal basis spanning the entire data set. POD identifies the motions which, on average, contain the most energy (Berkooz et al., 1993). In other words, POD captures the most energetic and largest structures in the first few modes. The first few modes thus reflect the dominant flow structures. In this study, the snapshot POD method proposed by Sirovich (1987) is adopted. A

detailed discussion and implementation of the snapshot method are available in Meyer et al. (2007), Sirovich (1987) and Berkooz et al. (1993) and only an overview is presented here. The first step is to calculate the mean velocity field which is considered the zeroth mode. The rest of the analysis is based on the fluctuating velocities which are arranged from the  $N$  snapshots in a matrix  $U$  as shown below:

$$U = [u^1 \ u^2 \ \dots \ u^N] = \begin{bmatrix} u_1^1 & u_1^2 & \dots & u_1^N \\ \vdots & \vdots & \vdots & \vdots \\ u_M^1 & u_M^2 & \dots & u_M^N \\ v_1^1 & v_1^2 & \dots & v_1^N \\ \vdots & \vdots & \vdots & \vdots \\ v_M^1 & v_M^2 & \dots & v_M^N \\ w_1^1 & w_1^2 & \dots & w_1^N \\ \vdots & \vdots & \vdots & \vdots \\ w_M^1 & w_M^2 & \dots & w_M^N \end{bmatrix} \quad (2-12)$$

The auto covariance matrix is created as

$$C = U^T U \quad (2-13)$$

and the corresponding eigenvalue problem

$$CA^i = \lambda^i A^i \quad (2-14)$$

is solved. The solutions are ordered according to the size of the eigenvalues

$$\lambda^1 > \lambda^2 > \dots > \lambda^N = 0 \quad (2-15)$$

The eigenvectors of equation (2-14) make up a basis for constructing the POD modes,  $\varphi^i$  as follows:

$$\varphi^i = \frac{\sum_{n=1}^N A_n^i u^n}{\|\sum_{n=1}^N A_n^i u^n\|}, i = 1 \dots N, \quad (2-16)$$

where  $A_n^i$  is the  $n^{th}$  component of the eigenvector corresponding to  $\lambda^i$  from equation (2-14) and the discrete 2-norm is defined as

$$y = y_1^2 + y_2^2 + \dots + y_M^2 \quad (2-17)$$

Each snapshot can be expanded in a series of the POD modes with expansion coefficients  $a^i$  for each POD mode  $i$ . The coefficients, also called POD coefficients, are determined by projecting the fluctuating part of the velocity field onto the POD modes as shown below

$$a^n = \Psi^T u^n \quad (2-18)$$

where  $\Psi = [\varphi^1 \varphi^2 \dots \varphi^N]$  has been introduced. The expansion of the fluctuating part of a snapshot  $n$  is

$$u^n = \sum_{n=1}^N a_n^i \varphi^i = \Psi a^n \quad (2-19)$$

### 2.3 Review of Literature on Geometry-Induced Separated and Reattached Flow

The characteristics of separated flows induced by surface-mounted bluff bodies are strongly dependent on the specific geometry of the bluff body. For a bluff body of height,  $h$ , the geometry is completely characterized by its spanwise aspect ratio ( $w/h$ ) and streamwise aspect ratio ( $l/h$ ). As discussed earlier, the dimensionality of the flow is dependent on the spanwise aspect ratio. More specifically, the flow is categorised as two-dimensional if the spanwise aspect ratio is sufficiently large so that the statistical properties are homogeneous in the spanwise direction. In

the case of three-dimensional flows, the bluff bodies are of limited spanwise extent and in such a case, end effects are of importance and the statistical properties are spatially inhomogeneous in the spanwise direction. The streamwise aspect ratio, in addition to upstream conditions is determinative of whether reattachment occurs over or downstream of the step. Consequently, the streamwise aspect ratio dictates the classification of the step as a forward-facing step (FFS), backward-facing step (BFS) or a forward-backward-facing step (FBFS).

Irrespective of the dimensionality of the separated and reattached flows generated by surface-mounted bluff bodies, both the mean and turbulent characteristics are strongly dependent on a wide range of initial and upstream conditions including relative boundary thickness,  $\delta/h$ , where  $\delta$  is the boundary layer thickness and  $h$  is the body height; turbulence intensity; Reynolds number,  $Re = U_e h/\nu$ , where  $U_e$  is the freestream velocity and  $\nu$  is the kinematic viscosity; and wall roughness, which is often characterized by the roughness Reynolds number,  $k_s^+ = k_s U_\tau/\nu$ , where  $k_s$  is the equivalent sand grain roughness height and  $U_\tau$  is the friction velocity. Given their diverse engineering and environmental applications, and also theoretical importance advancing fundamental understanding of complex turbulent flows and for validating numerical models, separated and reattached turbulent flows have been the focus of numerous investigations. In the following, the investigations of two-dimensional and three-dimensional bluff bodies that are of special relevance to the present study are reviewed.

### 2.3.1 Two-Dimensional Bluff Bodies

The most commonly investigated two-dimensional bluff bodies in previous studies are the forward-facing step (FFS), backward-facing step (BFS) and forward-backward-facing step (FBFS). Table 2-1 provides a summary of previous studies of FFS, BFS and FBFS. The information provided in the table includes the streamwise and spanwise aspect ratios as well as key parameters such as Reynolds number ( $Re_h$ ) and relative boundary layer thickness ( $\delta/h$ ).

Table 2-1 Overview of previous studies on FFS, BFS, FBFS.

Authors	$l/h$	$w/h$	$Re_h \times 10^3$	$\delta/h$	Quantities measured
Nematollahi & Tachie (2018)	160	40	7.8	4.3 – 6.7	$L_r, U, V, \overline{u'u'}, \overline{u'v'}, \overline{v'v'}, \delta_w, P, T_u, T_v$
Sherry, Jacono, Sheridan, Mathis, & Marusic (2009)	11 – 33	11 – 33	3.7 – 140	0.8 – 2.5	$L_r, u', \overline{u'u'}, \overline{u'v'}, \overline{v'v'}$
Essel, Nematollahi, Thacher, & Tachie (2015)	138	21	2 – 8	2.4 – 3.8	$L_r, U, \overline{u'u'}, \overline{u'v'}, R_{uu}, R_{vv}, Lx_{uu}, Lx_{vv}, Ly_{uu}, Ly_{vv}, P_T$
Largeau & Moriniere (2006)	–	15 – 25	76.9 – 128	0.16 – 0.26	$L_r, \overline{u'u'}, \overline{v'v'}, \overline{u'v'}, C_p$
Graziani, Lippert, Uystepuyst, & Keirsbulck (2017)	4.85 – 6.02	9.7 – 12	110 – 412	0.34 – 0.49	$L_r, U, V, C_p$
Awasthi, Devenport, Glegg, & Forest (2014)	–	31 – 500	6.64 – 213	1.62 – 26.02	$U, C_p$
Jovic (1996)	54	–	6.8 – 32	0.8 – 2	$C_f, C_p, U, \overline{u'u'}, \overline{v'v'}, \overline{u'v'}, \delta_w, S_u$

Essel & Tachie (2015)	133	21	7	2.2	$L_r, U, V, \overline{u'u'}, \overline{u'v'}, \overline{v'v'}, \delta_w$
Ampadu-Mintah & Tachie (2015)	133	21	3.2	6.8	$U, \overline{u'u'}, \overline{u'v'}, \overline{v'v'}, D_k, R_{uu}, R_{vv}, Lx_{uu}, Lx_{vv}, Ly_{uu}, Ly_{vv}$
Piirto, Saarenrinne, Eloranta, & Karvinen (2003)	–	–	15	0.6	$L_r, \overline{u'u'}, \overline{u'v'}, \overline{v'v'}$ ,
Isomoto & Honami (1989)	–	18	32	0.5	–
van der Kindere & Ganapathisubramani (2018)	0.1 – 8	$\geq 30$	20	1.3	$C_p, L_r, PDF, P_T, u', POD$
Bergeles & Athanassiadis (1983)	1 – 10	12	–	0.48	$L_r$
Chalmers, Nyantekyi-Kwakye, Fang, & Tachie (2019)	1 – 10	20	13.2	6.5	$L_r, U, V, \overline{u'u'}, \overline{u'v'}, v_T$
Fang & Tachie (2019)	2.4	20	12	4.8	$L_r, U, u', v', \overline{u'u'}, \overline{u'v'}, \overline{v'v'}, P_T$

It should be noted that some of these key parameters are not reported in many of the previous investigations. Also shown in the table are the flow quantities reported in these studies. Here,  $U$  and  $V$  are, respectively, the mean velocities in the streamwise and wall-normal directions;  $u'$  and  $v'$  are the fluctuating components in the streamwise and wall-normal directions, respectively;  $\overline{u'u'}$ ,  $\overline{v'v'}$ ,  $\overline{u'v'}$  are the streamwise Reynolds normal stress, wall-normal Reynolds normal stress and

Reynolds shear stress respectively;  $L_r$  is the reattachment length;  $C_f$  is the skin friction coefficient;  $C_p$  is the wall pressure coefficient; PDF is the probability density function;  $c_f'$  is the root-mean-square of the fluctuating shear stress;  $\delta_w$  is the vorticity thickness;  $P_T$  is the total production term;  $T_u$  and  $T_v$  are the integral time scales;  $D_k$  is the diffusion term;  $R_{uu}$  and  $R_{vv}$  are the streamwise and wall-normal correlation coefficients;  $Lx_{uu}$  and  $Ly_{uu}$  are the streamwise and wall-normal extent of  $R_{uu}$ ;  $Lx_{yy}$  and  $Ly_{yy}$  are the streamwise and wall-normal extent of  $R_{vv}$ ;  $\nu_t$  is the eddy kinematic viscosity.

### ***Forward-Facing Step (FFS)***

Sherry et. al (2010) experimentally investigated the separation bubble over a FFS at three relative turbulent boundary layer (TBL) thicknesses, over a wide Reynolds number range, i.e.  $1400 < Re_h < 19000$ . The velocity measurements were performed using particle image velocimetry (PIV). They observed that an increase in the Reynolds number led to an increase in the reattachment until  $Re_h = 8500$ , where the reattachment length remained constant with any further increase in Reynolds number.

Essel et al. (2015) investigated the effects of both roughness and Reynolds number ( $Re_h$ ) on the characteristics of separated and reattached flows induced by an FFS in a fully developed channel flow. This study was performed at a blockage ratio  $h/H = 0.2$  and a Reynolds number range of 2040 to 9130. A planar PIV was used to record the information on the reattachment length and single point statistics. For the smooth wall, it was reported that  $l_r/h$  increased from 1.4 to 2.2 up to  $Re_h = 6380$  and remained unchanged with a further increase in Reynolds number. This trend is

qualitatively similar to that observed by Sherry et al. (2010). Contrarily, for the rough wall, the reattachment length decreased from 1.4 to 1.2 and then remained unchanged at  $Re_h > 4000$ . Though qualitatively similar, the threshold value for the Reynolds number differed in both studies. Essel et al. (2015) attributed this to the different turbulence level and blockage ratio reported in both studies.

Awasthi et al. (2014) investigated the turbulent flow over an FFS in a wind tunnel over a wide Reynolds number range. They used a Pitot tube and a hot wire anemometry to perform velocity and pressure measurements. The Reynolds number ( $Re_h$ ) was varied from 6640 to 213000 for three values of the relative turbulent boundary layer (TBL) thickness, i.e.  $\delta/h \approx 2, 7$  and 26. Similar to that of Sherry et. al (2010) and Essel et al. (2015), their results showed an increase of the reattachment length with increasing Reynold number. The relation between the Reynolds number and reattachment length was found to be affected by the relative boundary layer thickness where a lower  $\delta/h$  value led to a sharper increase in  $Re_h$ .

The effects of Reynolds number and relative boundary layer thickness on the reattachment length and the pressure statistics over a FFS was experimentally studied by Graziani et al. (2017). The experiments were carried out in a closed-loop wind tunnel and three bluff bodies of different heights were used. The Reynolds number ranged from 110670 to 412000 and a relative TBL thickness of  $0.34 > \delta/h < 0.49$ . A PIV was used to investigate the flow field topology while pressure sensors were used to measure the wall pressure. An increase in the Reynolds number leads to an increase in reattachment length till an asymptotic value was reached. On the other hand, there was a decrease in the reattachment length with an increase in  $\delta/h$ .

Largeau & Moriniere (2006) investigated the effects of varying the step height on the reattachment length and turbulent quantities using a hot wire anemometry (HWA) and PIV. Varying step height resulted in three test cases of different Reynolds number, relative boundary layer thickness and aspect ratio. Two-dimensionality of the flow was ensured, and the step height was always greater than the boundary layer (i.e.,  $\delta/h < 1$ ). Reattachment length was shown to be inversely proportional to the relative boundary layer thickness ( $\delta/h$ ) as observed in Awasthi et al. (2014) and Graziani et al. (2017).

The effects of turbulent intensity on the recirculation region over a 2D bluff body have been examined in previous investigations. Hillier & Cherry (1981) investigated the effects of turbulent intensity in flow over a blunt flat plate. The turbulent intensity was varied from 1.0% to 6.5% which led to a significant reduction in the reattachment length, i.e.  $\sim 40\%$ . Similar results were observed by Kiya & Sasaki (1983) and Nakamura & Ozono (1987).

Nematollahi & Tachie (2018) investigated the effects of upstream roughness on an FFS. This study was performed in an open water channel with three different upstream walls: hydraulically smooth, transitionally rough 16-grit sandpaper and fully rough staggered cubes. A TR-PIV was used to measure the time-averaged mean velocities, Reynolds stresses, temporal auto-correlations and frequency spectra of the flow field. An increase in upstream roughness decreased the reattachment length of the recirculation bubble over the step. They also observed that the Reynolds stresses were unaffected by the sandpaper roughness but the cubes increased the streamwise Reynolds stress both near the wall and outside the shear layer, while decreasing the wall-normal Reynolds stress and Reynolds shear stress near the wall but enhancing them in the outer layer.

Essel et al. (2015) also observed that upstream roughness decreased the reattachment length by about 44% and attributed this reduction to higher momentum deficit and larger turbulence levels produced by upstream wall roughness.

### ***Backward-Facing Step (BFS)***

Essel & Tachie (2015) investigated the effect of downstream wall roughness on the reattachment length on a BFS. The Reynolds number and upstream boundary layer thickness were kept constant at 7050 and  $2.2h$ , respectively. Detailed particle image velocimetry (PIV) measurements were performed over a reference smooth wall and two rough walls produced from sandpaper 36 and 24 grits. The reattachment length was increased by wall roughness by 5% and 7% in the sandpaper 36 and 24 grits, respectively, as compared to the smooth wall. Beyond 5 step heights from the reattachment point, wall roughness reduced the streamwise mean velocity in the region adjacent to the rough walls. Wall roughness significantly increased the levels of the Reynolds stresses in the recirculation and redevelopment regions, however, the spatial coherence of turbulence structures embodied in the streamwise and wall-normal auto-correlation function is significantly reduced over the rough walls.

Ampadu-Mintah & Tachie (2015) studied the effects of surface roughness on separated and reattached region of a BFS. Two different wall conditions were examined: a smooth (acrylic) surface and rough surface generated from sand grains of average diameter 1.5 mm glued onto an acrylic plate, both placed immediately downstream of the step. One- and two-point statistics were collected using a PIV to analyse the effects of roughness on the recirculation and recovery regions of both test cases. The reattachment length, mean and turbulent statistics showed no dependence

on surface roughness in the recirculation region. However, in the recovery region, i.e. beyond 21 step heights from the trailing edge of the step, surface roughness reduced the mean velocity but increased the Reynolds stresses.

The effects of turbulent intensity on a BFS was experimentally investigated by Isomoto & Honami (1989). The experiments were carried out in an air flow tunnel and hot wire anemometry was used to obtain measurements of the mean velocity and turbulence intensity at the separation point and in the separated shear layer. The local turbulence was enhanced using a rod or cavity. The turbulent intensity was shown to be inversely proportional to the reattachment length where an increase of the turbulent intensity led to a decline in reattachment length.

### ***Forward-Backward-Facing Step (FBFS)***

Bergeles & Athanassiadis (1983) experimentally investigated the recirculation bubble length over a two-dimensional FBFS using a hot wire. With a thin upstream turbulent boundary layer ( $\delta/h = 0.48$ ) and low turbulent intensity of 0.5%, they observed that for  $l/h < 4$ , the shear layer separating from the leading edge reattaches downstream of the step and the length of the recirculation bubble measured from the trailing edge of the step decreased linearly with the streamwise length. However, for  $l/h \geq 5$ , the flow separates at the leading edge and reattaches on top of the step and separates again at the trailing edge where it reattaches downstream of the step. In this case, the reattachment length was found to be constant with any further increase in the streamwise length.

van der Kindere & Ganapathisubramani (2018) experimentally investigated the flow over a FBFS using PIV. The steps were submerged in a turbulent boundary layer of thickness of 1.37 body heights at a fixed Reynolds number of 20000, and the streamwise aspect ratio of the step ( $l/h$ ) was varied from 0.1 to 8. They observed one large separation bubble for  $l/h \leq 4$  which possessed high turbulence levels. For these steps (i.e.,  $l/h \leq 4$ ), the reattachment length decreased linearly from  $13.3h$  to  $4.4h$  as  $l/h$  was increased from 0.1 to 4. Intermittent reattachment occurred at  $l/h > 5$ , where the separation bubble reattaches on top of the step and is followed by another separation at the trailing edge of the step. For the longer steps, the reattachment length of the recirculation region on the top surface of the step remained steady at  $2.7h$ , and that at the trailing edge became asymptotic at  $3.8h$ .

Chalmers et al. (2019) performed an experimental study detailing the effects of streamwise aspect ratio on the turbulent statistics over a FBFS. The body height was kept constant at  $h = 30$  mm but  $l/h$  was varied from 1 to 10. The steps were submerged in a thick turbulent boundary layer ( $\delta/h = 6.5$ ) and a TR-PIV was used to measure the velocity field. At  $l/h = 2$ , there was intermittent separation observed where the separation bubble from the leading edge of the bluff body reattached on top of the step at  $l_r/h = 1.6$  and remained unchanged with any further increase in the streamwise length. However, the reattachment length of the recirculation bubble behind the bluff body was found to decrease as the streamwise length was increased up to  $l/h = 3$  and remained unchanged with any further increase.

It is clear from the studies reviewed above that the streamwise length aspect ratio necessary for two separation bubbles to form from the leading and trailing edges depends on the boundary layer thickness ( $\delta/h$ ). From these studies, it is observed that as the relative boundary thickness ( $\delta/h$ )

increases, the streamwise aspect ratio beyond which the separated shear layer from the leading edge attaches on top of the step decreases. Also, the asymptotic reattachment length of the separation bubble on top of the bluff body decreases with increasing  $\delta/h$ . On the contrary, reattachment length behind the bluff body increases with  $\delta/h$ .

Fang & Tachie (2019) investigated the flow over a 2D bluff body with an intermediate streamwise aspect ratio ( $l/h = 2.36$ ) immersed in a thick oncoming TBL using a TR-PIV system. Three distinct separation bubbles were observed. They found that although reattachment of the mean flow occurs on top of the step, the separating shear layer emanating from the leading edge reattached intermittently on the wall behind the step. The separation bubble over the step exhibited a low-frequency flapping motion which was linked to the large-scale motion embedded in the oncoming turbulent boundary layer, and a higher frequency breakup event attributed to the inherent instability of the separation bubble itself. A strong mutual interaction was evident between the separation bubbles on top of and behind the step, an enlargement of the former is accompanied by an enlargement of the latter. The separation bubble behind the step also exhibited flapping motion with the same frequency as the bubble on top of the step.

### **2.3.2 Three-Dimensional Bluff Bodies**

The overview of previous studies on cubes and other 3D bluff bodies is shown in Table 2-2. Castro & Dianat (1983) performed an experiment to understand how body geometry and/or upstream flow characteristics promote or prevent reattachment on the top face of the bluff body. This experiment was performed at a fixed height,  $h = 60$  mm and relative boundary layer thickness of  $\delta/h = 5$  in

a low speed wind tunnel. Flow visualizations and pressure measurements were performed over bluff bodies with different spanwise and streamwise ratios, i.e.  $w/h$  and  $l/h$  respectively, to determine the critical ratios for which reattachment occurred on top of the bluff body. A strong pressure recovery was observed for a body of  $l/h = 2$ , placed in a rough-wall boundary layer as compared to a body of  $l/h = 1$  in a smooth-wall boundary layer.

Table 2-2 Overview of previous studies on cubes and other 3D bluff bodies.

Authors	$l/h$	$w/h$	$Re_h \times 10^3$	$\delta/h$	Quantities measured
Martinuzzi & Tropea (1993)	1	1 – 60	–	–	$C_p, L_r$
Hearst, Gomit, & Ganapathisubramani (2016)	1	1	11.4, 28.8	2	$L_r$
Akon & Kopp (2016)	2.36	3.1 3.4	110 35	–	$C_p, L_r$
Kim, Ji, & Seong (2003)	3.5	2.38	7.9	16	$L_r, U, V, \text{TKE}$
Castro & Robins (1977)	1	1	–	10	$C_p, U, V, W, \overline{u'u'}$
Castro & Dianat (1983)	1– 2	1	–	5	$C_p, U, V, W, \overline{u'u'}$
Sousa (2001)	1	1	3.2	–	$U, V$
Nakamura, Igarashi & Tsutsui (1999)	1	1	4 – 33	1.5 - 1.8	$C_p$
Hussein & Martinuzzi (1996)	1	1	–	–	$U, V, \overline{u'u'}, \overline{v'v'}, \overline{u'v'}, C_p$

This was indicative of an earlier reattachment for high turbulent flows. The minimum length of the body for which reattachment occurred, labeled as the critical body length, was also plotted as a function of the spanwise aspect ratio for both smooth and rough upstream boundary layer cases. For the smooth case, the critical  $l/h$  increased as  $w/h$  was increased up to an asymptotic value of  $l/h = 2$ . The same trend was observed for the rougher case; however, a lower critical length was observed, i.e.  $l/h = 1$ . This was expected as turbulence generated by wall roughness promotes an earlier reattachment.

An experimental investigation of the flow around surface-mounted cubes immersed in uniform, irrotational and turbulent flows is presented in detail by Castro & Robins (1977). They identified a horseshoe vortex that wraps itself around the body, the physical size of the vortex being determined by the boundary layer thickness. The vortex promotes turbulent mixing near the base of the body which entrains fluid into the base region thereby relieving the pressure.

Hussein & Martinuzzi (1996) performed an experimental investigation of the three-dimensional flow around a surface-mounted cube in a channel. A cube of height,  $h = 25\text{mm}$  and blockage ratio of 50%, was placed in open, blower-type air channel. A laser Doppler anemometry (LDA) was used to measure the single-point velocity correlations to provide insight into the production, convection and transport of the turbulence kinetic energy in the bluff body wake. They observed that for smaller  $w/h$  (3D surface-mounted bluff bodies), most of the flow ( $\sim 50\%$ ) was deflected along the sides of the bluff body whereas it was deflected on top of the bluff body for larger aspect ratio. This gives rise to smaller reattachment lengths for 3D cases.

Kim et al. (2003) investigated flow around a 3D FBFS using a PIV technique. In this study, a prism of dimensions  $l/h = 3.5$  and  $w/h = 2.38$ , was immersed in a thick boundary layer, i.e.  $\delta/h = 16$

at  $Re_h = 7900$ . The reattachment lengths were  $1.01h$  and  $1.9h$ , respectively, for the separation bubbles on the bluff body and downstream of the bluff body. The maximum kinetic energy was observed at the leading edge of the prism and was 2.5 times higher than that in the wake region.

Akon & Kopp (2016) investigated the effects of the aspect ratio and turbulent intensity on the reattachment length and turbulence characteristics for 3D surface-mounted bluff bodies. Using a PIV, two aspect ratios,  $w/h = 3.1$  and  $3.5$ , and a range of turbulent intensities (10% to 26%) were examined. For aspect ratio of 3.1, it was observed that the reattachment length decreased from 1.49 to 0.67 when the turbulence intensity increased from 10% to 22%. Meanwhile, the reattachment length for aspect ratio of 3.5 decreased from 1.29 to 0.87 with an increase in turbulence intensity from 14% to 26%.

Hearst et al. (2016) also investigated the effect of turbulence intensity on the wake of a turbulent boundary layer by varying the turbulence intensity from 6.3 to 9%. Separation occurred at the leading edge and attached intermittently onto the top of the cube. An increase in the turbulent intensity was shown to promote wake recovery i.e. reduce the reattachment length. This reduction was attributed to the reduction in the strength of the dominant shedding motions. The intermittency of the recirculation bubble was also shown to reduce with increasing turbulent intensity.

Martinuzzi & Tropea (1993) study of the flow around surface-mounted bluff bodies using flow visualisation and static pressure measurements. A prism of height,  $h = 25$  mm,  $l = 25$  mm, and spanwise width which varied from  $w/h = 1$  to 8, was placed in a fully developed channel flow with a blockage ratio of 50%. The flow was observed to reattach downstream of the bluff body due to the limited streamwise aspect ratio, i.e.  $l/h = 1$ . They found that the reattachment length increased with the aspect ratio and became asymptotic at  $w/h = 10$ . Pressure measurements

revealed that the recovery length downstream of the bluff body is shorter for a three-dimensional bluff body due to the flow being dominated by the interaction of the horseshoe vortex with the corner vortex and mixing layer behind small aspect ratios (i.e.,  $w/h < 4$ ). This interaction also makes the flow around a 3D bluff body more complex compared to their 2D counterparts. This is the only study in which the spanwise aspect ratio was systematically varied from 3D through transition to 2D regime. However, only the reattachment length and pressure measurements were reported which is not sufficient to understand the detailed behaviour of the separated region on the bluff body.

## **2.4 Summary of Previous Studies on Geometry-Induced Separated and Reattached Flow**

Geometry-induced separated and reattached flows have been studied quite extensively. The geometries of interest include forward-, backward-, forward-backward-facing steps (two-dimensional); and cubes and surface-mounted bluff bodies (three-dimensional). The reattachment length and turbulent properties have been shown to be strongly dependent on several upstream conditions including roughness, Reynolds number and relative boundary layer thickness. Despite the extensive study of 2D and 3D bluff bodies, the literature is lacking in a detailed examination of the transitional spanwise aspect ratio. Thus, the focus of this thesis is to fill this knowledge gap by systematically investigating the effects of spanwise aspect ratio of surface-mounted bodies immersed in a thick turbulent boundary layer using a time-resolved particle image velocimetry.

## **Chapter 3 Experimental Setup**

This chapter presents a detailed description of the experimental setup, the surface-mounted bluff bodies used to induce flow separation and to assess the effects of spanwise aspect ratio on the characteristics of the separated shear layers. The test conditions as well as the time-resolved particle image velocimetry system used to perform the velocity measurements in this study are also described.

### **3.1 Test Section and Rough Wall**

The experiments were conducted in a recirculating open water channel shown in Fig. 3-1. The length, width and height of the test section are, respectively, 6000 mm, 600 mm and 450 mm. The side and bottom walls of the channel were fabricated from smooth 31.8 mm thick super abrasion resistant (SAR) transparent acrylic plates that facilitate optical access. The recirculating flow was driven by a pump with a maximum flow rate of 33950 LPM through a series of flow conditioning units, including a perforated plate, a hexagonal honey-comb, mesh screens and a 4.88:1 converging section. A 40HP variable-speed drive motor was used to regulate the speed of the pump.

As shown in Fig. 3-2, the flow at the inlet was tripped by a two-dimensional tooth barrier placed at the leading edge of the channel, followed by an upstream rough wall made of staggered cubes of height 3mm, to promote a rapid transition of the approach boundary layer to turbulence and the development of a thick boundary layer. The toothed barriers had a height of 15 mm, with triangular

cut-outs at the top of pitch 15 mm and depth 12 mm and span 0.075 m from the leading edge of the channel.



Figure 3-1 Test facility.

The upstream rough wall spans a total length of 4 m and extended across the entire width of the channel floor. The cubes were machined from a 6 mm acrylic plate and had center-to-center spacing of 3 mm in both the streamwise and spanwise directions. Bluff bodies of nominal height,  $h = 30$  mm and length,  $l = 70.8$  mm, and width ranging from  $w = 30$  mm to 600 mm (resulting in  $w/h = 1, 2, 3, 3.5, 4, 5, 8, 12$  and 20) were mounted on a smooth plate with length  $\times$  breadth of 400 mm  $\times$  600 mm and a thickness of 6 mm (to match the combined thickness of the upstream rough plate) was screwed unto the channel floor and was of equal height as the upstream rough wall (as shown in Fig. 3-2). The smooth plate and bluff bodies both had their leading edges

immediately downstream the upstream roughness plate. The bluff bodies, plate and roughness cubes immediately upstream of the bluff body were painted with black non-reflective paint to minimise reflection of the laser.

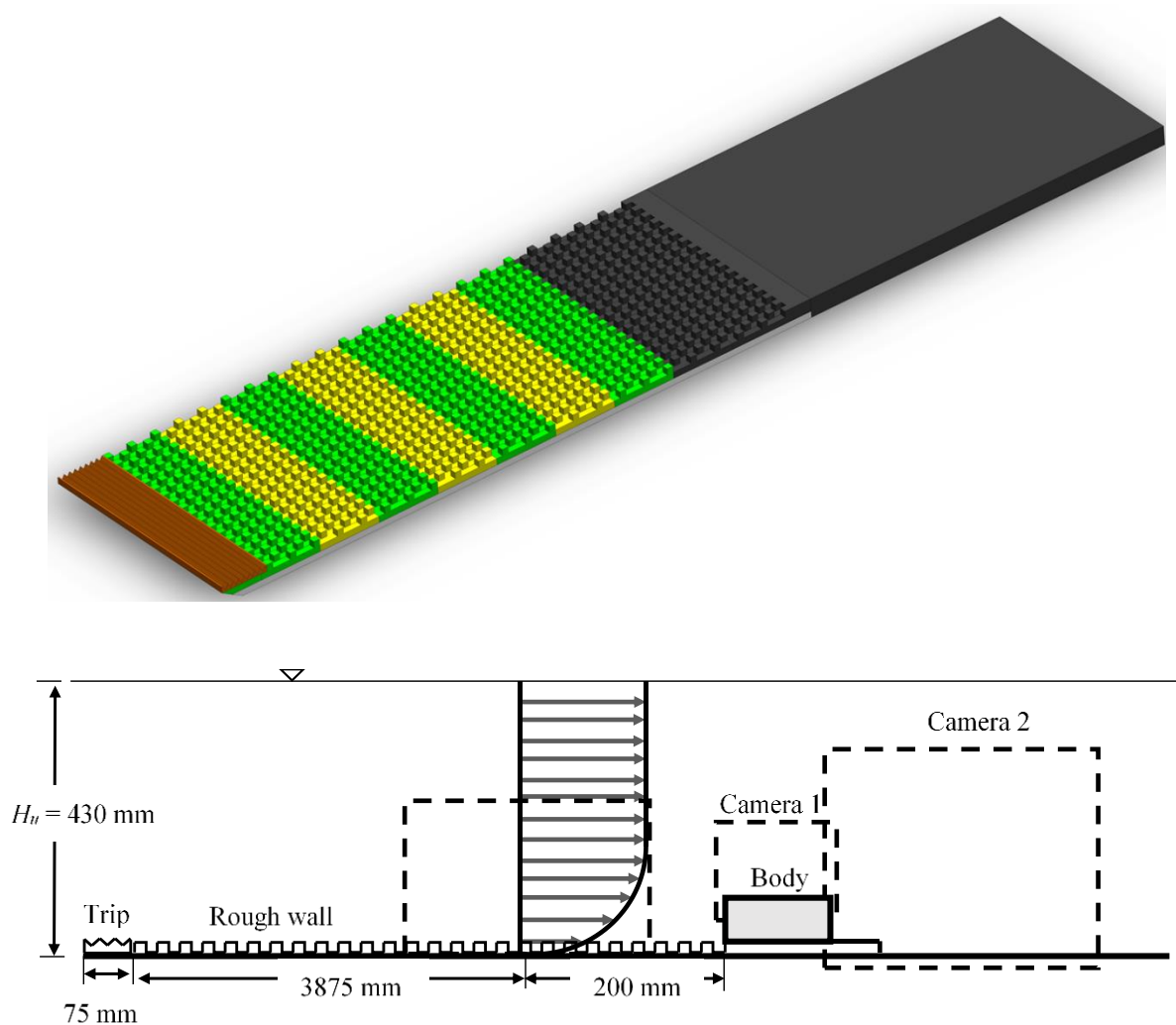


Figure 3-2 Schematic of experimental setup showing upstream roughness and block at aspect ratio 20: a) three-dimensional view, b) sectional view.

### 3.2 Test Conditions

The water depth and freestream velocity were maintained at  $H_u = 430$  mm and  $U_e = 0.41$  m/s, respectively, throughout the experiments. The room temperature was set at 20°C, yielding a kinematic viscosity of the working fluid ( $\nu$ ) of  $10^{-6}$  m<sup>2</sup>/s. For all test cases, the bluff body height was kept constant at  $h = 30$  mm yielding a blockage ratio,  $h/H_u = 0.07$ . The width to height ratio,  $w/h$ , of the bluff body was varied from 1 to 20, with the aim of investigating the effects of aspect ratio. The Reynolds number based on the body height,  $Re_h (= U_e h/\nu)$ , was 12500, and the Froude number,  $Fr_H (= U_e/\sqrt{gH_u})$  was 0.2 which ensured that the water surface was free of waves. The streamwise mean velocity at the body height ( $U_h$ ), is a more appropriate velocity scale than  $U_e$  since the boundary layer thickness is significantly larger than the body height and is used in the analysis. This approach has been adopted in previous studies in which the bluff body is submerged in a thick TBL (Castro, 1979; Lim et al., 2007; and Fang & Tachie, 2019).

### 3.3 Time-Resolved Particle Image Velocimetry

The particle image velocimetry (PIV) is a widely used tool in the experimental study of fluid flows. The PIV measures instantaneous velocities in 2D (planar) and 3D (volumetric) flow regions with high spatial resolution. A planar time-resolved PIV (TR-PIV) was employed in this study. The typical setup is shown schematically in Fig. 3-2. A PIV system consists of a laser source to illuminate the flow field, a camera used to capture the flow field and a data acquisition system to acquire and process the captured images. Firstly, the flow is seeded with tracer particles assumed to faithfully follow the fluid motion. The flow field is then illuminated by a pulsed sheet of high-

intensity laser light, fired at precise time intervals. The light scattered by the tracer particles are captured by a complementary metal-oxide semiconductor (CMOS) camera. The images are then subdivided into grids and each grid is called an interrogation area (IA). A numerical correlation algorithm is then applied to statistically determine the local displacement vector ( $\Delta x$ ) of particles between the first and second image for each IA. The velocity vector for each IA is then obtained by dividing  $\Delta x$  by  $\Delta t$ , which is repeated for all the IAs to obtain the velocity vector map of the entire flow field.

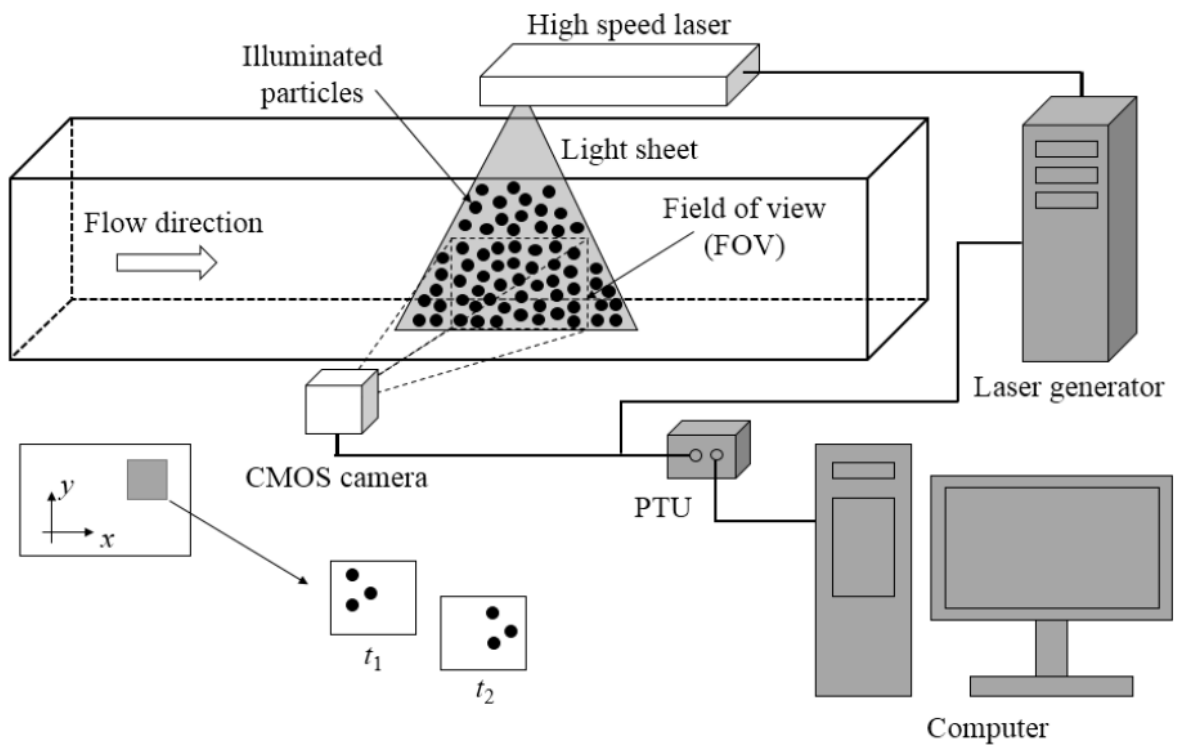


Figure 3-3 Typical setup of a time-resolved particle image velocimetry (TR-PIV) (Nematollahi, 2019).

### 3.3.1 Particle Illumination and Recording

On account of their high-energy density monochromatic light that can be transformed into thin sheets of light, lasers are used to illuminate seeding particles in PIV. A laser comprises of three main components, which are the laser material consisting of atomic or molecular gas, semiconductor or solid material, the pump source that excites the laser material by electromagnetic energy or chemical energy, and the mirror arrangement allowing an oscillation within the laser material. The need for high-speed, time-dependent turbulence applications has led to the development of high repetition rate lasers capable of delivering pulse bursts of up to 1 kHz – 1 MHz. An example is the Neodymium: Yttrium Lithium Fluoride (Nd:YLF) dual-pulse laser which was employed in this study. It has a pulse width of about 129 ns and wavelength 527 nm that delivers a total energy of 30 – 60 mJ/Pulse at 1 kHz – 10 kHz.

The intensity of the light sheet produced by the laser is considered to follow a Gaussian distribution of the form:

$$I = I_o \exp(-8z^2/d_l^2) \quad (3-1)$$

where  $I_o$  is the peak intensity of the sheet and  $d_l$  is the light sheet thickness, defined at the  $I_o e^{-2}$  intensity level (i.e., where  $z = d_l/2$ ).

To capture the images of the illuminated particles, high-spatial resolution cameras such as the charge-coupled device (CCD) camera are used. The cameras are synchronized with the laser to allow image acquisition within the duration of the pulse. Typical commercially available CCD cameras are however limited to the acquisition of relatively few image pairs per second.

Consequently, the development of high-speed cameras such as the complementary metal-oxide semiconductor (CMOS) camera allows achieving up to kilohertz (kHz) image acquisition rates. Coupled with the high-repetition rate lasers, the CMOS camera becomes an extremely valuable tool for performing time-resolved PIV measurements. The availability of the high-speed CMOS cameras allows turbulence research into rapidly evolving time-dependent flow phenomena as found in separating and reattaching flows around bluff bodies.

### 3.4 Measurement Procedure

A high-resolution planar TR-PIV system, which consists of a high repetition-rate laser source, a high-speed camera, and data acquisition system was used to perform the velocity measurements. The flow was seeded with 10  $\mu\text{m}$  silver coated hollow glass spheres with specific gravity of 1.4, and illuminated by a Photonics DM30-527DH dual-head high-speed Nd:YLF laser that emits green light up to a maximum of 30 mJ/pulse for each laser at  $\lambda = 527 \text{ nm}$ .

The slip velocity of the seeding particles was estimated as (Raffel et al., 1998):

$$U_s = \frac{d_p^2 (\rho_p - \rho_f)}{18\rho_f \nu} g \quad (3-2)$$

where  $\rho_p$  and  $\rho_f$  are the density of seeding particles and working fluid (water), respectively. This results in  $U_s = 2.18 \times 10^{-5} \text{ m/s}$ , which is orders of magnitude smaller than the smallest velocity scale of the measured fluid motion. Thus, these seeding particles faithfully follow the flow.

Also, the response time of the seeding particles was estimated as

$$\tau_p = \frac{d_p^2 (\rho_p - \rho_f)}{18\rho_f \nu} \quad (3-3)$$

producing a value of  $\tau_p = 2.2 \times 10^{-6}$  s. The smallest temporal scale ( $\tau_f$ ) in the studied turbulent flow is estimated to be of the order of  $\nu/u_\tau^2 = 1.6 \times 10^{-3}$  s, where  $u_\tau$  is the friction velocity, and is approximately 0.025 m/s. Therefore, the Stokes number

$$S_k = \frac{\tau_p}{\tau_f} = 0.0014 \quad (3-4)$$

which is within the recommended range of  $S_k \leq 0.05$  proposed by Samimy & Lele (1991). It is therefore concluded that the adopted seeding particles followed the fluid motions very well.

A high speed 12-bit Phantom VEO340L complementary metal-oxide semiconductor (CMOS) camera at a full resolution of 2560 pixel  $\times$  1600 pixel was used to capture the images. The pixel pitch of the camera was 10  $\mu$ m. In order to characterize the upstream boundary layer, detailed velocity measurements in the  $x - y$  plane were performed upstream of the bluff body at the mid-span of the channel. This was followed by measurements in the  $x - y$  and  $x - z$  planes over the bodies. For the upstream boundary layer measurements, two sets of measurements were conducted at the mid-span of the water channel without installing the bluff body. The first set of measurements were performed using a larger FOV of 352 mm  $\times$  220 mm in order to capture the entire thickness of TBL. In this case, the images were acquired at a rate of 1000 Hz and a reduced resolution of 1920 pixel  $\times$  1600 pixel in continuous mode. The next set of measurements were performed using a smaller FOV of 160 mm  $\times$  100 mm at a rate of 100 Hz and a full resolution (2560 pixel  $\times$  1600 pixel) in a double-frame mode for the purpose of achieving a better spatial resolution and reliable quantification of second-order moments.

To capture the separation bubbles on top and downstream of the bluff body simultaneously, two cameras positioned side-by-side were used in this experiment with the  $x - y$  plane measurements located at the mid-span of the channel. Camera 1 was fitted with a Sigma DG MACRO 105 mm  $f$  2.8 D lens while Camera 2 was fitted with an AF MICRO NIKKOR 60 mm  $f$  2.8 D lens. The field of view of Camera 1 was set to 78 mm  $\times$  65 mm, while the field of view of Camera 2 was set to 197 mm  $\times$  164 mm. There was an overlap of 13.2 mm in the streamwise direction between the fields of view. In each case, 32000 samples were collected at a sampling rate of 1 kHz and at a reduced spatial resolution of 1920 pixel  $\times$  1600 pixel. For measurements in the  $x - z$  plane, the CMOS cameras were placed above the free surface of the water. An acrylic plate of cross-sectional area of 600 mm  $\times$  600 mm in the  $x - z$  plane and 9 mm thickness was placed beneath the cameras and submerged into the water by 2 mm to prevent distortion of the captured images by the surface waves. The leading edge of the acrylic plate was rounded to further minimize its influence on the flows. The  $x - z$  plane measurements were performed at a vertical distance of  $0.5h$  above the top plane of the roughness cubes and at  $0.1h$  above the bluff bodies. This was to measure the upstream boundary layer and also investigate the turbulent separated flows over the bluff body in the  $x - z$  plane. For these measurements, the sampling frequency was set to 807 Hz which allowed the full resolution of the cameras (2560 pixel  $\times$  1600 pixel) to be used.

The data acquisition was controlled using a commercial software (DaVis version 8.4) supplied by LaVision. The data was processed starting with a grid size of 128 pixel  $\times$  128 pixel with 50% overlap and finally stepping down to an interrogation area of 32 pixel  $\times$  32 pixel with 75% overlap. The vector spacing of the small and large fields of view resulted as 0.33 mm and 0.82 mm respectively. The particle image size was estimated to be 25  $\mu$ m (2.5 pixel). This is within the

recommended 2-4 pixels. The small pixel size reduces the effects of peak locking (Johnson & Smith, 2016).

Following the measurements performed upstream, some relevant boundary layer parameters are summarised in Table 3-1, where  $U_h$  is the velocity at the body height ( $y = h$ ),  $Re_h$  is the Reynolds number based on the body height and freestream velocity, and Tu ( $= u_{rms} / U_h$ ) is the relative turbulence intensity based on the velocity at body height,  $\delta^*$  is the displacement thickness,  $\theta$  is the momentum thickness and  $H$  is the shape factor ( $\delta^* / \theta$ ).

Table 3-1 Upstream boundary layer.

Parameters	$U_e$ (m/s)	$U_h$ (m/s)	$Re_h$	Tu	$\delta/h$	$\delta^*$ (m)	$\theta$ (m)	$H$
Value	0.418	0.285	12500	15.9%	4.8	0.0270	0.0173	1.56

## Chapter 4 Results and Discussion

In this chapter, the effects of spanwise aspect ratio on the instantaneous velocity field as well as the statistical properties of the separated shear layers are discussed. Specifically, the variations of the mean reattachment length on top and behind the bluff bodies as well as the mean velocities, Reynolds stresses and budget terms in the transport equation for aspect ratio 1, 4, 8 and 20 are presented and discussed. The coherent structures are also examined using quadrant analysis, Galilean decomposition, JPDF, two-point correlation and POD.

### 4.1 Instantaneous Flow Visualization

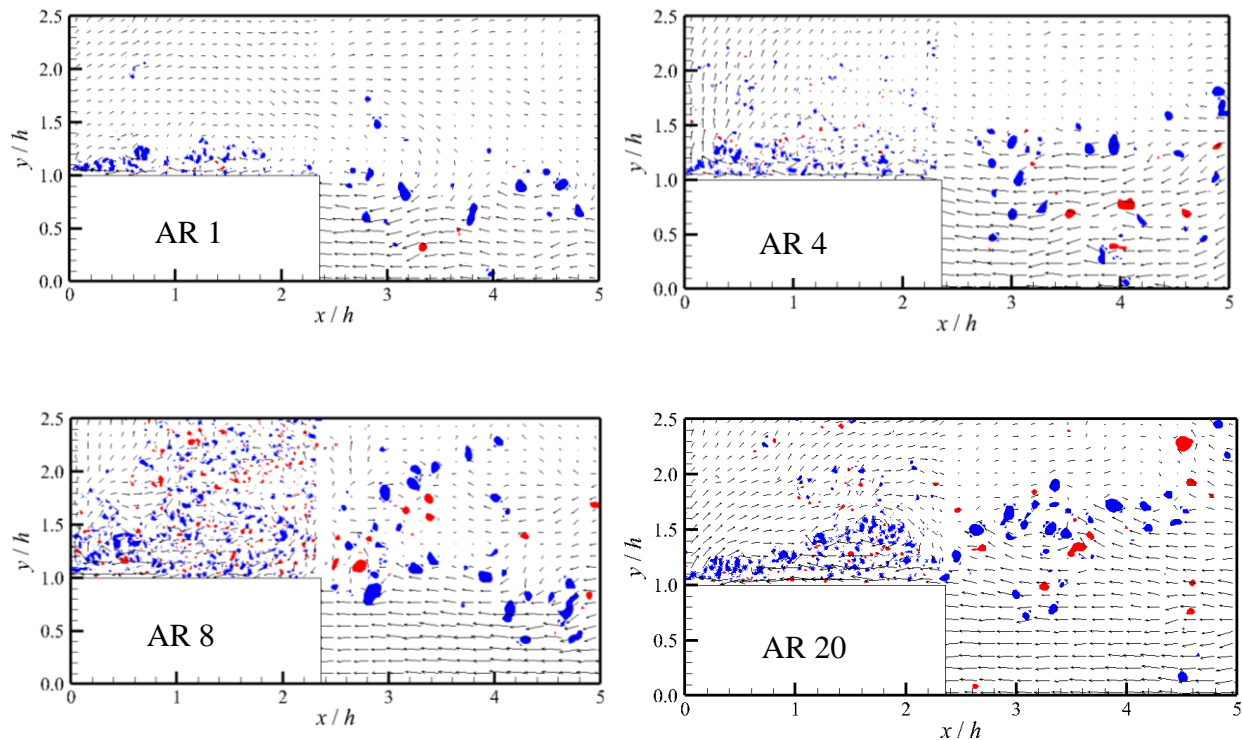


Figure 4-1 Contour plots of the Galilean decomposition of the instantaneous flow fields for aspect ratio (a) 1, (b) 4, (c) 8 and (d) 20.

The separated and reattached regions are highly unstable and dominated by large-scale coherent structures. To analyse the instantaneous large-scale structures in the separated region, Galilean decomposition is applied to the instantaneous velocity field. Figure 4-1 shows the Galilean decomposition of the instantaneous velocity fields for aspect ratios 1, 4, 8 and 20. The vector fields for these test cases were obtained by subtracting a constant convection velocity equal to the velocity at the body height, i.e.  $U_c = U_h$  from the instantaneous streamwise velocities. A convection velocity that is  $0.6 - 0.8 U_e$  have been adopted in past studies (Nematollahi & Tachie, 2018; Volino et al., 2007) to reveal the present vortices. As stated earlier, the velocity at the body height is a more appropriate normalizing scale due to the presence of the significantly larger TBL and is also adopted in the present study as the convective velocity. The velocity at body height,  $U_h$ , represents  $0.6U_e$  and clearly reveals the vortices present in the flow field.

Since the complete 3D velocity gradient tensor was inaccessible, the 2D velocity gradient tensor was used in estimating the values of the swirling strength,  $\lambda_{ci,z}$ , in the  $x - y$  plane. The instantaneous  $\lambda_{ci,z}$  distribution was decomposed into prograde (negative) and retrograde (positive) swirling strength in order to differentiate between clockwise and counter-clockwise swirling motions, respectively. Contours of the prograde (blue  $\lambda_{ci,z}$  patches) and retrograde (red  $\lambda_{ci,z}$  patches) were superimposed on the vector fields as shown in Fig. 4-1. In Fig. 4-1, it is observed that the flow is dominated by prograde swirling motions both on the body and downstream of the body for all aspect ratios. The swirling motions are observed to increase as the aspect ratio increases from 1 to 8 and then decrease from 8 to 20. The prograde swirling motions are also more localised close to the wall, i.e. in the separated region, for aspect ratio 1, but are more diffused into

the outer layer from aspect ratio 1 to 4 and 4 to 8. The swirling motions for aspect ratio 8 case is highly concentrated and extend further away from the wall than in the other cases.

## 4.2 Distributions of Mean Velocities and Reynolds Stresses

To better understand the effects of the spanwise aspect ratio on the mean flow, contours of the mean streamwise and wall-normal velocities for aspect ratios 1 and 20 are presented in Fig. 4-2. The mean velocities are normalized by the velocity at the body height ( $U_h$ ) and the  $x$  and  $y$  values are normalized by the body height ( $h$ ). The contour plots are shown in Fig. 4-2(a) and (b) for AR 1 and 20, respectively. A general trend was observed as the aspect ratio was varied from 1 to 20. Firstly, two separation bubbles are identified at the leading and trailing edges of the bluff body, which is consistent with other intermediate streamwise aspect ratio surface-mounted bluff bodies. Castro & Robins (1977) performed measurement studies over a 3D bluff body of  $l/h = 1$  and 2 at  $\delta/h = 5$ . They observed that for the  $l/h = 1$  case, one large separation bubble was observed from the leading edge and reattached at a distance downstream of the body as compared to two separation bubbles at the leading and trailing edges of the body of  $l/h = 2$ . Kim et al. (2003) also performed PIV measurement studies over a 3D bluff body with  $l/h = 3.5$  at  $\delta/h = 16$  and observed a separation bubble at the leading and trailing edges.

Secondly, the separation bubble at the leading edge is quantitatively smaller in size than that at the trailing edge.

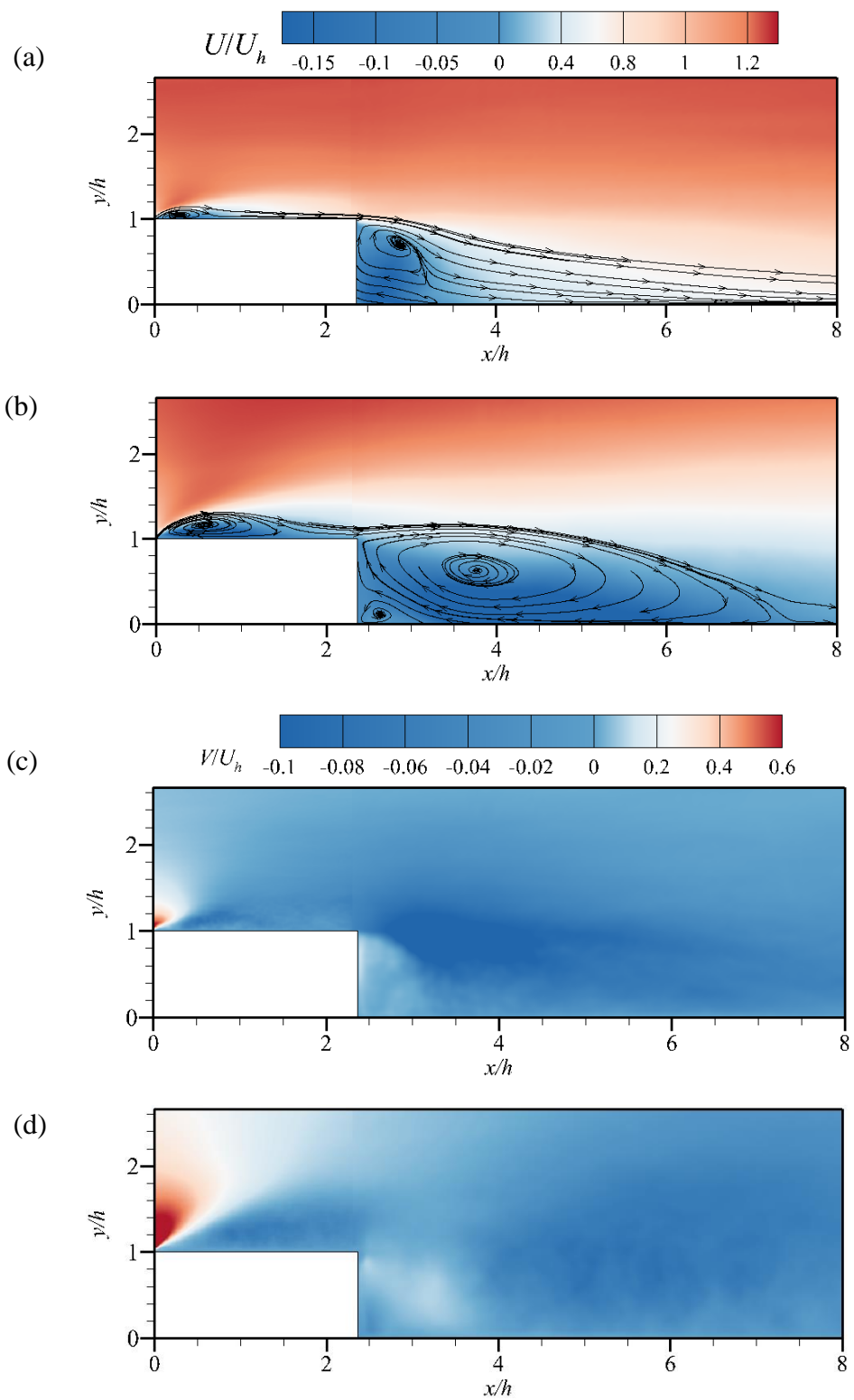


Figure 4-2 Contours of streamwise mean velocity for AR (a) 1 and (b) 20, and wall-normal mean velocity for AR (c) 1 and (d) 20.

Separation and reattachment are also dependent on the aspect ratio. An increase in the aspect ratio was accompanied by an increase in the size of the separation bubbles on top of and behind the bluff bodies. The smaller recirculation bubble in the smaller aspect ratios may be attributed to a higher mixing due to the flow being forced over and around the bluff body (Martinuzzi & Tropea, 1993). At aspect ratio of 20, all of the flow is forced over the body and there are no end effects. The separation bubble on the body and downstream of the body are similar to that of FFS and BFS, respectively. The maximum backflow within the recirculation bubbles over and downstream of the bluff bodies also increase with spanwise aspect ratio. On the bluff body, for example, the maximum backflow increased from  $0.13U_h$  to  $0.35U_h$  as the aspect ratio increased from 1 to 20. Downstream of the bluff body, the maximum backflow increased from  $0.21U_h$  to  $0.35U_h$  as the aspect ratio increased from 1 to 20.

The wall-normal mean velocity is examined in Fig. 4-2(c) and (d) for AR 1 and 20, respectively. Regions of positive (near the leading edge of the step) and negative velocity (on top of the step) are observed in both aspect ratios. The positive velocity region near the leading edge of the body signifies the upward transport of low momentum near front corner of the step into the outer high momentum flow. The negative velocity region, on the other hand, shows the downward transport of high momentum flow into the low momentum zone on top of the body and the downstream wall. The area of positive velocity region is larger for AR 20 as compared to AR 1, which signifies an increase with increasing aspect ratio. This shows that the ability of the lower momentum boundary layer to diffuse into the outer higher momentum flow increases as aspect ratio increases. On the other hand, in the negative velocity region, the opposite is trend observed, i.e. there is a reduction in the downward transport of high momentum flow into the low momentum zone on top

of the body and the downstream wall as the flow transitions from a 3D to 2D. This can be linked to the larger separation bubble in the higher aspect ratio cases.

In Fig. 4-3, the separation bubble is quantitatively analysed by plotting the reattachment length as a function of the aspect ratio. The reattachment point was determined using the zero contour levels of the mean velocity and the streamlines, at the point where the separating streamlines reattached to the top or downstream of the bluff body. As shown in Fig. 4-3(a), the reattachment length on top of the bluff body increases monotonically as the aspect ratio increases from  $w/h = 1$  to 8, with a slope ( $dl_r/dw$ ) of 0.13, and thereafter,  $l_r/h$  approaches an asymptotic value of 1.6. This indicates that for bluff bodies of  $w/h > 8$ , the influences from sidewalls on the mean flow at mid-span of the channel are negligible. This observation is similar to Castro & Dianat (1983) who noted that aspect ratio,  $w/h > 10$  is sufficient for the mean flow in the central region to be independent of side wall effects. The present asymptotic value is in agreement with Fang & Tachie (2019) who reported  $l_r/h = 1.6$  over a FBFS of  $l/h = 2.36$  and  $\delta/h = 4.8$ . Nematollahi & Tachie (2018) investigated the effects of upstream roughness on an FFS using sandpaper and cube roughness elements at  $\delta/h = 6.7$ . They reported  $l_r/h = 1.23$  and 1.78 for cube and sandpaper roughness respectively. The cube roughness, similar to the present study, produced a comparably lower reattachment length value. This difference may be attributed to the lower  $\delta/h$  value of the present study. Largeau & Moriniere (2006) also reported  $l_r/h = 3.5$  to 3.8 for different aspect ratios ( $l/h = 15, 18.7$  and 25). The relatively longer reattachment lengths reported in their study may be attributed to the fact that their experiments were performed at  $\delta/h = 0.16$  to 0.26, which is significantly lower compared to  $\delta/h = 4.8$  used in the present study.

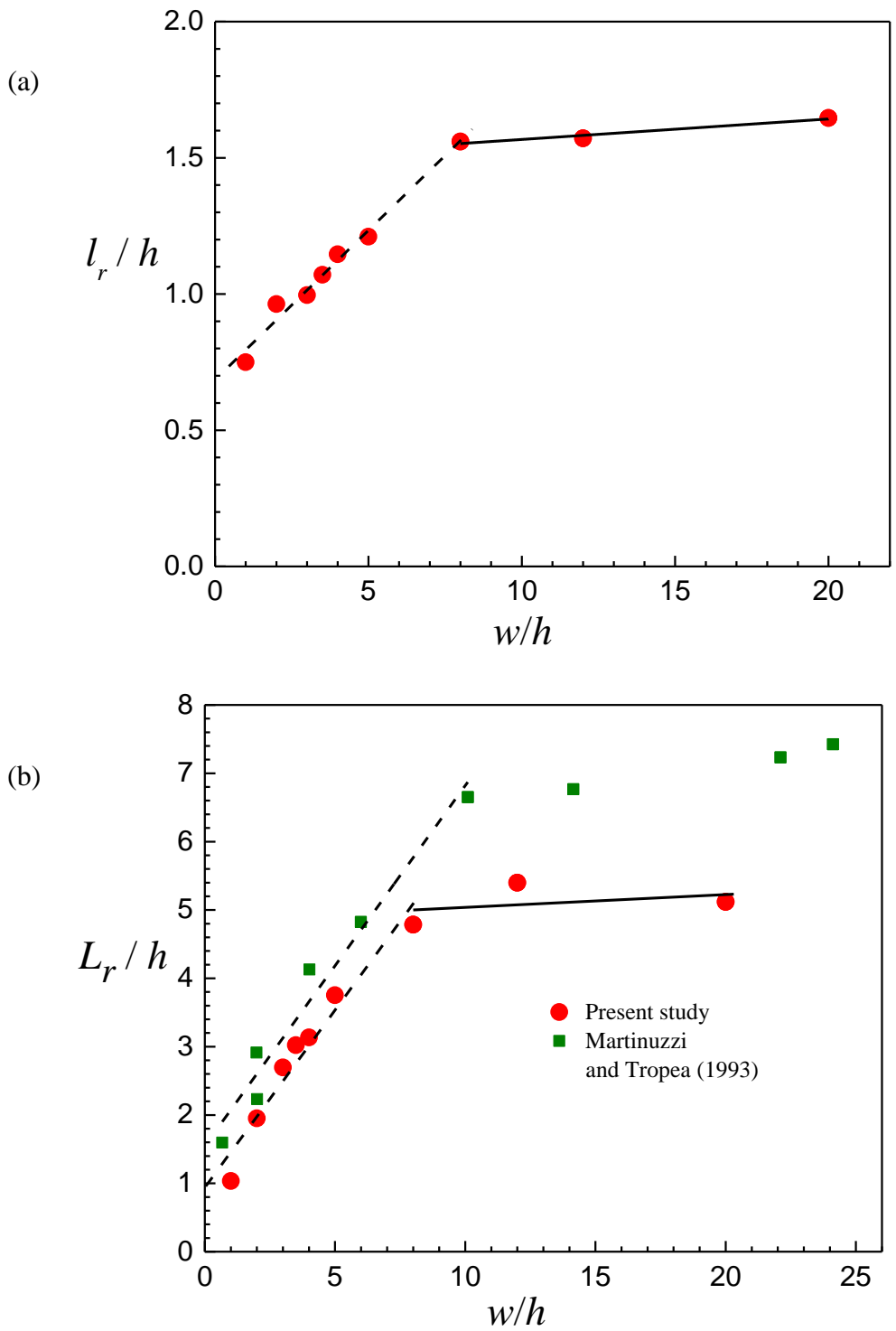


Figure 4-3 Reattachment length of separation bubble at the leading and trailing edges as function of the aspect ratio: a) separation at leading edge; b) separation at trailing edge.

For the separation downstream of the bluff body, it is observed from Fig. 4-3(b) that the reattachment length increases as the aspect ratio increases from  $w/h = 1$  to 8 and becomes asymptotic at  $L_r/h = 5.3$ . This value is in good agreement with  $L_r/h = 5.1$  reported by Ampadumintah & Tachie (2015) in the BFS experiment. Essel & Tachie (2015) reports a relatively higher reattachment length of  $5.8h$  to  $6.2h$ . The present results are also compared to those from Martinuzzi and Tropea (1993) which were obtained for square ribs ( $l/h = 1$ ) in a fully developed channel flow, and the reattachment lengths were measured from the trailing edge. It is observed that the reattachment length in the present study is lower than that of Martinuzzi & Tropea (1993). These differences may be attributed to differences in streamwise length to height ratio ( $l/h$ ). The reattachment length varied linearly with an increase in aspect ratio 1 to 8, with a slope,  $dL_r/dw = 0.52$ , which compare favorably to  $dL_r/dw = 0.53$  reported in the study of Martinuzzi & Tropea (1993).

Figure 4-4 shows the mean flow in the  $x - z$  plane at half body height ( $y/h = 0.5$ ) away from the bottom wall for the AR 1, AR 3.5 and AR 8 cases. A distinct recirculation motion occurs in the wake region near the spanwise ends of the bluff bodies. In AR 1, the distance between the vortex core and mid-span is approximately  $0.38h$ . This distance is identical to that observed by Yakhot et al. (2006) in the wake flow behind a cube.

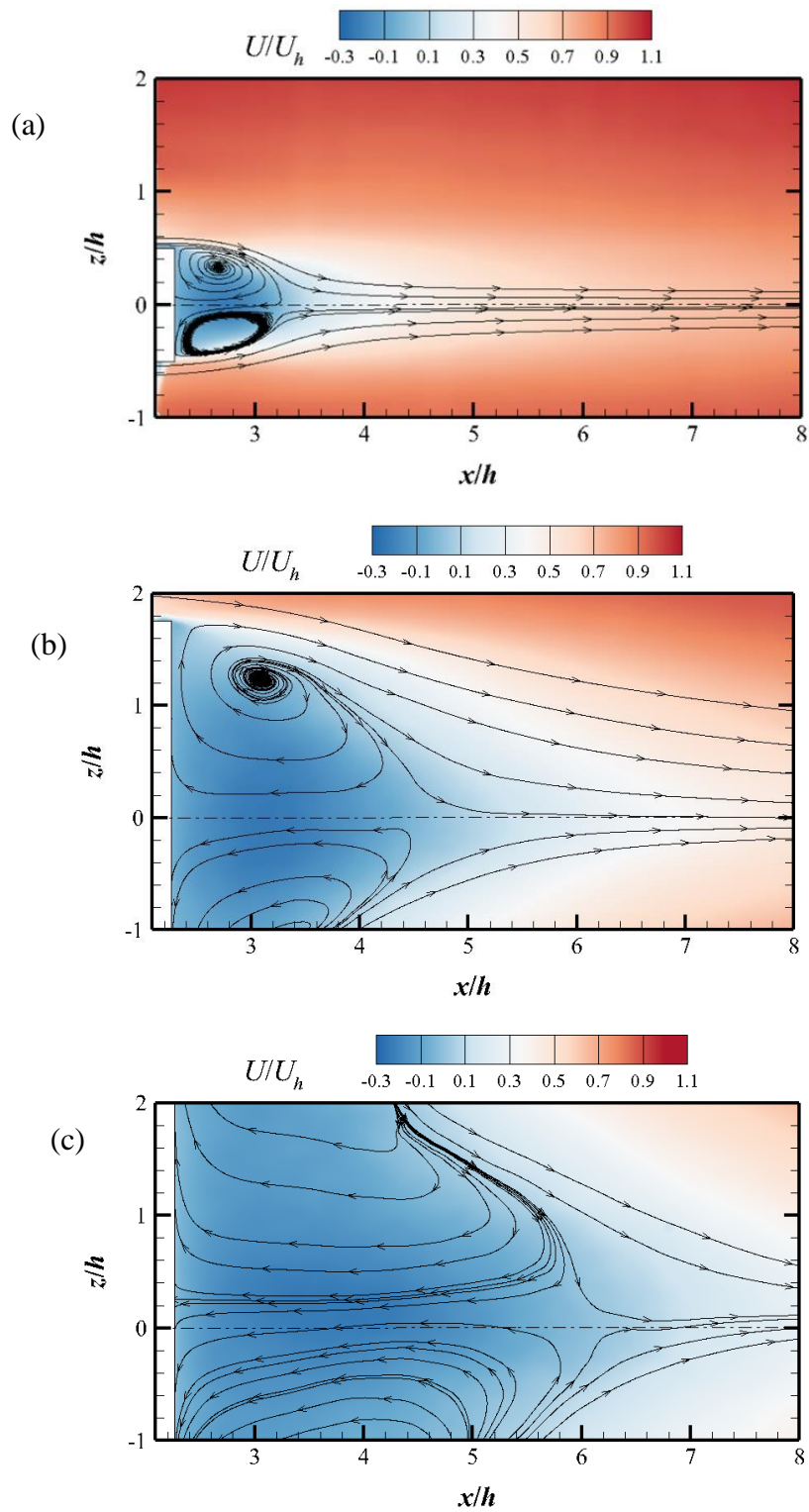


Figure 4-4 Mean flow in the  $x - z$  plane at half body height ( $y/h = 0.5$ ) of AR a) 1 b) 3.5 and c) 8.

As the aspect ratio increases, the vortex core moves farther away from the mid-span. This is consistent with the observation made by Martinuzzi & Tropea (1993) using oil film on the bottom wall. Specifically, the vortex cores at  $y/h = 0.5$  in the AR1, AR 3.5 and AR 8 cases occur at  $z/h = 0.38, 1.24$  and  $2.14$ , respectively.

To characterise the growth of the shear layer, the vorticity thickness is examined in Fig. 4-5. Brown & Roshko (1974) define the vorticity thickness for a mixing layer as:

$$\delta_w = (U_e - U_{min})/(\partial U/\partial y)_{max}, \quad (4-1)$$

where  $U_{min}$  represents the minimum mean streamwise velocity in each  $x/h$  location in the shear layer. This definition has been adopted for a separated shear layer (Thacker et al., 2013; Nematollahi & Tachie, 2018) and is applied in the present study. The development of two separation bubbles due to an intermediate aspect ratio leads to the existence of two shear layers emanating from the leading and trailing edges of the body. This makes the shear layer of the intermediate aspect ratio bluff body more complex than that of an FFS or BFS.

Figure 4-5 examines the growth of the shear layer at AR 1, 4, 8 and 20. Figure 4-5(a) examines the streamwise development of the velocity difference over the body. For all aspect ratios, the velocity difference increases initially, and peaks close to the leading edge of the body, after which it decreases and then remains constant. The peak value increases as the aspect ratio increases; a 14% increase was observed from  $w/h = 1$  to 20. In Fig. 4-5(b),  $(\partial U/\partial y)_{max}$  of the shear layer is plotted. It is observed that the shear layer developed at the leading edge of the step, due to the adverse pressure gradient, decays with increasing streamwise distance, up to the point of reattachment.

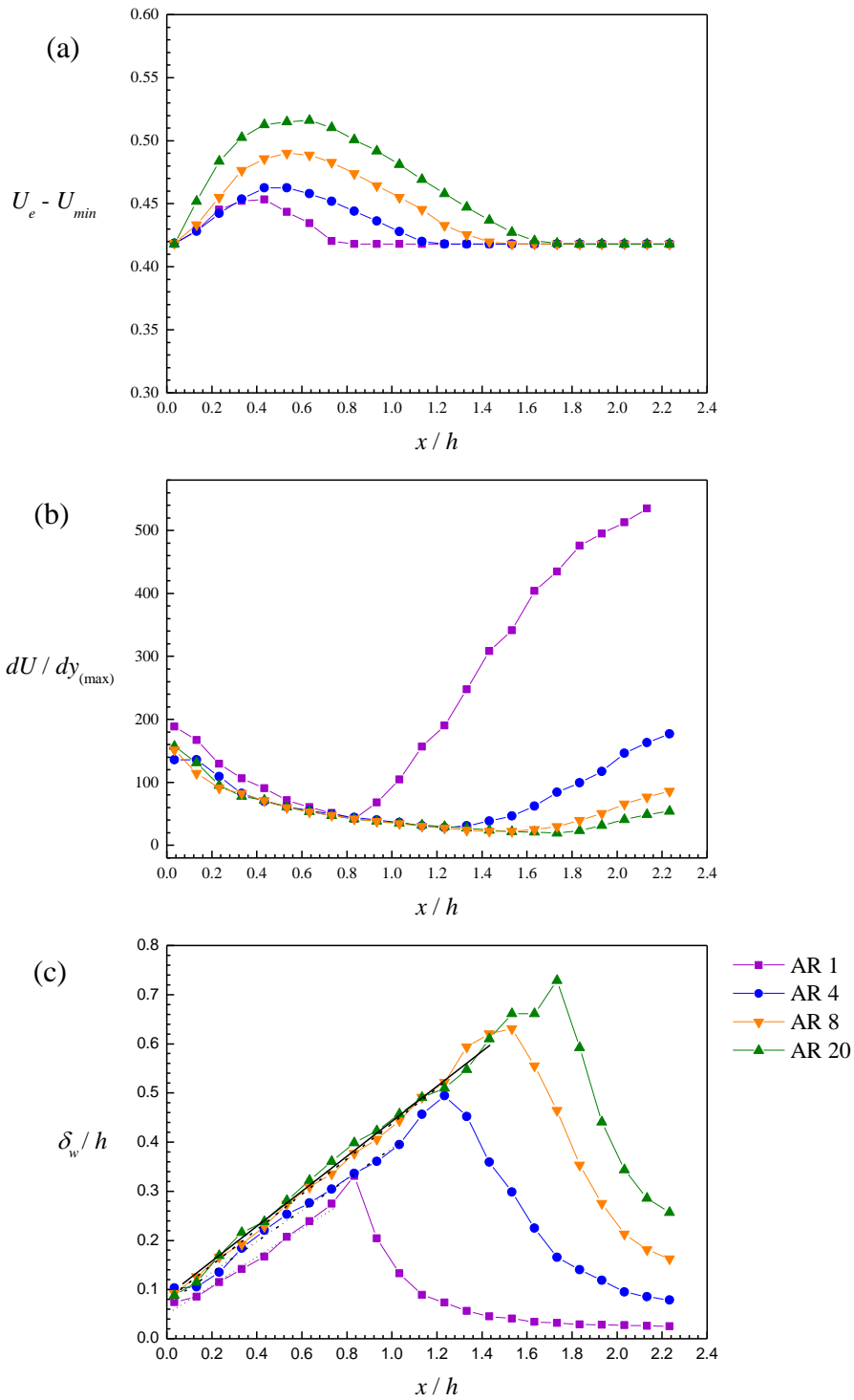


Figure 4-5 Growth of shear layer.

After reattachment, a new shear layer develops at the wall and increases further downstream. The vorticity thickness is plotted for aspect ratio 1, 4, 8 and 20 to investigate the effect the transition from a 3D to 2D flow regime has on the growth on the shear layer. Figure 4-5(c) represents the vorticity thickness of the shear layer emanating from the leading and trailing edges. In Fig. 4-5(c), it is observed that in all cases, the vorticity increases linearly with increasing streamwise distance for the first part over the bluff body. This linear development has been observed in other separated and reattached flows (Fang & Tachie, 2019; Nematollahi & Tachie, 2018; Thacker et al., 2013). The vorticity thickness,  $\delta_w/h$ , has a linear development in the streamwise direction with a slope that varies with aspect ratio. The slope is recorded as  $d\delta_w/dx = 0.29, 0.31, 0.34$  and  $0.35$  for AR 1, 4, 8 and 20 respectively. This represents a 20% increase from aspect ratio 1 to 20. This value agrees with other bluff body induced separation studies (Fang & Tachie, 2019) who reported a value of  $d\delta_w/dx = 0.3$ . This value is considerably higher than that observed in other two-dimensional geometry-induced separated flows (Thacker et al., 2013; Nematollahi & Tachie, 2018). After the point of reattachment, vorticity due to the wall shear develops. This point varies with the different aspect ratio cases with different reattachment points.

Figure 4-6 shows the contour plots of the Reynolds stresses for AR 1 and AR 20, and normalised by  $U_h^2$ . In all cases, the Reynolds stresses are observed to possess peak values at their leading edges which is followed by a decay in streamwise direction. This is attributed to the high turbulent intensity of the incoming TBL which was reported by Samson & Sarkar (2015) to cause an early turbulence transition of the separating shear layer at the leading edge. The contour plots of the streamwise Reynolds normal stress are presented in Fig. 4-6(a) and (b). A region of elevated turbulence level is observed at the leading edge which is shown to be significantly larger over AR

20 compared to AR 1. Figures 4-6(c) and (d) represent the contour plots of the wall-normal Reynolds normal stress at AR 1 and 20, respectively. The transition of the flow regime from 3D to 2D is followed by an increase in  $\overline{v'v'}$ .

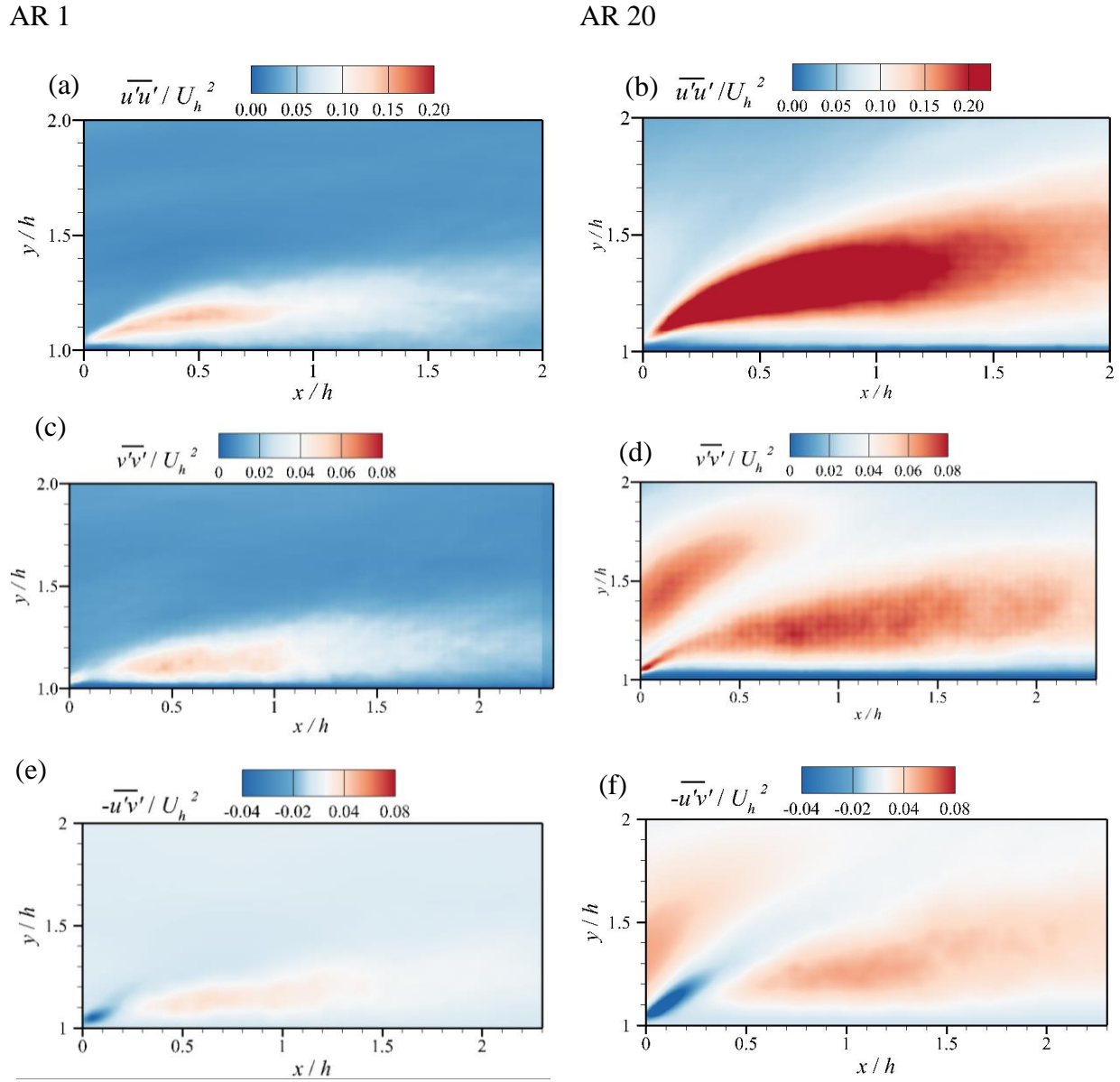


Figure 4-6 Contour plots of Reynolds stresses of AR (a) 1 (left column) and (b) 20 (right column).

For AR 20, a double peak is also observed at the leading edge of the bluff body which is consistent for other separated flow studies at high turbulent intensity (Fang & Tachie, 2019).

Figures 4-6(e) and (f) show contours plots of the Reynolds shear stress over the bluff bodies with  $w/h = 1$  and 20, respectively. A notable observation is the occurrence of a region of negative Reynolds shear stress at the leading edge of the bluff body which is followed by a region of positive Reynolds shear stress. This pattern is true for both aspect ratios, and has been observed in previous investigations of FFS (Essel et al., 2015 ; Hattori & Nagano, 2010; Sherry et al., 2010; Nematollahi & Tachie, 2018). Hattori & Nagano (2010) attributed the regions of negative  $-\overline{u'v'}$  to the countergradient diffusion phenomenon (CDP) that results in a negative contribution to the turbulence total kinetic energy. The large peak values of positive  $-\overline{u'v'}$  present on the bluff body signifies strong turbulent mixing process as a result of the entrainment of high-momentum freestream fluid into the recirculation region over the bluff body (Hattori & Nagano, 2010). The magnitudes of the negative and positive Reynolds shear stress increase with increasing the aspect ratio. However, the region of negative  $-\overline{u'v'}$  is considerably larger than the positive  $-\overline{u'v'}$  region, irrespective of aspect ratio.

The observation of negative  $-\overline{u'v'}$  at the leading edge is different than observed in other canonical TBL and geometry-induced separated flow (Mohammed-Taifour & Weiss, 2016). This deviation is further examined by analyzing contours of the eddy kinematic viscosity. The eddy kinematic viscosity is normalised by the kinematic viscosity and presented for AR 1 and 20 in Fig. 4-7(a) and (b) respectively. In standard eddy kinematic viscosity models,

$$-\overline{u'v'} = \nu_t (\partial U / \partial y + \partial V / \partial x) \quad (4-2)$$

where the Reynolds shear stress and the mean strain are of the same sign thereby producing an eddy kinematic viscosity of positive value.

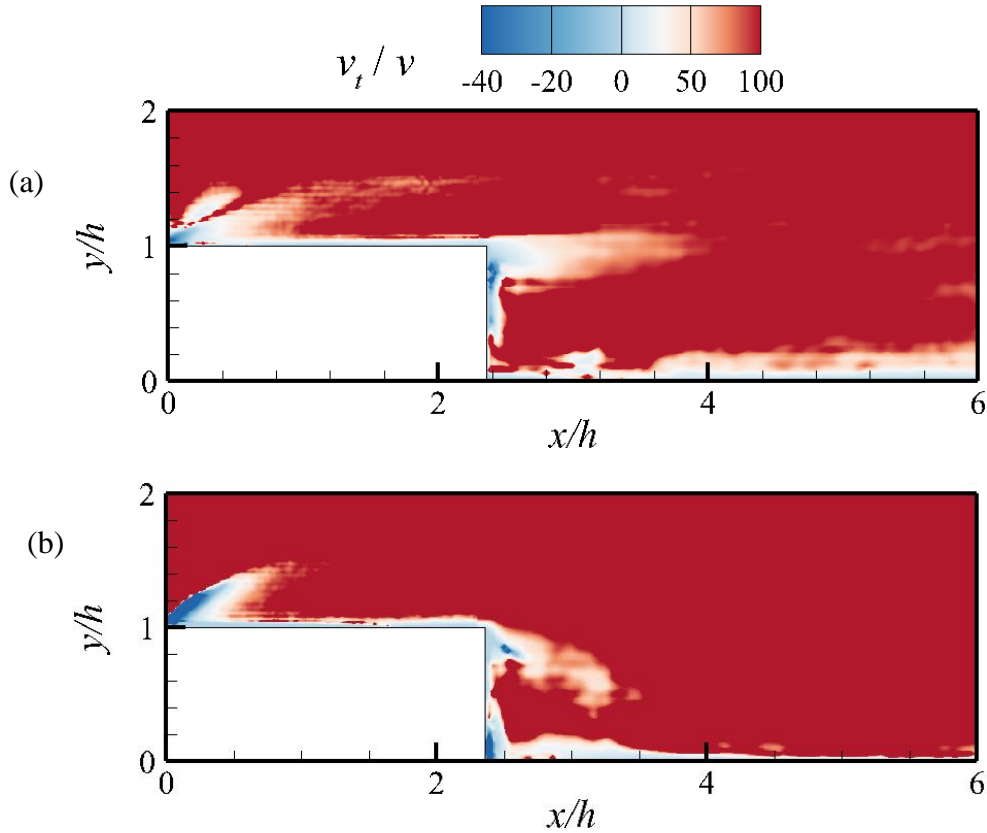


Figure 4-7 Contour plots of eddy kinematic viscosity of AR (a) 1 and (b) 20.

However, the contour plots of the eddy kinematic viscosity show a region of negative  $v_t/v$  at the leading edge that coincides with the region of negative  $-\overline{u'v'}$  in Fig. 4-6(e) and (f). This region of negative eddy kinematic viscosity signifies the existence of countergradient diffusion phenomenon at the leading edge and makes it impossible for turbulence models based on equation 4-1 to reliably predict flow of this nature.

The mean velocities and Reynolds stresses are further investigated by assessing the streamwise development of one-dimensional profiles for selected aspect ratio cases. The profiles were plotted at selected locations of  $x/h = 0.25, 0.5, 1$  and  $2$  to show quantitative variations of mean flows in the separation and reattachment regions on the bluff body. The profiles from the various streamwise locations are staggered relative to one another with the origin of each location defined on the top axes to indicate the correct intervals for the axes. In these profiles,  $y/h = 1$  coincides with the top plane of the bluff bodies.

Figure 4-8 presents the one-dimensional profiles of the mean velocities at AR 1, 4, 8 and 20, normalised by  $U_h$ . The one-dimensional profile of the mean streamwise velocity is presented in Fig. 4-8(a). Close to the leading edge, i.e.  $x/h = 0.25$ , the effects of aspect ratio are observed near the wall at  $y/h < 1.2$ . However, as the streamwise distance is increased, the effects of aspect ratio diffuse farther into the outer layer and at  $x/h = 2$ , the effects of aspect ratio are observed as far as  $y/h = 1.6$ . The profiles of the different aspect ratios show a decrease in the velocity with increasing aspect ratio which is coincidental with a larger region of negative velocity over the higher aspect ratios observed in the contour plots in section 4.3. The height of the inflection point grows with streamwise distance.

Figure 4-8(b) shows the one-dimensional profiles of the wall-normal mean velocities. It is observed that close to the leading edge, i.e.  $x/h = 0.25$ , high values of wall normal velocity are present. This is due to the upward deflection of the flow as it approaches the body. This region is also indicative of upward transport of low momentum fluid into the outer high-speed flow. As  $x/h$  increases, the wall normal velocity decreases and spreads more in the  $y$ -direction. At  $x/h = 1$ ,  $V/U_h$  becomes negative due to entrainment of ambient fluid into the separated shear layer. Close

to the wall, i.e.  $y/h < 1.3$ , there is no significant variation in the wall-normal mean velocity with aspect ratio; variation with aspect ratio is observed only beyond  $y/h > 1.3$ .

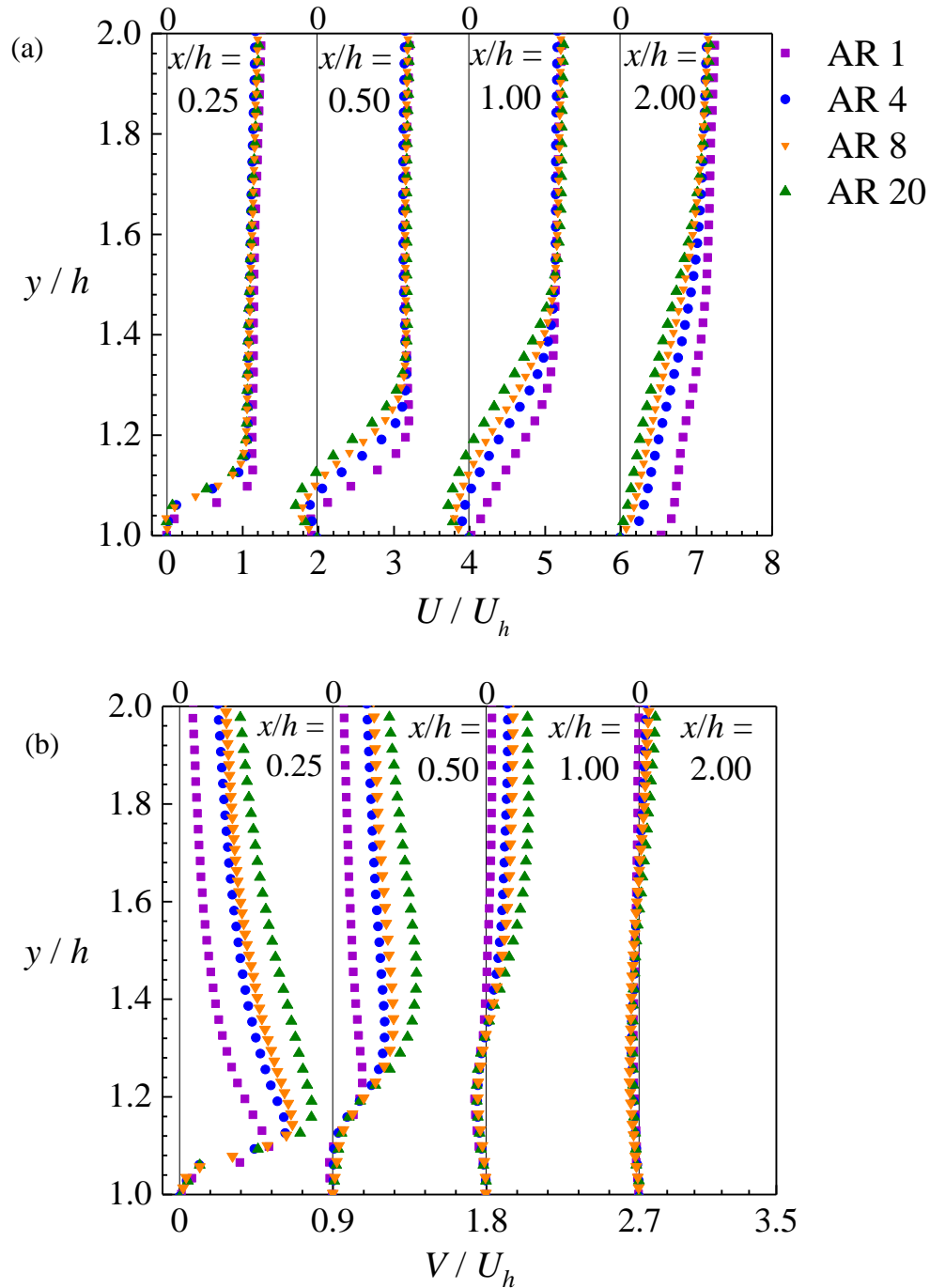
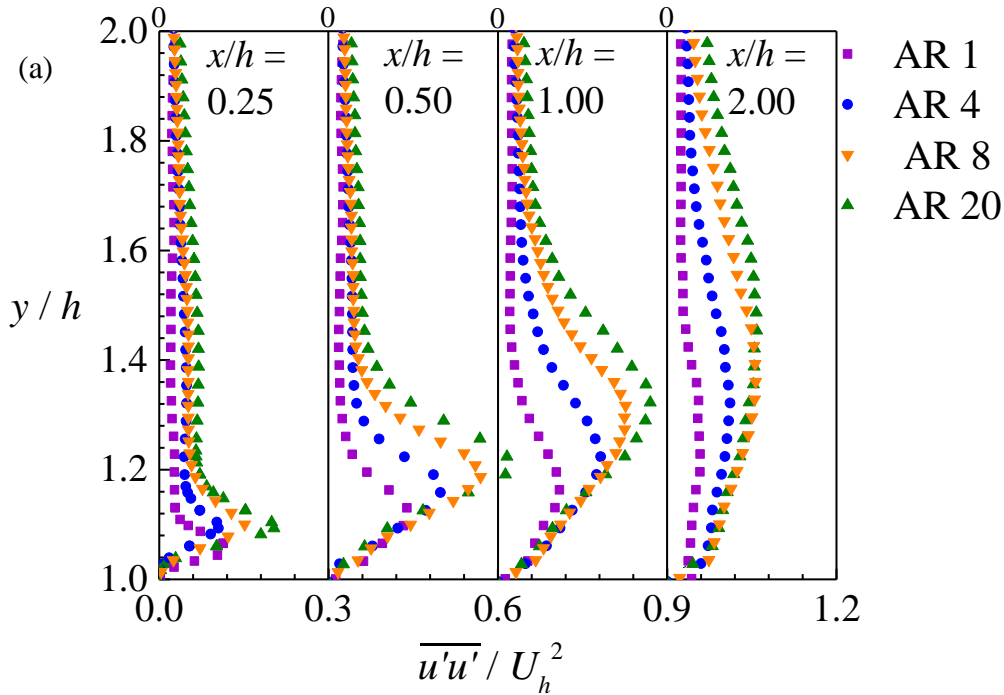


Figure 4-8 One-dimensional profiles of (a) streamwise and (b) wall-normal mean velocities.

The Reynolds stresses are also examined by analysing the streamwise development of one-dimensional profiles of the Reynolds normal and shear stresses, as shown in Fig. 4-9. The Reynolds stresses are normalised by the velocity at the body height,  $U_h^2$  and plotted at  $x/h = 0.25$  to 2 for aspect ratios 1, 4, 8 and 20. In Fig. 4-9(a), the streamwise Reynolds stresses are plotted and it is observed that close to the leading edge (i.e.,  $x/h = 0.25$ ),  $\overline{u'u'}$  peaks close to the wall. This peak value increases with increasing at  $x/h = 0.5$  and then decays as the streamwise distance increases further. The peak values at  $x/h = 0.5$  and 1 are substantially larger than that at the leading edge, approximately 65% and 40% respectively for AR 20. Furthermore, the wall-normal location of the peak value moves farther away from the wall with increasing streamwise distance. This trend has been observed in other separated flows (Nematollahi & Tachie, 2018).



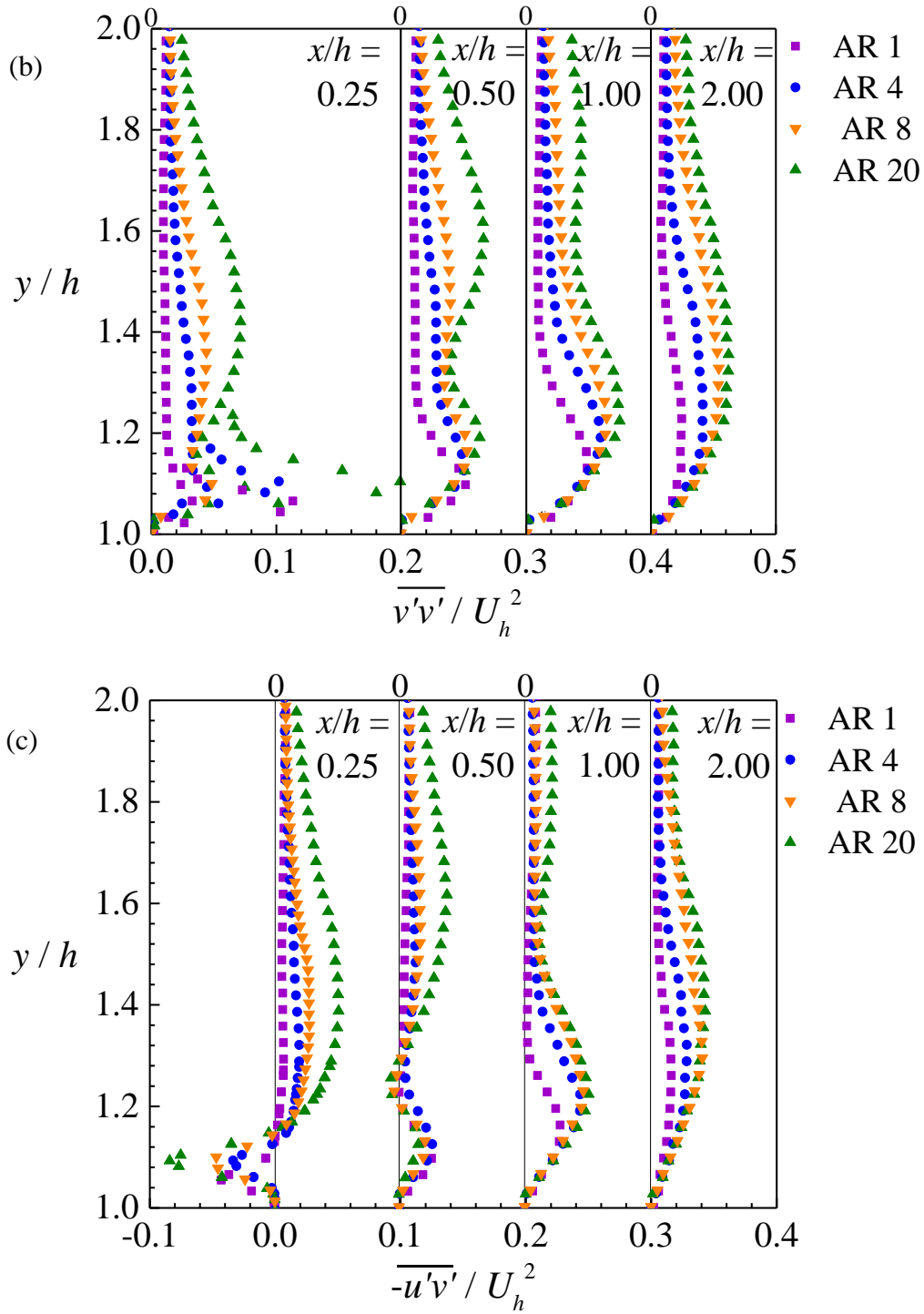


Figure 4-9 One-dimensional profile of Reynolds stresses for aspect ratio 1, 4, 8 and 20.

The higher aspect ratios are also observed to peak farther away from the wall. The one-dimensional profiles for the wall-normal Reynolds normal stress are presented in Fig. 4-9(b). At the leading edge of the bluff body, a high peak of  $\overline{v'v'}$  is observed which is substantially higher than that downstream of the leading edge in all aspect ratio cases. This peak is approximately 230% and 150% higher than at  $x/h = 0.5$  and 1, respectively, for AR 20. The wall-normal Reynolds normal stress is observed to increase as the flow transitions from 3D to 2D, with a peak that is further away from the wall, as observed in  $\overline{u'u'}$ . The trend of the  $\overline{v'v'}$  with increasing streamwise distance is quite similar to  $\overline{u'u'}$ , however, much lower values of  $\overline{v'v'}$  are observed compared to  $\overline{u'u'}$ . This indicates the presence of strong anisotropy in the separated shear layer. A dual peak is also observed in AR 8 and 20 which is not present in the 3D cases. Figure 4-9(c) shows the one-dimensional profiles of the Reynolds shear stress. Besides the strong negative  $-\overline{u'v'}$  values at the leading edge, the profiles of the Reynolds shear stress are qualitatively similar to that of the wall-normal Reynolds normal stress. At the leading edge, the effect of the aspect ratio on  $-\overline{u'v'}$  is localised near the wall. As the streamwise distance increases, the effects of aspect ratio are diminished and diffused farther away from the wall. As discussed earlier, the negative  $-\overline{u'v'}$  was attributed to the countergradient diffusion phenomenon that results in a negative contribution to the turbulence total kinetic energy.

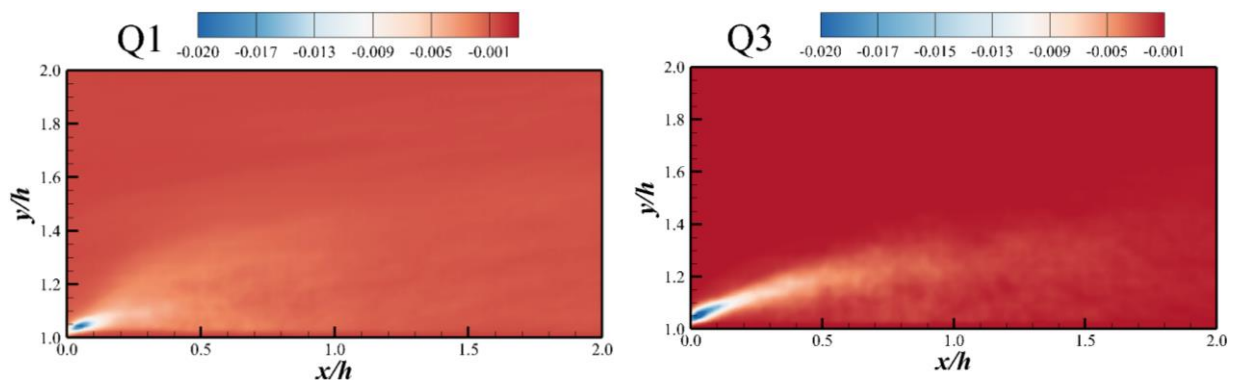
### 4.3 Quadrant Analysis

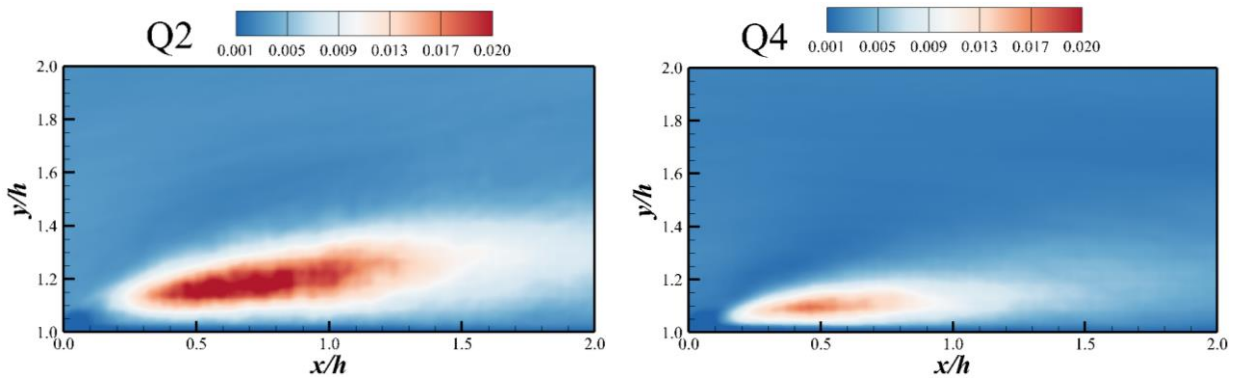
The Reynolds shear stress is further analysed using the quadrant decomposition. As discussed earlier in section 2.2.4, the Reynolds shear stress is divided into four quadrants according to the signs of the streamwise and wall-normal fluctuating velocities. Using the Lu & Willmarth (1973)

hyperbolic hole method, the contribution of each quadrant of the  $u' - v'$  plane to the mean Reynolds shear stress were estimated for  $H_q = 0$ , where the hole size of 0 represents Reynolds shear stress contributions from all events in the decomposition.

Figure 4-10 shows contours of the contributions from the four quadrants: outward motion of high-speed fluid (Q1), ejection of low speed fluid away from the wall (Q2), inward motion of low speed fluid (Q3) and inrush of high-speed fluid (Q4) for AR 1 and 20. In these contour plots, Q1 and Q3 are directly responsible for the negative Reynolds stresses observed in the vicinity of the leading edge. For all aspect ratios, a wider spread of Q3 over Q1 is observed implying the inward interaction term contributes more to the negative Reynolds shear stress near the leading edge of the bluff body. The Q2 and Q4 events are the main contributors to the positive Reynolds shear stress observed downstream of the leading edge. However, the wider spread of the Q2 contours suggests a higher contribution from the ejection of low speed fluid away from the wall to the positive Reynolds shear stress.

AR1





AR 20

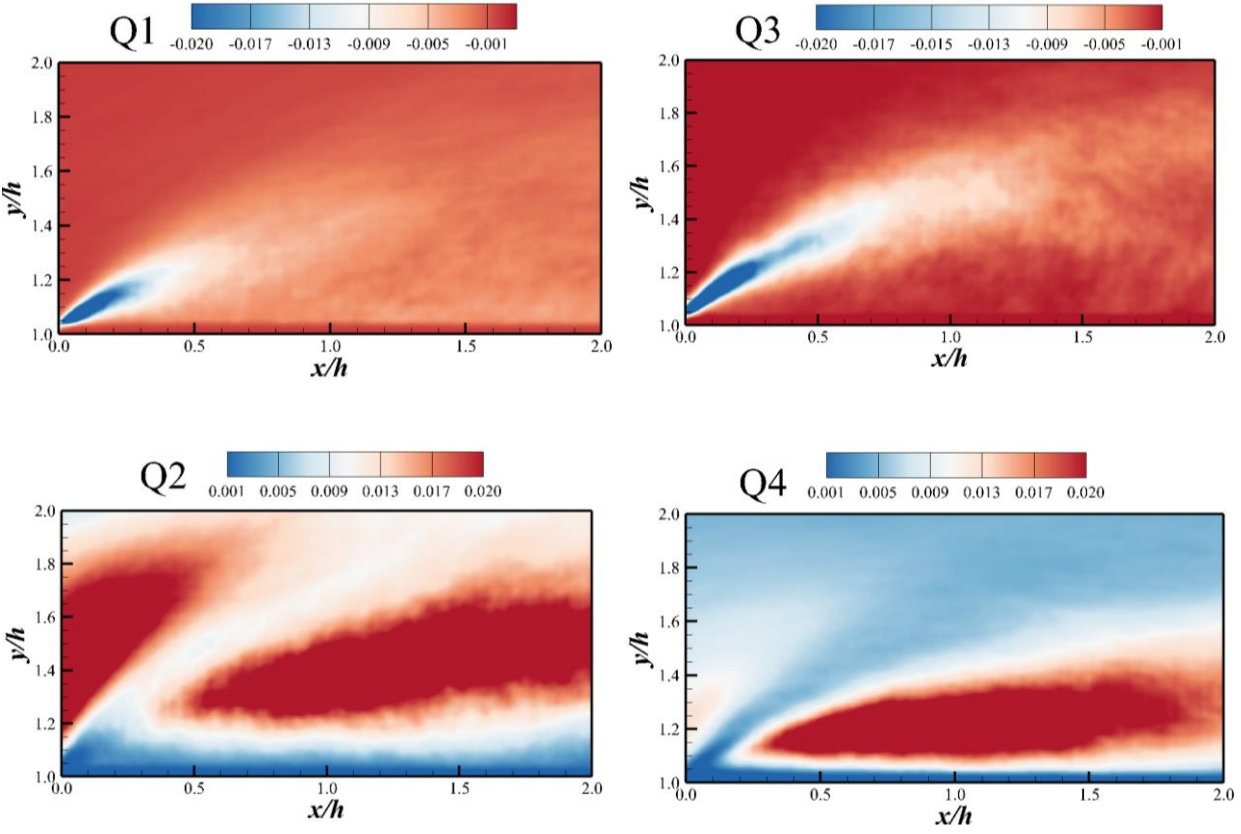


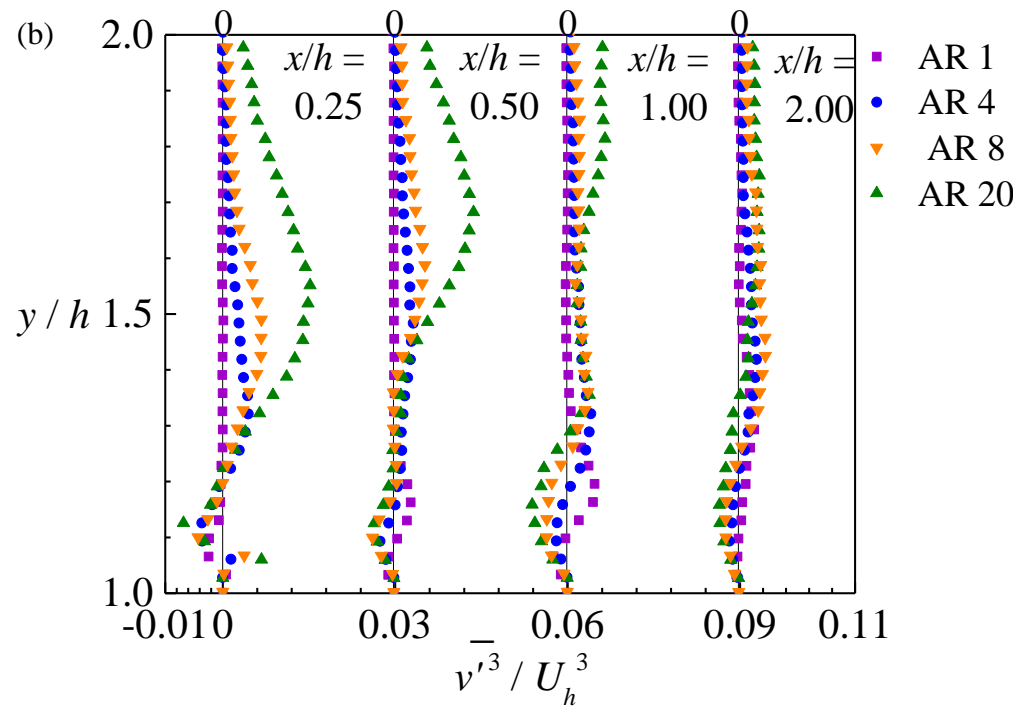
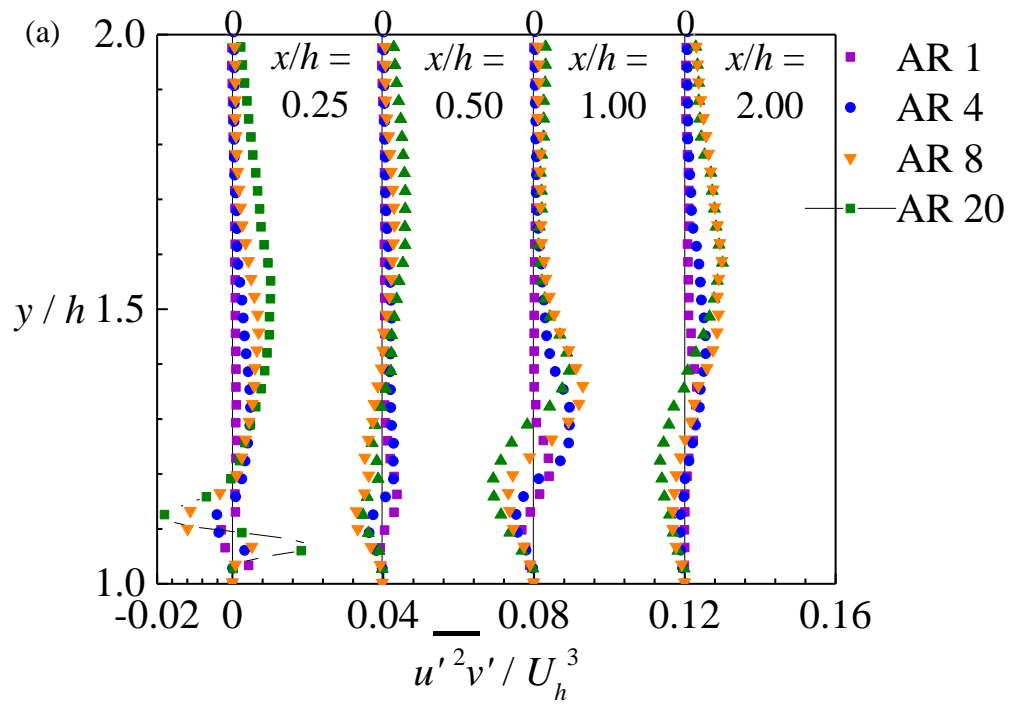
Figure 4-10 Quadrant analysis of AR 1 and 20.

In AR 20, there is the presence of the double peak as observed in the contour plots of  $-\overline{u'v'}$ . The

contours of Q1, Q2, Q3 and Q4 are more widely spread in AR 20 as compared to AR 1.

#### 4.5 Turbulent Transport and Production of Kinetic Energy

Figure 4-11 shows profiles of the triple velocity correlations normalized by  $U_h^3$ . These are plotted at  $x/h = 0.25, 0.5, 1$  and  $2$  locations. The transport of kinetic energy is represented by the gradients of the triple correlation terms. In Fig. 4-11, all plots show the same trend at the leading edge, which is a positive peak near the wall which symbolizes an upward transport of all Reynolds stresses away from the bluff body. This is followed by a negative peak with increasing distance away from the wall, i.e.  $y/h \approx 1.15$ , which shows a deflection towards the wall. The positive and negative peaks are approximately equal in magnitude. Figure 4-11(a) shows the wall-normal turbulent transport of the streamwise Reynolds normal stress ( $\overline{u'^2v'}$ ). In all test cases, two peaks are observed at all locations. Beyond the leading edge, a negative peak is observed close to the wall which is followed by a positive peak farther away from the wall. This signifies that a downward transport of streamwise Reynolds stress occurs in the near-wall region. Farther away from the wall, there is an outward transport of the streamwise Reynolds normal stress towards the external flow away from the high  $\overline{u'u'}$  locations. From  $x/h = 0.5$  to  $1$ , the peaks of wall-normal transport increase after which it diminishes with increasing streamwise distance and moves farther away from the wall, getting closer to a value of zero after reattachment occurs. The wall-normal transport of streamwise Reynolds stress increased with the aspect ratio, for example, at  $x/h = 1$ , the negative peak is observed to increase by approximately 500% from AR 1 to 20. Also, close to the leading edge, the wall-normal transport of streamwise Reynolds stress increases by a magnitude of 400% as the aspect ratio is increased from 1 to 20.



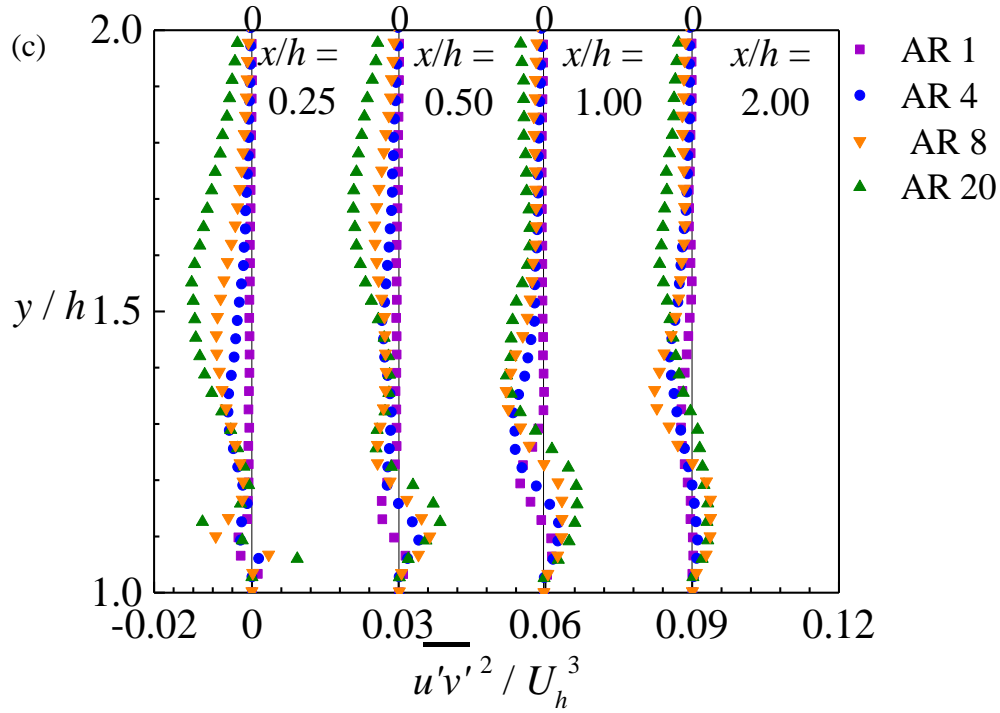


Figure 4-11 One-dimensional profiles of triple correlations.

Figure 4-11(b) presents the one-dimensional profiles of the wall-normal transport of the wall-normal Reynolds normal stress ( $\overline{v'^3}$ ). The plots of  $\overline{v'^3}$  are qualitatively similar to the wall-normal transport of streamwise Reynolds normal stress observed in Fig. 4-11(a). However, the wall-normal transport of  $\overline{u'u'}$  ( $\overline{u'^3}$ ) is far greater than observed for  $\overline{v'v'}$  ( $\overline{v'^3}$ ). The one-dimensional profiles of the wall-normal transport of the Reynolds shear stress is presented in Fig. 4-11(c). Unlike in Fig. 4-11(a) and (b), the wall-normal transport of  $\overline{u'v'}$  is positive close to the wall which represents a continuous diffusion of the Reynolds shear stress away from the wall. Further from the wall, there is a gain in Reynolds shear stress by turbulent diffusion fed by the loss in Reynolds shear stress by turbulent diffusion from the wall region.

The production term of the turbulent kinetic energy transport equation is given by:

$$P_T = -(\overline{u'u'} \partial U / \partial x + \overline{v'v'} \partial V / \partial y + \overline{u'v'} (\partial U / \partial y + \partial V / \partial x)) \quad (4-3)$$

and is decomposed into the contributions from the normal and shear stresses, respectively, as:

$$P_N = -(\overline{u'u'} \partial U / \partial x + \overline{v'v'} \partial V / \partial y) \quad (4-4)$$

$$P_{-uv} = -\overline{u'v'} (\partial U / \partial y + \partial V / \partial x) \quad (4-5)$$

Figure 4-12(a) shows the profiles for the total production term for aspect ratios 1, 4, 8 and 20. These terms are evaluated from equations 4-2, 4-3 and 4-4 respectively. The streamwise distance and production term are normalised by  $l_r$  and  $U_h^3/h$  respectively. It is observed that at the leading edge, there is no significant production, except for the AR 20 case, which is followed by a sudden peak at  $x/l_r = 0.25$ . Further downstream, the level of production decays up to the point of reattachment.

The total production is further analysed by assessing the contributions from the normal and shear stresses to the total production at AR 20 in Fig. 4-12(b). It follows the same trend as observed in Fig. 4-12(a). At  $x/l_r = 0.25$ , there is a sudden positive peak from the normal stresses with a negative contribution from the shear stress which goes to reduce the total production. As the flow evolves further downstream, the level of production reduces with positive contributions from the normal and shear stresses to the total production at reattachment.

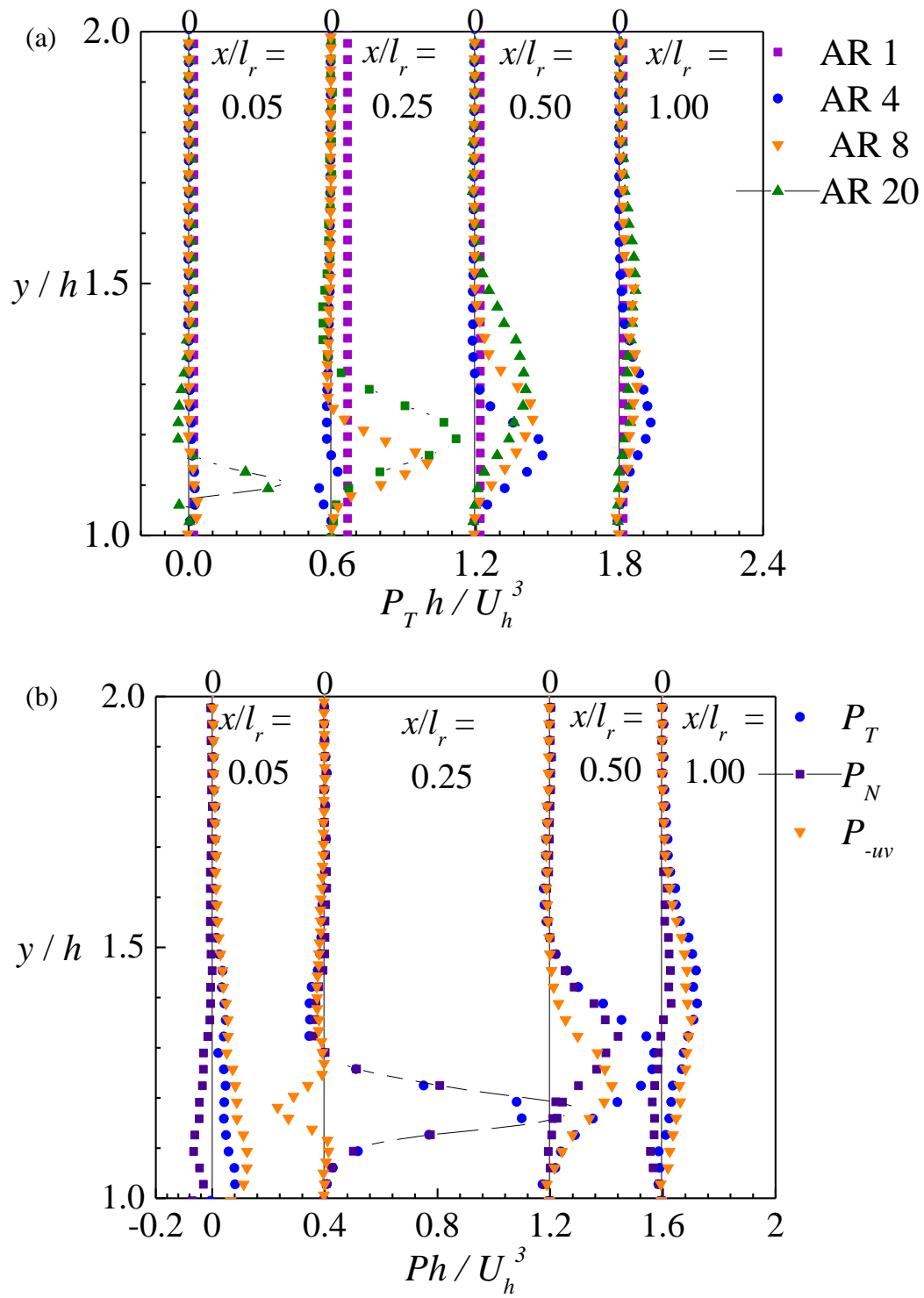


Figure 4-12 One dimensional profile of (a) total production in the AR 1, 4, 8 and 20 cases. (b) contribution of normal and shear stress production to the total production at AR 20 in the recirculation bubble.

## 4.6 Two-Point Correlation

The two-point correlation function is used to examine the effects of aspect ratio on the coherent structures within the separated shear layers. The two-point correlation,  $R_{AB}$ , between the two quantities A and B, at a reference point  $(x_{ref}, y_{ref})$  is defined as

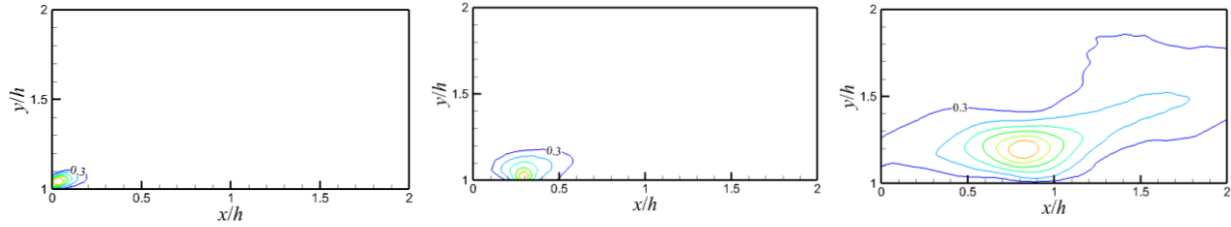
$$R_{AB}(x_{ref} + \Delta x, y_{ref} + \Delta y) = \frac{A(x_{ref}, y_{ref}) B(x_{ref} + \Delta x, y_{ref} + \Delta y)}{\sigma_A(x_{ref}, y_{ref}) \sigma_B(x_{ref} + \Delta x, y_{ref} + \Delta y)} \quad (4-6)$$

where  $\Delta x$  and  $\Delta y$ , respectively, represent the spatial separations in the streamwise and wall-normal directions. Figure 4-13 shows the iso-contours of the two-point spatial auto-correlation function of streamwise velocity ( $R_{uu}$ ) for AR 1, AR 4, AR 8 and AR 20 cases at select reference points. The reference points are selected to coincide with the region of high Reynolds shear stress at the leading edge, the recirculation region and downstream of the recirculation bubble. The contour levels are from 0.3 to 0.9 in 0.1 intervals in all aspect ratios.

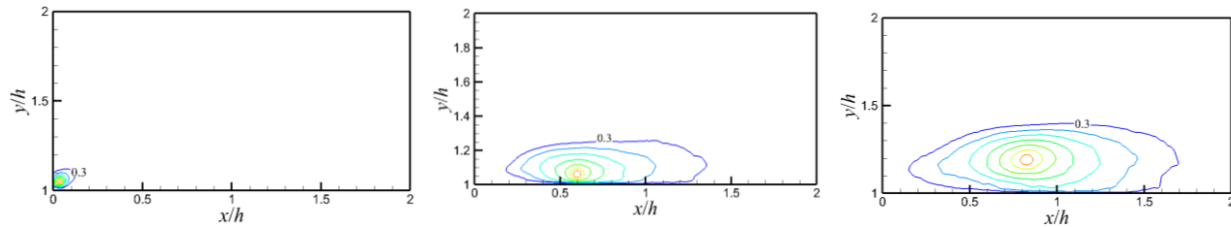
The contour plots in Fig. 4-13(a) and (b) revealed an inclination of the structures, at an angle with respect to the streamwise direction, at the leading edge. Further downstream of the leading edge, the structures are more streamwise-aligned and their sizes grow with increasing streamwise distance from the leading edge. This is observed in all aspect ratios and signifies an increase in spatial correlation of the  $u'$  fluctuations with downstream distance. It is observed that for every selected position, the average size of the turbulent structures increased as the AR increased from 1 to 20 which signifies higher spatial coherence at higher aspect ratios. For AR 20, the  $R_{uu}$  correlation contours in the recirculation region resemble those of separated and reattached turbulent boundary layers. The average streamwise inclination angle of the correlation was

estimated to be  $11^\circ$ . This is in agreement with  $11^\circ$  and  $13^\circ$  reported by Nematollahi (2019) and Volino et al. (2007), respectively.

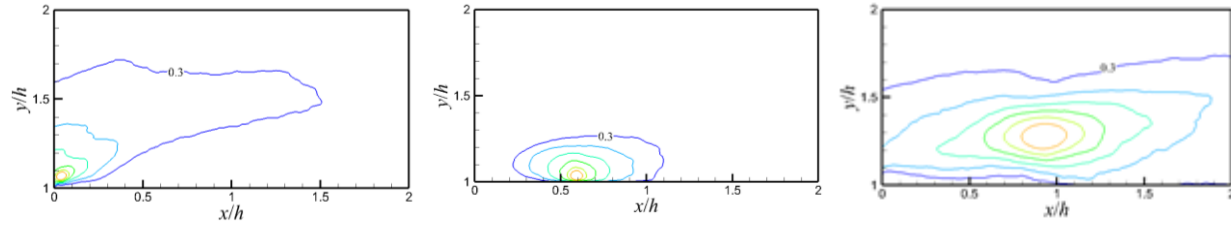
AR 1



AR 4



AR 8



AR 20

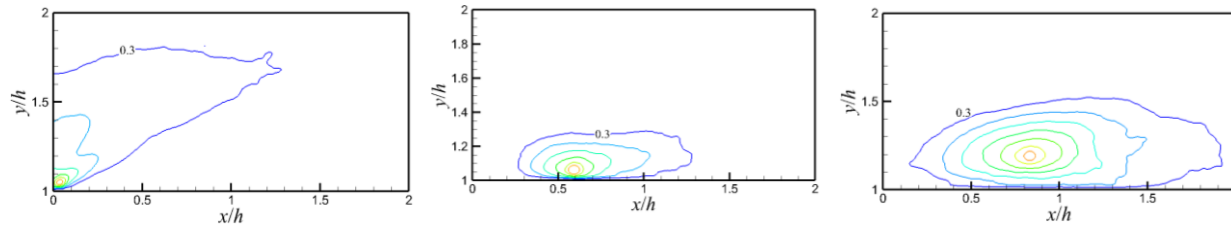
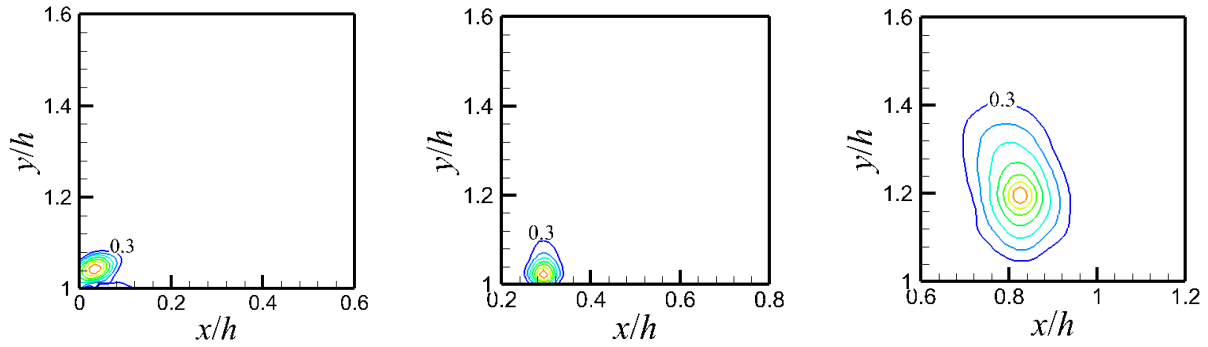


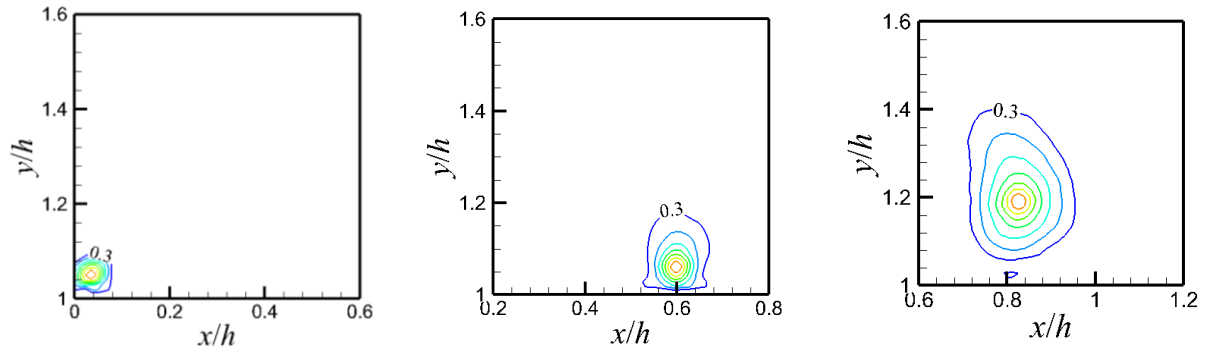
Figure 4-13 Iso-contours of the two-point spatial auto-correlation function of streamwise velocity ( $R_{uu}$ ) in the (a) AR 1, (b) AR 4, (c) AR 8 and (d) AR 20 cases, with the reference point at  $(x/h, y/h) = (0.04, 1)$ ,  $(0.3-0.6, 1)$  and  $(0.8, 1.2)$  (from left to right of each row). Contour levels are from 0.3 to 0.9 in 0.1 intervals.

Figure 4-14 shows the iso-contours of the two-point spatial auto-correlation function of wall-normal velocity ( $R_{vv}$ ) for AR 1, AR 4, AR 8 and AR 20 cases. These contours are smaller, more compact and elongated in the wall-normal direction as compared to the contours of  $R_{uu}$ .

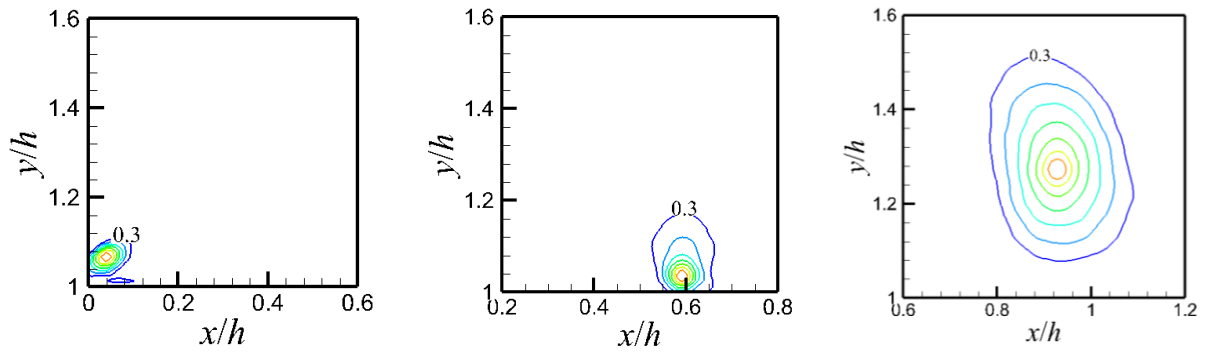
AR 1



AR 4



AR 8



AR 20

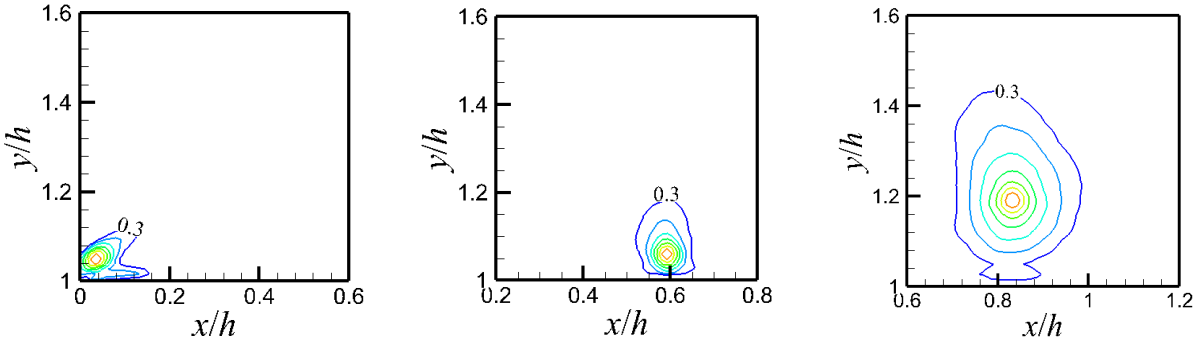


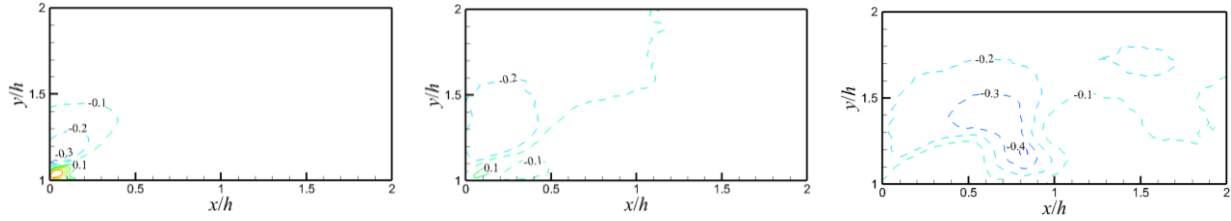
Figure 4-14 Iso-contours of the two-point spatial auto-correlation function of wall-normal velocity ( $R_{vv}$ ) for (a) AR 1, (b) AR 4, (c) AR 8 and (d) AR 20 cases, with the reference point at  $(x/h, y/h) = (0.04, 1)$ ,  $(0.3-0.6, 1)$  and  $(0.8, 1.2)$  (from left to right of each row). Contour levels are from 0.3 to 0.9 with 0.1 intervals.

At the leading edge, the contours are inclined in the  $x - y$  plane as observed in the streamwise case. These observations are consistent with other separated and reattached flows (Nematollahi, 2019). Downstream of the leading edge, the contours are elongated in the wall-normal direction and grow with increasing streamwise distance from the leading edge. The same trend is observed for  $R_{vv}$  as in  $R_{uu}$ ; for every selected position, the average size of the turbulent structures were increased when the AR was increased from 1 to 20 which signifies higher spatial coherence at higher aspect ratios.

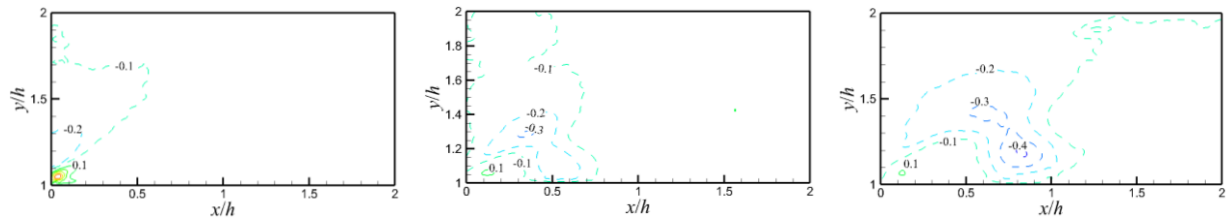
Figure 4-15 represents the iso-contours of the two-point spatial cross-correlation function ( $R_{uv}$ ). The two-point spatial cross-correlation provides information regarding the size and shape of the vortical structures responsible for mixing across the shear layer. It represents the turbulent motions responsible for the of transport low- and high-momentum fluid away from and towards the wall. In Fig. 4-15, there are regions of both positive and negative  $R_{uv}$ . As stated in section 4.3,  $Q1 (u' >$

0,  $v' > 0$ ) and Q3 ( $u' < 0, v' < 0$ ) motions are the main contributors to the positive correlations, and Q2 ( $u' < 0, v' > 0$ ) and Q4 ( $u' > 0, v' < 0$ ) to the negative correlations.

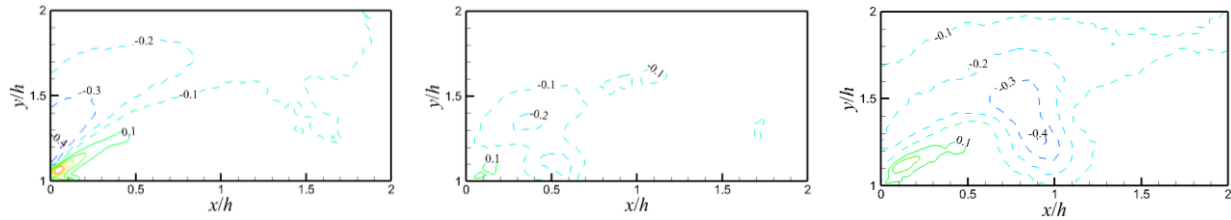
AR 1



AR 4



AR 8



AR 20

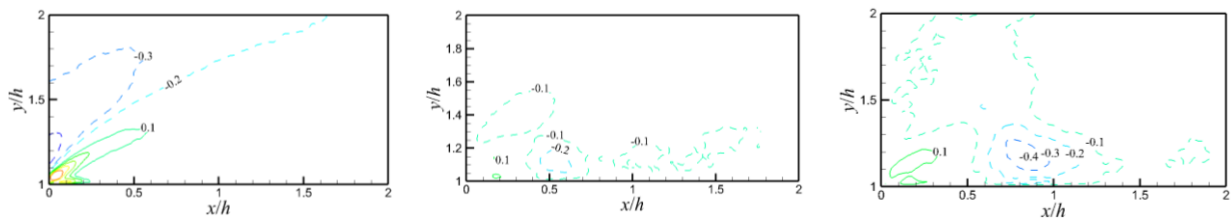


Figure 4-15 Iso-contours of the two-point spatial cross-correlation function ( $R_{uv}$ ) for (a) AR 1, (b) AR 4, (c) AR 8 and (d) AR 20 cases, with the reference point at  $(x/h, y/h) = (0.04, 1)$ ,  $(0.3-0.6, 1)$  and  $(0.8, 1.2)$  (from left to right of each row). Contour levels are from -0.4 to -0.1 and 0.1 to 0.5 with 0.1 intervals.

In all aspect ratios, the negative contours are of considerably larger spatial extent than the positive contours signifying that Q2 and Q4 are the dominant motions producing the Reynolds shear stress. The streamwise evolution of the negative cross-correlation follows the same trend of the  $u$  and  $v$  auto-correlations.

However, the region of positive  $R_{uv}$  is largest at the leading edge and diminishes further downstream. The diminishing size and magnitude of the positive correlations in the smaller aspect ratios is explanatory to the smaller recirculation bubble due to early recovery.

#### 4.7 Joint Probability Density Function (JPDF)

The joint probability density function (JPDF),  $P(u', v')$ , is defined by Wallace & Brodkey (1977) as

$$\langle u'v' \rangle = \iint u'v' P(u', v') du'dv' \quad (4-7)$$

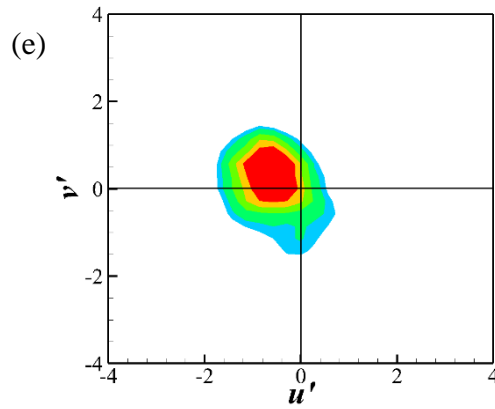
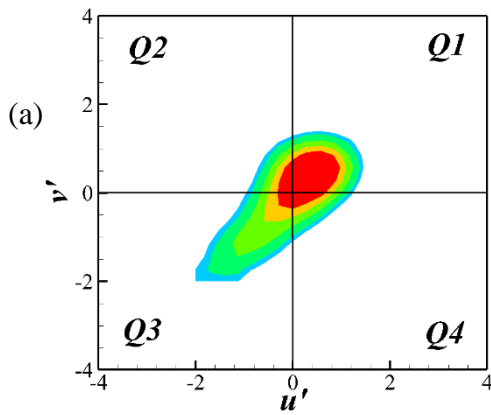
For non-isotropic turbulence, the contours of  $P(u', v')$  are elliptical, where the innermost contours are of high probability, but weak Reynolds shear stress events while the outermost contours are characterised by strong Reynolds shear stress events but are of low probability. Thus, the total Reynolds shear stress will be a balance between the strong but low probability joint events and the weak but high probability joint events. Figure 4-16 shows the distributions of the JPDF at two selected locations: ( $x/h = 0.01, y/h = 1.04$ ) where  $-\overline{u'v'}$  is negative and ( $x/h = 0.8, y/h = 1.2$ ) where  $-\overline{u'v'}$  is positive. At the location where  $-\overline{u'v'}$  is negative, the distributions are inclined towards Q1 and Q3 as expected, indicating the dominance of outward and inward motion of the high and low momentum fluid, respectively. In the case of AR 1, the highest contour level is

predominantly in Q1, however, as the aspect ratio increases so does the contribution from Q3. At  $x/h = 0.8$ ,  $y/h = 1.2$ , the distributions are inclined towards Q2 and Q4, which indicate larger contributions of ejections and sweeps to the mean Reynolds shear stress at this location.

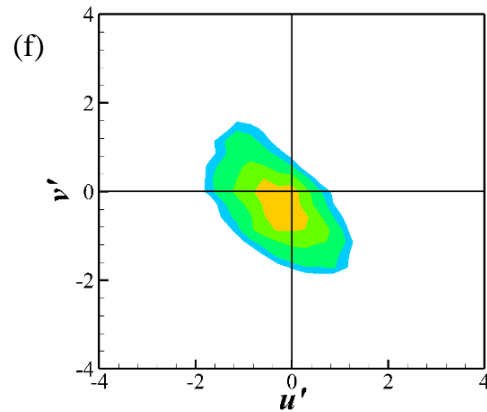
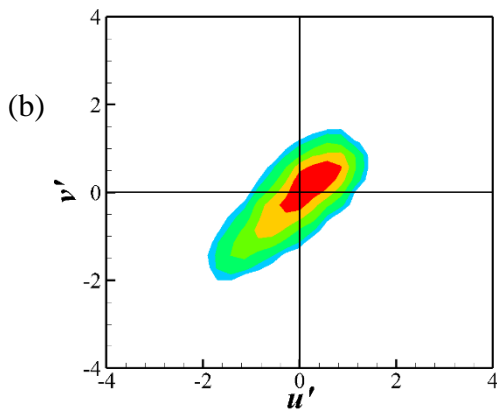
Negative region of  $-\overline{u'v'}$

Positive region of  $-\overline{u'v'}$

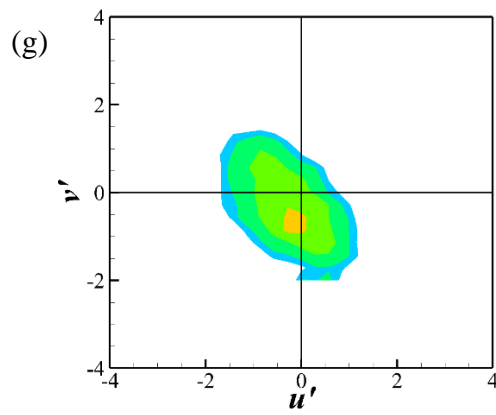
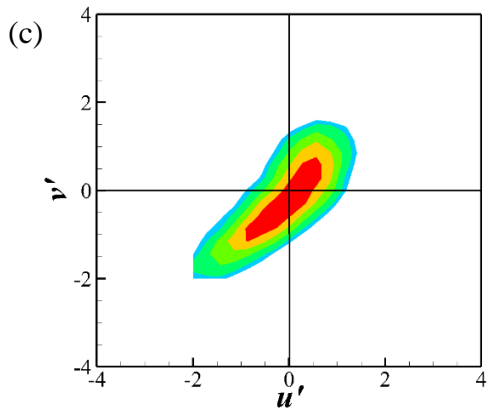
AR 1



AR 4



AR 8



AR 20

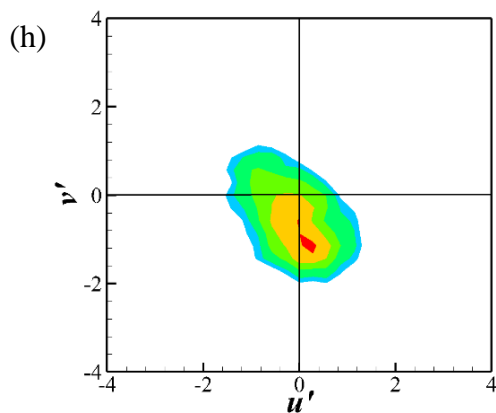
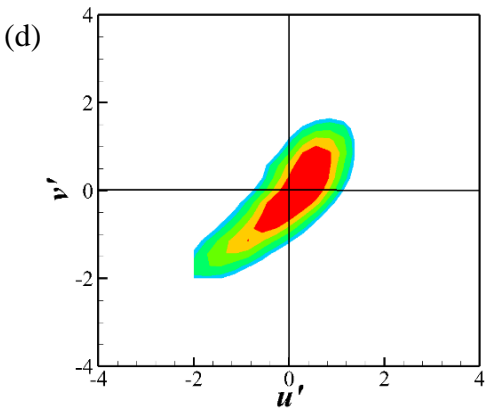


Figure 4-16 Contours of the joint PDF of the velocity fluctuations along the mean dividing streamline: (a)-(d) represents aspect ratios 1, 4, 8 and 20 respectively at  $x/h = 0.04$ ,  $y/h = 1.04$ ; (e)-(f) represents aspect ratios 1, 4, 8 and 20 respectively at  $x/h = 0.8$ ,  $y/h = 1.2$ .

The magnitude of contribution is highest for AR 1 which is in good agreement with the topology observed in the contours of the Reynolds shear stress (see Fig. 4-6).

## 4.8 Proper Orthogonal Decomposition (POD)

The proper orthogonal decomposition method (POD) was applied to the flow fields to reveal the spatial characteristics of the dominant eddies in shear layer. Figure 4-17 shows a comparison of the modal energy and cumulative modal energy distributions among selected aspect ratio cases. To avoid clutter of the data only the first 40 POD modes are plotted. POD is performed for aspect ratios 1, 4, 8 and 20 cases in the region bounded by  $x/h \in [0; 2.36]$  and  $y/h \in [1; 2]$ . The results in Fig. 4-17(a) shows that the first POD mode contributes the largest fraction of the total turbulent kinetic energy (TKE), approximately 26% to 32%, while the contributions from the higher order modes decay very rapidly, reaching 3.3% from the 15th mode. Also, a more rapid convergence is observed for the larger aspect ratio test cases.

A summary of the contribution of the first four modes is shown in Table 4-1. These results are consistent with other studies of separated and reattached flows. Mohammed-Taifour & Weiss (2016) performed a POD analysis for an adverse-pressure-gradient-induced turbulent separation flow. The reported percentages of the first four modes to the total TKE are 31%, 9%, 6% and 4%, respectively. Thacker et al. (2013) conducted a POD analysis for an Ahmed body-induced separation flow. They found that the first four modes contributed 28.0%, 9.5%, 6.0% and 3.5%, respectively, to the total TKE. The first two modes contribute a combined 33.7%, 36.1%, 39.3% and 37.6% for AR 1, 4, 8 and 20 respectively. This shows that the modal contributions are dependent on the aspect ratio; the contributions from the lower modes increase with increasing aspect ratio up to AR 8 and then reduce from  $w/h = 8$  to 20.

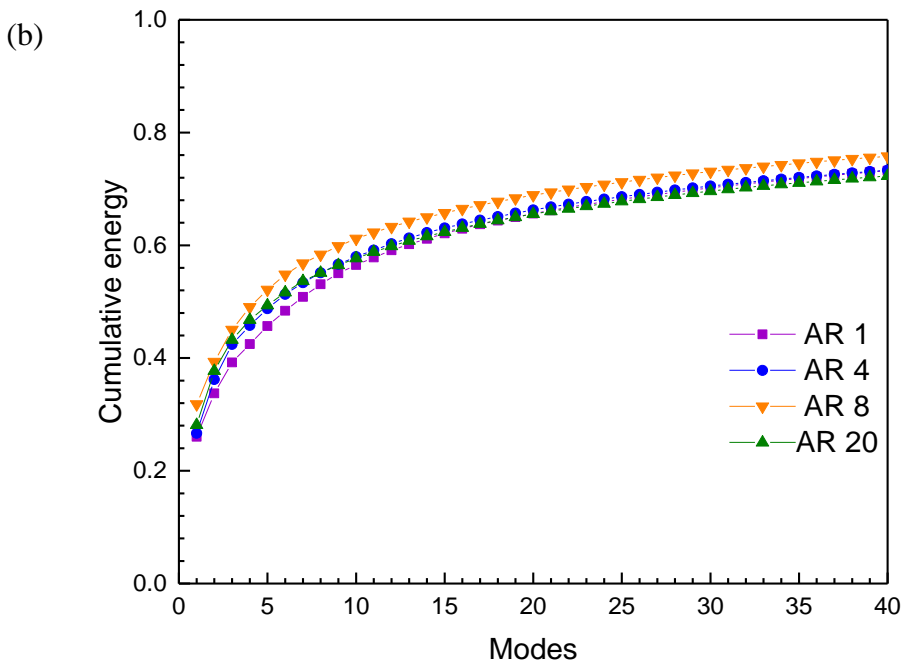
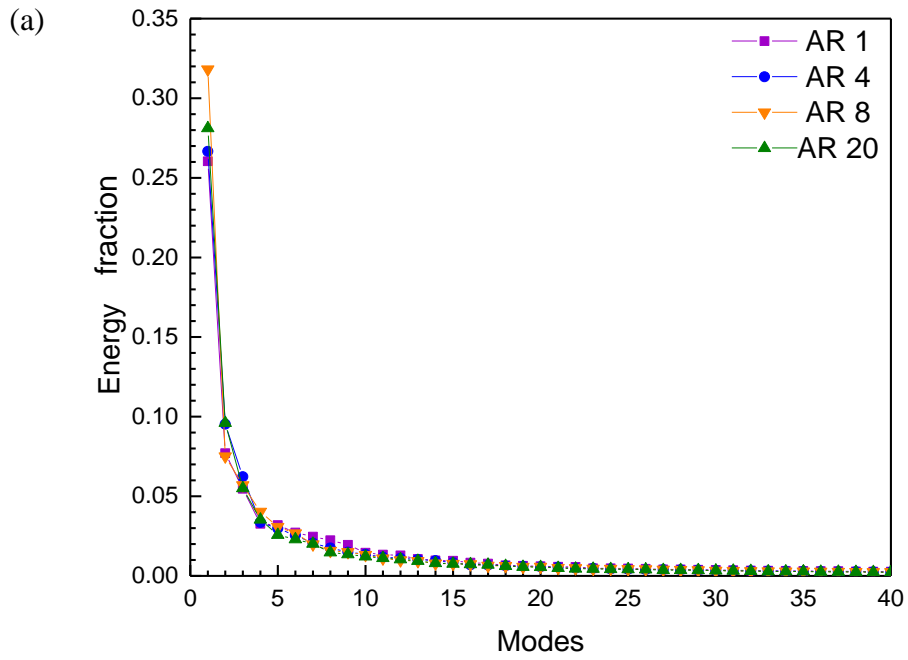


Figure 4-17 Distribution of modal and cumulative energy fractions for the first 40 modes.

Table 4-1 Summary of the contribution of first four modes to the total TKE.

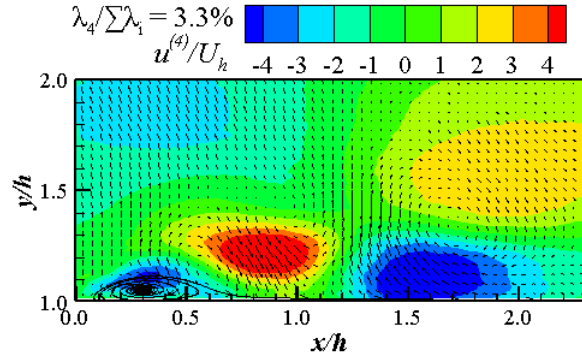
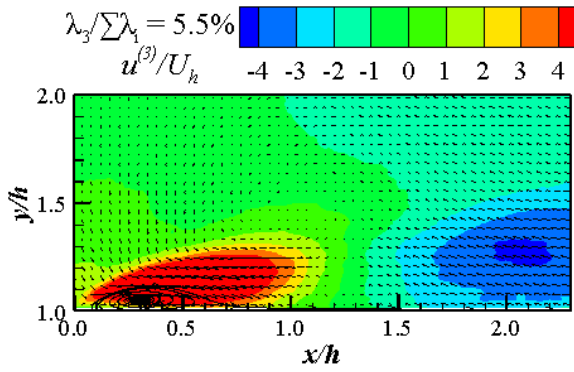
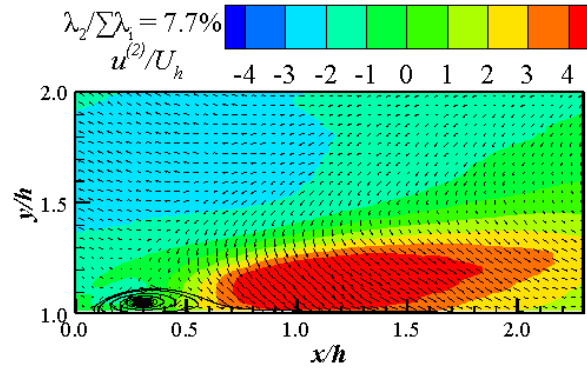
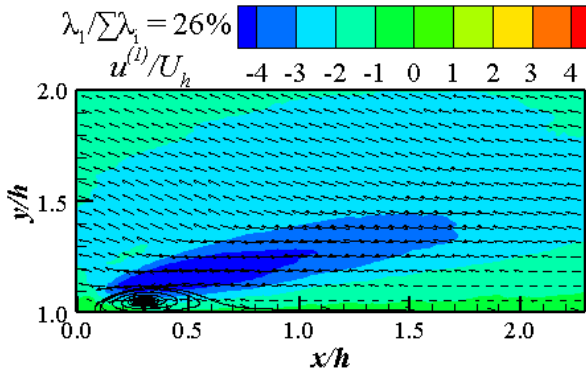
Aspect Ratio	Energy Percentages			
	Mode 1	Mode 2	Mode 3	Mode 4
1	26.0	7.7	5.5	3.3
4	26.6	9.5	6.2	3.3
8	31.8	7.5	5.7	4.0
20	28.0	9.6	5.5	3.3

The combined values of the first two modes in the 2D cases are comparable to 40% and 37.5% reported by Mohammed-Taifour & Weiss (2016) and Thacker et al. (2013) respectively.

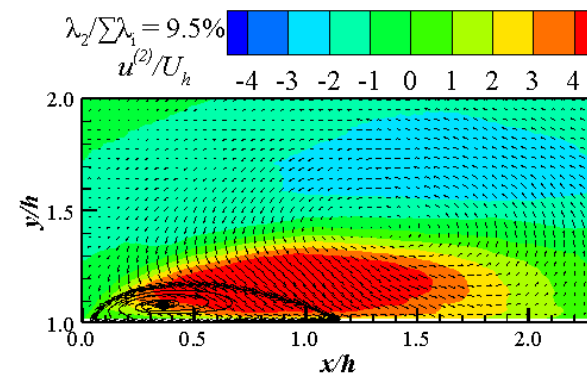
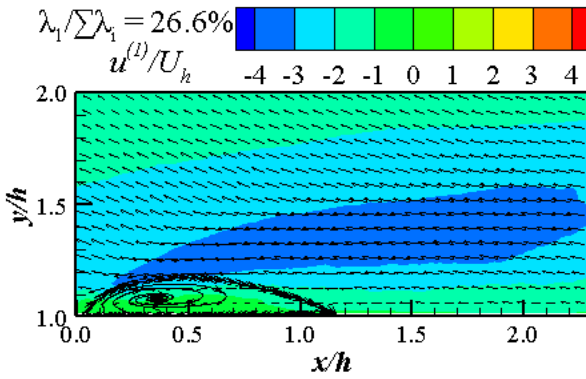
In Fig. 4-17(b), the contribution of the first 40 POD modes to the cumulative energy are shown. It is observed that the first 40 POD modes represent 73%, 73%, 76% and 72% of the total energy content for aspect ratio 1, 4, 8 and 20 respectively. For turbulent separation induced by an Ahmed body, Thacker et al. (2013) reported that the first 30 POD modes contribute 72% of the total energy. This value is comparable to the present study.

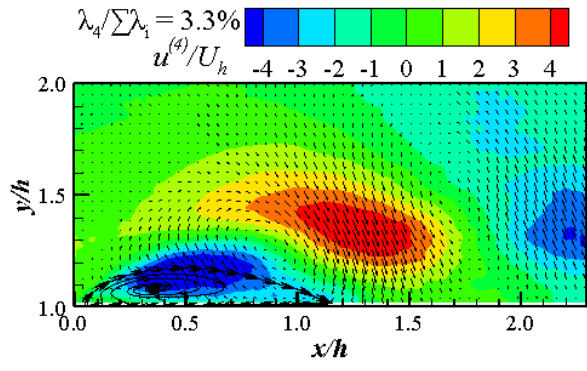
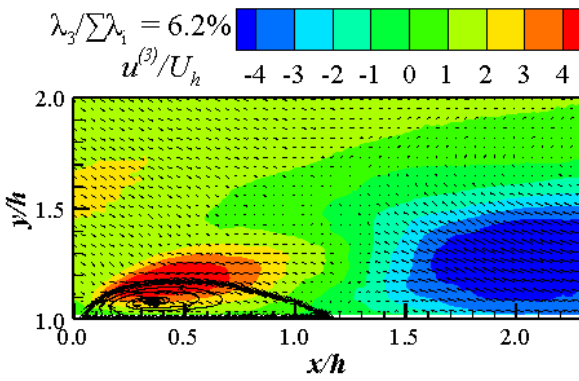
Figure 4-18 illustrates the effects of aspect ratio on the spatial eigen modes in the recirculation region. The plots show the iso-contours of the streamwise component  $\Phi_u(x, y)$  of the first four low-order POD modes. It is observed that the iso-contour of the first spatial mode encompasses the entire recirculation bubble. The first POD mode has been attributed to the global velocity fluctuations inside the recirculated zone that are linked with flapping motion, while the other modes are associated with a large-scale vortex shedding and turbulent motion (Thacker et al., 2013; Mohammed-Taifour & Weiss, 2016).

AR 1

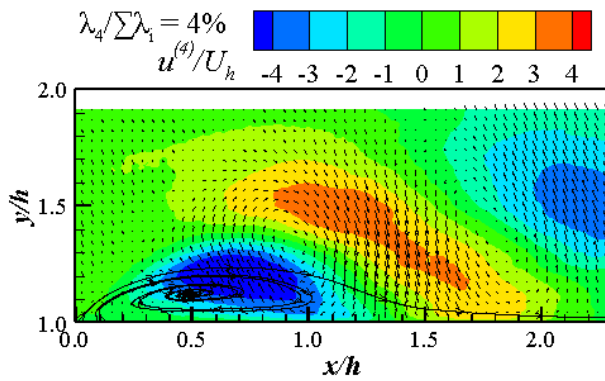
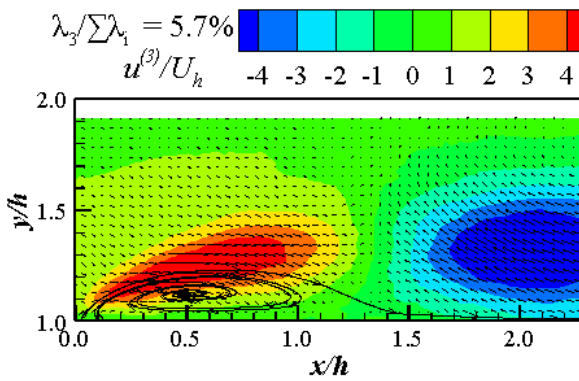
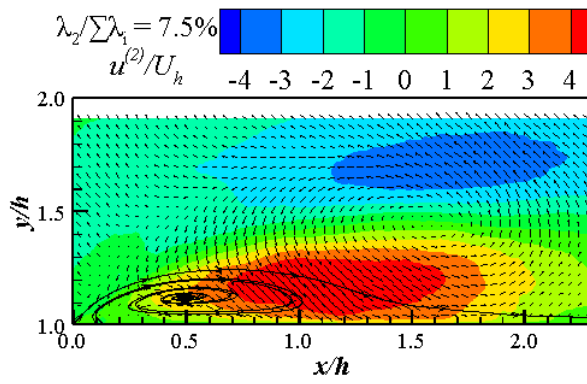
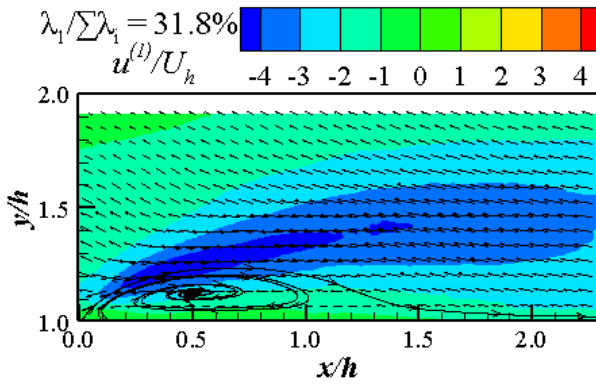


AR 4





AR 8



AR 20

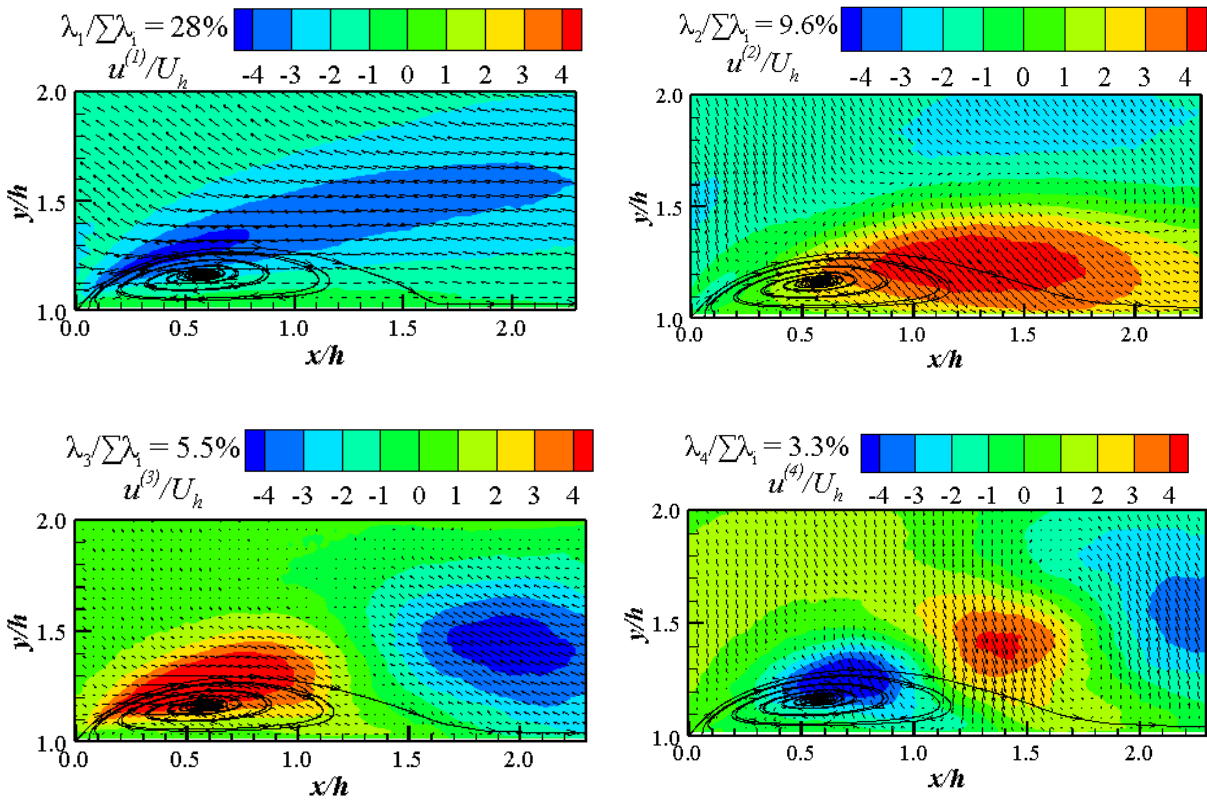


Figure 4-18 Iso-contours of the spatial Eigen modes in the recirculation region for the first four modes in AR 1, 4, 8 and 20.

Thacker et al. (2013) attributed the global flapping of the recirculation zone as the main mechanism that induce most of the turbulent kinetic energy. This suggests that the dynamics of the most dominant spatial mode are related to the physical mechanism responsible for the formation of the recirculation bubble.

In all aspect ratios, the number of visible structures in the iso-contours increases as the number of modes increases, and the structures increase in size with increasing aspect ratio. For the lower aspect ratios, however, the structures are more localised closer to the wall. In Fig. 4-18, large magnitudes of  $u'$  are observed at the leading edge of the bluff body in the first POD mode. This

agrees with the distribution of Reynolds stress  $\overline{u'u'}$  presented in Fig. 4-6 for all aspect ratios. This observation emphasises the dominance of the first POD mode.

## Chapter 5 Conclusions and Recommendation for Future Work

### 5.1 Summary and Conclusion

The effects of the spanwise aspect ratio on the velocity field was investigated using a time-resolved particle image velocimetry system. The thickness of the upstream turbulent boundary layer was 4.8 times the body height. The streamwise aspect ratio of the body was 2.36, which was large enough to allow reattachment of the mean flow over the body, yet small enough to permit interactions between turbulent separation bubble on top of the bluff body and that behind the bluff body. The upcoming turbulent intensity of the bluff body is among the highest in the existing literature. The major conclusions are as follows.

In the mean flow field, two distinct separation bubbles appear: one on top of the bluff body, the other downstream of the bluff body. The reattachment length on top of the bluff body increases monotonically as the aspect ratio increases from  $w/h = 1$  to 8, and  $l_r/h$  approaches an asymptotic value of 1.6. This asymptotic value is comparably higher than previous experiments of separated and reattached flows and this difference may be attributed to differences in upstream conditions. The separation bubble downstream of the bluff body followed the same trend; the reattachment length increases as the aspect ratio increases from  $w/h = 1$  to 8 and becomes asymptotic at  $L_r/h = 5.3$ . This value is in good agreement with that of previous BFS experiment and comparably lower than those recorded by Martinuzzi and Tropea (1993) which were obtained for square ribs ( $l/h = 1$ ) in a fully developed channel flow, and the reattachment lengths measured from the trailing edge. These differences may be attributed to differences in streamwise length to height ratio ( $l/h$ ).

This indicates that for bluff bodies of  $w/h > 8$ , the flow is nominally two-dimensional. This observation is similar to Castro & Dianat (1983) and Martinuzzi and Tropea (1993) who noted that the flow is two-dimensional for aspect ratio,  $w/h > 10$  and  $w/h > 6$  respectively.

The Reynolds stresses, turbulent kinetic energy and turbulent production in the recirculation region were enhanced in the higher aspect ratio cases. The triple velocity correlations gave the indication that transport of turbulent kinetic energy is intense at the leading edge of the step. The triple velocity correlations revealed aspect ratio effects; there was higher transport of turbulent kinetic energy in the higher aspect ratios. At the leading edge of the body, negative eddy kinematic viscosity is present which signifies a counter-gradient diffusion of Reynolds shear stress. Therefore, eddy-viscosity models based on the assumption of positive eddy kinematic viscosity will fail to properly predict the flow of this nature.

The effects of the aspect ratio on the streamwise and wall-normal extents of the two-point auto-correlation functions in the recirculation region were examined. The average size of the turbulent structures was increased as the aspect ratio was increased from 1 to 20 which signifies higher spatial coherence at higher aspect ratios.

The quadrant decomposition of the Reynolds shear stress and joint probability density function analysis both reveal the inward (Q3) and outward (Q1) interaction terms as the dominant contributors to the mean Reynolds shear stress near the leading edge. For all aspect ratios, a wider spread of Q3 over Q1 is observed implying the inward interaction term contributes more to the negative Reynolds shear stress near the leading edge of the bluff body. Downstream of the leading edge, the Q2 and Q4 events are the main contributors to the positive Reynolds shear stress. However, the wider spread of the Q2 contours suggests a higher contribution from the ejection of

low speed fluid away from the wall to the positive Reynolds shear stress. The contours of all quadrants are more widely spread in AR 20 as compared to AR 1.

The dominant structures of the separation bubbles were further studied using proper orthogonal decomposition (POD). The first POD mode contributes the largest fraction of the total turbulent kinetic energy (TKE) while the contributions from the higher order modes decay very rapidly. The number of visible structures in the iso-contours increases as the number of modes increases, and the structures increase in sizes with increasing aspect ratios. An increase in the aspect ratio caused a corresponding increase in the fractional energy convergence of the POD modes.

## 5.2 Recommendation for Future Work

The following recommendations are proposed for future work:

- The time-space correlations could be implemented to study the dynamic coupling of the spatial and temporal characteristics of the coherent structures.
- A three-dimensional measurement system such as the time-resolved tomographic PIV will be useful in obtaining the instantaneous 3D3C velocity field. This will be instrumental in gaining a complete understanding of the complex nature of the separated and reattached flow over bluff bodies.

## References

- Adrian, R. J., Christensen, K. T., & Liu, Z. C. (2000). Analysis and interpretation of instantaneous turbulent velocity fields. *Experiments in Fluids*, 29(3), 275–290. <https://doi.org/10.1007/s003489900087>
- Adrian, R. J. (2007). Hairpin vortex organization in wall turbulence. *Physics of Fluids*. <https://doi.org/10.1063/1.2717527>
- Akon, A. F., & Kopp, G. A. (2016). Mean pressure distributions and reattachment lengths for roof-separation bubbles on low-rise buildings. *Journal of Wind Engineering and Industrial Aerodynamics*, 155, 115–125. <https://doi.org/10.1016/j.jweia.2016.05.008>
- Alfonsi, G. (2008). Passive techniques for control of turbulence in wall-bounded flows. *Journal of Flow Visualization and Image Processing*, 15(3), 217–234. <https://doi.org/10.1615/JFlowVisImageProc.v15.i3.30>
- Ampadu-Mintah, A. A., & Tachie, M. F. (2015). Surface roughness effects on separated and reattached turbulent flow in open channel, 1686. <https://doi.org/10.1080/00221686.2015.1026952>
- Awasthi, M., Devenport, W. J., Glegg, S. A. L., & Forest, J. B. (2014). Pressure fluctuations produced by forward steps immersed in a turbulent boundary layer. *Journal of Fluid Mechanics*, 756, 384–421. <https://doi.org/10.1017/jfm.2014.405>
- Bergeles, G., & Athanassiadis, N. (1983). The flow past a surface-mounted obstacle. *Journal of Fluid Engineering - T. ASME*, 105(December 1983), 461–463.

<https://doi.org/10.1115/1.3241030>

- Berkooz, G., Holmes, P., & Lumley, J. L. (1993). The proper orthogonal decomposition in the analysis of turbulent flows. *Annual Review of Fluid Mechanics*, 25(1), 539–575.  
<https://doi.org/10.1146/annurev.fl.25.010193.002543>
- Brown, G. L., & Roshko, A. (1974). On density effects and large structure in turbulent mixing layers. *Journal of Fluid Mechanics*. <https://doi.org/10.1017/S002211207400190X>
- Casarsa, L., & Giannattasio, P. (2008). Three-dimensional features of the turbulent flow through a planar sudden expansion. *Physics of Fluids*. <https://doi.org/10.1063/1.2832780>
- Castro, I. P. (1979). Relaxing wakes behind surface-mounted obstacles in rough wall boundary layers. *Journal of Fluid Mechanics*, 93(04), 631–659.  
<https://doi.org/doi:10.1017/S0022112079001968>
- Castro, I. P., & Dianat, M. (1983). Surface flow patterns on rectangular bodies in thick boundary layers. *Journal of Wind Engineering and Industrial Aerodynamics*, 11(1–3), 107–119.  
[https://doi.org/10.1016/0167-6105\(83\)90093-4](https://doi.org/10.1016/0167-6105(83)90093-4)
- Castro, I. P., & Robins, A. G. (1977). The flow around a surface-mounted cube in uniform and turbulent streams. *Journal of Fluid Mechanics*, 79(2), 307–335.  
<https://doi.org/10.1017/S0022112077000172>
- Chalmers, H. A., Nyantekyi-Kwakye, B., Fang, X., & Tachie, M. F. (2019). Aspect ratio effects on turbulent flow over forward-backward-facing Steps, 1–8.

- Essel, E. E., Nematollahi, A., Thacher, E. W., & Tachie, M. F. (2015). Effects of upstream roughness and Reynolds number on separated and reattached turbulent flow. *Journal of Turbulence*. <https://doi.org/10.1080/14685248.2015.1033060>
- Essel, E. E., & Tachie, M. F. (2015). Roughness effects on turbulent flow downstream of a backward facing step. *Flow, Turbulence and Combustion*, 94(1), 125–153. <https://doi.org/10.1007/s10494-014-9549-1>
- Essel, E. E., & Tachie, M. F. (2017). Upstream roughness and Reynolds number effects on turbulent flow structure over forward facing step. *International Journal of Heat and Fluid Flow*, 66, 226–242. <https://doi.org/10.1016/j.ijheatfluidflow.2015.11.004>
- Fang, X., & Tachie, M. F. (2019). On the unsteady characteristics of turbulent separations over a forward-backward-facing step. *Journal of Fluid Mechanics*, 863, 994–1030. <https://doi.org/10.1017/jfm.2018.962>
- Fazle Hussain, A.K.M (1986). Coherent structures and turbulence. *Journal of Fluid Mechanics*, 173(January 1987), 303–356. <https://doi.org/10.1017/S0022112086001192>
- Graziani, A., Lippert, M., Uystepuyst, D., & Keirsbulck, L. (2017). Scaling and flow dependencies over forward-facing steps. *International Journal of Heat and Fluid Flow*, 67, 220–229. <https://doi.org/10.1016/j.ijheatfluidflow.2017.08.009>
- Hattori, H., & Nagano, Y. (2010). Investigation of turbulent boundary layer over forward-facing step via direct numerical simulation. *International Journal of Heat and Fluid Flow*. <https://doi.org/10.1016/j.ijheatfluidflow.2010.02.027>

- Hearst, R. J., Gomit, G., & Ganapathisubramani, B. (2016). Effect of turbulence on the wake of a wall-mounted cube. *Journal of Fluid Mechanics*, 804, 513–530. <https://doi.org/10.1017/jfm.2016.565>
- Hillier, R., & Cherry, N. J. (1981). The effects of stream turbulence on separation bubbles. *Journal of Wind Engineering and Industrial Aerodynamics*. [https://doi.org/10.1016/0167-6105\(81\)90007-6](https://doi.org/10.1016/0167-6105(81)90007-6)
- Hussein, H. J., & Martinuzzi, R. (1996). Energy balance for turbulent flow around a surface mounted cube placed in a channel. *Physics of Fluids*, 8(3), 764–780. <https://doi.org/10.1063/1.868860>
- Isomoto, K., & Honami, S. (1989). The effect of inlet turbulence intensity on the reattachment process over a backward-facing step. *Journal of Fluids Engineering, Transactions of the ASME*, 111(1), 87–92. <https://doi.org/10.1115/1.3243604>
- Johnson, R. W., & Smith, B. L. (2016). Fluid dynamics.
- Jovic, S. (1996). An experimental study of a separated/reattached flow behind a backward-facing step, (April).
- Kim, K. C., Ji, H. S., & Seong, S. H. (2003). Flow structure around a 3-D rectangular prism in a turbulent boundary layer. *Journal of Wind Engineering and Industrial Aerodynamics*, 91(5), 653–669. [https://doi.org/10.1016/S0167-6105\(02\)00459-2](https://doi.org/10.1016/S0167-6105(02)00459-2)
- Kiya, M., & Sasaki, K. (1983). Structure of a turbulent separation bubble. *Journal of Fluid Mechanics*. <https://doi.org/10.1017/S002211208300230X>

- Kline, S. J., & Robinson, S. K. (1988). Quasi-coherent structures in the turbulent boundary layer. Part I. Status report on a community-wide summary of the data. In *Proceedings of the International Centre for Heat and Mass Transfer*.
- Largeau, J. F., & Moriniere, V. (2006). Wall pressure fluctuations and topology in separated flows over a forward-facing step. *Experiments in Fluids*, 42(1), 21–40.  
<https://doi.org/10.1007/s00348-006-0215-9>
- Lim, H. C., Castro, I. P., & Hoxey, R. P. (2007). Bluff bodies in deep turbulent boundary layers: Reynolds-number issues. *Journal of Fluid Mechanics*, 571, 97–118.  
<https://doi.org/10.1017/S0022112006003223>
- Lu, S. S., & Willmarth, W. W. (1973). Measurements of the structure of the Reynolds stress in a turbulent boundary layer. *Journal of Fluid Mechanics*.  
<https://doi.org/10.1017/S0022112073000315>
- Lumley, J. L. (1967). Similarity and the turbulent energy spectrum. *Physics of Fluids*.  
<https://doi.org/10.1063/1.1762200>
- Martinuzzi, R., & Tropea, C. (1993). The flow around surface-mounted, prismatic obstacles placed in a fully developed channel flow (Data bank contribution). *Journal of Fluids Engineering*, 115(1), 85. <https://doi.org/10.1115/1.2910118>
- Meyer, K. E., Pedersen, J. M., & Özcan, O. (2007). A turbulent jet in crossflow analysed with proper orthogonal decomposition. *Journal of Fluid Mechanics*, 583, 199–227.  
<https://doi.org/10.1017/S0022112007006143>

- Mohammed-Taifour, A., & Weiss, J. (2016). Unsteadiness in a large turbulent separation bubble. *Journal of Fluid Mechanics*, 799, 383–412. <https://doi.org/10.1017/jfm.2016.377>
- Nakamura, H., Igarashi, T., & Tsutsui, T. (1999). Local heat transfer around a wall-mounted cube. *Transactions of the Japan Society of Mechanical Engineers Series B*, 65, 3105–3110. <https://doi.org/10.1299/kikaib.65.3105>
- Nakamura, Y., & Ozono, S. (1987). The effects of turbulence on a separated and reattaching flow. *Journal of Fluid Mechanics*. <https://doi.org/10.1017/S0022112087001320>
- Nematollahi, A. (2019). Effects of upstream roughness on turbulent flow over a forward-facing step.
- Nematollahi, A., & Tachie, M. F. (2018). Time-resolved PIV measurement of influence of upstream roughness on separated and reattached turbulent flows over a forward-facing step. *AIP Advances*, 8(10), 105110. <https://doi.org/10.1063/1.5063455>
- Piirto, M., Saarenrinne, P., Eloranta, H., & Karvinen, R. (2003). Measuring turbulence energy with PIV in a backward-facing step flow. *Experiments in Fluids*, 35(3), 219–236. <https://doi.org/10.1007/s00348-003-0607-z>
- Robinson, S. K. (1991). Coherent motions in the turbulent boundary layer.
- Samimy, M., & Lele, S. K. (1991). Motion of particles with inertia in a compressible free shear layer. *Physics of Fluids A*, 3(8), 1915–1923. <https://doi.org/10.1063/1.857921>
- Samson, A., & Sarkar, S. (2015). Effects of free-stream turbulence on transition of a separated

- boundary layer over the leading-edge of a constant thickness airfoil. *Journal of Fluids Engineering*, 138(2), 021202. <https://doi.org/10.1115/1.4031249>
- Sherry, M. J., Lo Jacono, D., Sheridan, J., Mathis, R., & Marusic, I. (2009). Flow separation characterisation of a forward facing step immersed in a turbulent boundary layer. In *6th International Symposium on Turbulence and Shear Flow Phenomena, TSFP 2009*.
- Sherry, M. J., Lo Jacono, D., & Sheridan, J. (2010). An experimental investigation of the recirculation zone formed downstream of a forward facing step. *Journal of Wind Engineering and Industrial Aerodynamics*, 98(12), 888–894. <https://doi.org/10.1016/j.jweia.2010.09.003>
- Sirovich, L. (1987). Turbulence and the dynamics of coherent structures part I: coherent structures. *Quarterly of Applied Mathematics*, 45(3), 561–571. <https://doi.org/10.1090/qam/910463>
- Sousa, J. M. M. (2001). Turbulent flow around a surface-mounted obstacle using 2D-3C DPIV. *DLR-Mitteilung*, 33(3), 1303–1311. <https://doi.org/10.1007/s00348-002-0497-5>
- Stern, F., Muste, M., Berninatti, M.-L., & Eichinger, W. E. (1999). Summary of experimental uncertainty assessment methodology with example.pdf.
- Thacker, A., Aubrun, S., Leroy, A., & Devinant, P. (2013). Experimental characterization of flow unsteadiness in the centerline plane of an Ahmed body rear slant. *Experiments in Fluids*, 54(3). <https://doi.org/10.1007/s00348-013-1479-5>
- van der Kindere, J., & Ganapathisubramani, B. (2018). Effect of length of two-dimensional obstacles on characteristics of separation and reattachment. *Journal of Wind Engineering and Industrial Aerodynamics*, 178(January), 38–48. <https://doi.org/10.1016/j.jweia.2018.04.018>

- Volino, R. J., Schultz, M. P., & Flack, K. A. (2007). Turbulence structure in rough- and smooth-wall boundary layers. *Journal of Fluid Mechanics*, 592, 263–293.  
<https://doi.org/10.1017/S0022112007008518>
- Wallace, J. M., & Brodkey, R. S. (1977). Reynolds stress and joint probability density distributions in the u-v plane of a turbulent channel flow. *Physics of Fluids*.  
<https://doi.org/10.1063/1.861897>
- Wallace, J. M., Eckelmann, H., & Brodkey, R. S. (1972). The wall region in turbulent shear flow. *Journal of Fluid Mechanics*. <https://doi.org/10.1017/S0022112072000515>
- Willmarth, W. W., & Lu, S. S. (1972). Structure of the reynolds stress near the wall. *Journal of Fluid Mechanics*. <https://doi.org/10.1017/S002211207200165X>

## **Appendix**

### **A.1 Measurement Uncertainty**

Measurement error or uncertainty is defined as the difference between a measured value and the true value of a physical variable. The total error is a combination of the precision (random) error and the bias (systematic) error. A precision error arises from the scatter of the data and is random. A bias error is a systematic error, where it is introduced by the measurement system and procedure. A detailed uncertainty methodology was presented in Coleman & Steele (1995), following the AIAA standard. Common sources of error in PIV measurements come from sub-particle displacement bias, insufficient sample size, spatial resolution, seeding particles, particle response time to fluid motion and positioning of the laser sheet.

To minimize the error in the current study, a large sample size was used, which reduced the precision error. The settling velocity and response time of the selected seeding particles confirmed that these particles will faithfully follow the flow and the maximum particle displacement was set to  $\frac{1}{4}$  of the interrogation area used. The interrogation area was chosen to be as small as possible to improve the spatial resolution, but large enough to contain sufficient number of particles.

### **A.2 Error Estimation**

In this section, the analysis of the bias and precision errors for the PIV measurement in this study are presented.

### A.2.1 The Estimation of Bias Errors

The instantaneous velocity at any given point for PIV measurements is given by:

$$U_i = \Delta s_i L_o / \Delta t L_i \quad (\text{A-1})$$

where  $U_i$  is the velocity component,  $\Delta s_i$  is the component of the particle displacement in the  $x - y$  direction obtained from the correlation algorithm,  $L_o$  is the width of the field of view of the camera,  $\Delta t$  is the time between pulses and  $L_i$  is the width of the digital image.

The bias limit of the measured velocity is determined with a root-sum-square (RSS) of the elementary bias limits based on the sensitivity coefficients, which are given as:

$$B_{U_i}^2 = \theta_{\Delta s_i}^2 B_{\Delta s_i}^2 + \theta_{L_o}^2 B_{L_o}^2 + \theta_{\Delta t_i}^2 B_{\Delta t_i}^2 + \theta_{L_i}^2 B_{L_i}^2 \quad (\text{A-2})$$

where the sensitivity coefficients,  $\theta x$ , are defined as:

$$\theta x = \partial U_i / \partial X \quad (\text{A-3})$$

$$\text{where } X = (\Delta s_i, L_o, \Delta t, L_i). \quad (\text{A-4})$$

The bias errors were estimated for  $U$  and  $V$  for the various test conditions and a typical case presented for AR 1, performed at  $(x, y, z) = (0.2, 1.1, 0.0)$  and  $(x, y, z) = (3.1, 0.93, 0.0)$  coinciding with the leading and trailing edge regions, respectively. These regions were specifically chosen due to the presence of wide range of velocities and turbulence intensity distributions. A summary of the results are presented in Tables A-1, A-2, A-3 and A-4. The bias limits of  $\Delta s$  and  $\Delta t$  were obtained from the PIV system manufacturer's specifications. The bias limit for  $L_o$  is obtained from a calibration procedure.

Table A-1 Bias error of the local streamwise mean velocity ( $U$ ) at  $(x, y, z) = (0.2, 1.1, 0.0)$  in the AR 1 case

Variable	Magnitude	$Bx$	$\theta x$	$Bx\theta x$	$(Bx\theta x)^2$
$L_o$ (m)	7.80E-02	5.00E-04	2.32E+00	1.16E-03	1.34E-06
$L_l$ (pix)	1.92E+03	5.00E-01	9.42E-05	4.71E-05	2.22E-09
$\Delta t$ (s)	1.00E-03	1.00E-07	1.81E+02	1.81E-05	3.27E-10
$\Delta s$ (pix)	4.45E+00	1.27E-02	4.06E-02	5.16E-04	2.66E-07
$U$ (m/s)	1.81E-01				
				$\sum(Bx\theta x)^2$	1.61E-06
				Bias error	1.27E-03
				%Bias Error	0.7%

Table A-2 Bias error of the local wall-normal mean velocity ( $V$ ) at  $(x, y, z) = (0.2, 1.1, 0.0)$  in the AR 1 case

Variable	Magnitude	$Bx$	$\theta x$	$Bx\theta x$	$(Bx\theta x)^2$
$L_o$ (m)	6.50E-02	5.00E-04	8.00E-01	4.00E-04	1.60E-07
$L_l$ (pix)	1.60E+03	5.00E-01	3.25E-05	1.62E-05	2.64E-10
$\Delta t$ (s)	1.00E-03	1.00E-07	5.20E+01	5.20E-06	2.70E-11
$\Delta s$ (pix)	1.28E+00	1.27E-02	4.06E-02	5.16E-04	2.66E-07
$V$ (m/s)	5.20E-02				
				$\sum(Bx\theta x)^2$	4.26E-07
				Bias error	6.53E-04
				%Bias Error	1.26%

Table A-3 Bias error of the local streamwise mean velocity ( $U$ ) at  $(x, y, z) = (3.1, 0.93, 0.0)$  in the AR 1 case

Variable	Magnitude	$Bx$	$\theta x$	$Bx\theta x$	$(Bx\theta x)^2$
$L_o$ (m)	1.97E-01	5.00E-04	8.68E-01	4.34E-04	1.88E-07
$L_l$ (pix)	1.92E+03	5.00E-01	8.91E-05	4.45E-05	1.98E-09
$\Delta t$ (s)	1.00E-03	1.00E-07	1.71E+02	1.71E-05	2.93E-10
$\Delta s$ (pix)	1.67E+00	1.27E-02	1.03E-01	1.30E-03	1.70E-06
$U$ (m/s)	1.71E-01				
				$\sum(Bx\theta x)^2$	1.89E-06
				Bias error	1.37E-03
				%Bias Error	0.8%

Table A-4 Bias error of the local wall-normal mean velocity ( $V$ ) at  $(x, y, z) = (3.1, 0.93, 0.0)$  in the AR 1 case

Variable	Magnitude	$Bx$	$\theta x$	$Bx\theta x$	$(Bx\theta x)^2$
$L_o$ (m)	1.64E-01	5.00E-04	2.53E-01	1.26E-04	1.60E-08
$L_I$ (pix)	1.60E+03	5.00E-01	2.59E-05	1.30E-05	1.68E-10
$\Delta t$ (s)	1.00E-03	1.00E-07	4.15E+01	4.15E-06	1.72E-11
$\Delta s$ (pix)	4.05E-01	1.27E-02	1.03E-01	1.30E-03	1.69E-06
$V$ (m/s)	4.15E-02				
				$\sum(Bx\theta x)^2$	1.71E-06
				Bias error	1.31E-03
				%Bias Error	3.15%

### A.2.2 The Estimation of Precision Errors

The precision error is estimated as

$$P = T \sigma / \sqrt{N} \quad (\text{A-5})$$

where  $T$  is the confidence coefficient and takes the value of 2 for a 95% confidence level as suggested by Stern et al. (1999),  $N$  is the sample size and  $\sigma$  is the standard deviation. To calculate the precision error, the samples (32000 image pairs) were sub-divided into 10 sets and mean velocities were calculated using each set. The values of precision errors for the streamwise and vertical velocities at the location  $(x, y, z) = (0.2, 1.1, 0.0)$  are 0.066% and 0.001%, respectively. The values of precision errors for the streamwise and vertical velocities at the location  $(x, y, z) = (3.1, 0.93, 0.0)$  are 0.098% and 0.012%, respectively. Compared to the bias errors shown in Tables A-1, A-2, A-3 and A-4, the precision errors are apparently negligible.

### A.2.3 The Estimation of Total Errors

The total uncertainty (E) is defined as the RSS of the bias and precision errors as

$$E = \sqrt{B_x + P_x} \quad (\text{A-6})$$

As such, the total uncertainties of the streamwise and vertical mean velocities at the location  $(x, y, z) = (0.2, 1.1, 0.0)$  are 0.88% and 1.12%, respectively. The total uncertainties of the streamwise and vertical mean velocities at the location  $(x, y, z) = (3.1, 0.93, 0.0)$  are 0.95% and 1.78%, respectively.

Following Casarsa & Giannattasio (2008), the sampling errors of second-order statistics can be computed as

$$\varepsilon_{u_{rms}} = \frac{S[u_{rms}]}{u_{rms}} = \frac{T}{\sqrt{2N}},$$

$$\varepsilon_{uv'} = \frac{S[uv']}{uv'} = \frac{T}{\sqrt{N}},$$

where  $\varepsilon$  and  $s[\cdot]$  denote relative sampling error and the estimated standard deviation, respectively.

By substituting  $N = 32000$  into the above equations, the values of  $\varepsilon_{u_{rms}}$  and  $\varepsilon_{uv'}$  were calculated to be 0.79% and 1.12%, respectively.

## A.3 Copyright Permission



RightsLink®

[My Orders](#)

[My Library](#)

[My Profile](#)

Welcome haamorin3@gmail.com [Log out](#) | [Help](#)

[My Orders](#) > [Orders](#) > [All Orders](#)

### License Details

This Agreement between University of Manitoba -- Helen Amarin ("You") and AIP Publishing ("AIP Publishing") consists of your license details and the terms and conditions provided by AIP Publishing and Copyright Clearance Center.

[Print](#)

[Copy](#)

License Number	4816931323617
License date	Apr 27, 2020
Licensed Content Publisher	AIP Publishing
Licensed Content Publication	Physics of Fluids
Licensed Content Title	Energy balance for turbulent flow around a surface mounted cube placed in a channel
Licensed Content Author	H. J. Hussein, R. J. Martinuzzi
Licensed Content Date	Mar 1, 1996
Licensed Content Volume	8
Licensed Content Issue	3
Type of Use	Thesis/Dissertation
Requestor type	Student
Format	Print and electronic
Portion	Figure/Table
Number of figures/tables	1
Title	An Experimental Study of Surface-Mounted Bluff Bodies Immersed in Thick Turbulent Boundary Layers
Institution name	University of Manitoba
Expected presentation date	Apr 2020
Portions	Figure 5
Requestor Location	Helen Amarin 601-2815 Pembina Highway